ZINC-BASED PHOTORESIST FOR HIGH-RESOLUTION EUV (EXTREME ULTRAVIOLET) LITHOGRAPHY

A Thesis

Presented to the Faculty of the Graduate School

of Cornell University

In Partial Fulfillment of the Requirements for the Degree of

Master of Science

by

Kou Yang

August 2019

ABSTRACT

The electronics industry is pursuing smaller feature sizes based on Moore's law, thus a smaller wavelength light source is needed in order to achieve higher resolution. In recent years, next-generation lithography (NGL) technologies such as Extreme Ultraviolet (EUV) lithography have attracted scientists' attention. With a wavelength of 13.5 nm, smaller features can be printed in a single step. Among the emerging EUV photoresists, HfO_2 and ZrO_2 based photoresists developed by researchers at Cornell University show promising results. However, Zr and Hf are relatively low EUV absorbing metals compared to Zn. Under this notion, a series of photoresists using high EUV absorption element Zn as the metal core were developed. In this work, a set of zinc-based nanoparticles with different acid ligands were synthesized, and their photolithographic performance was explored. This work hopes to guide and promote the design for next-generation EUV photoresists.

BIOGRAPHICAL SKETCH

Kou Yang earned her B.S in Polymer Science and Engineering from 2013 to 2017 at the South University of Technology, China. As an undergraduate, Kou worked primarily with the development of Aggregation-induced Emission (AIE) materials applied in OLED devices. Then starting from August 2017 until the present, Kou became an M.S. student majoring in Materials Science and Engineering at Cornell University. During her graduate study, she joined Prof. Christopher K. Ober's research group and worked on lithography. Her research focuses on zinc-based nanoparticles used for EUV photoresists.

ACKNOWLEDGEMENTS

First of all, I would like to express my sincere gratitude to my graduate research advisor Prof. Christopher Ober of the department of Materials Science and Engineering at Cornell University. He was always willing to support me and give me advice of my study and research. On the academic level, Prof. Ober taught me fundamentals of my research project. On the personal level, Prof. Ober inspired me by his patience and hardworking attitude. I could never imagine having a better advisor and mentor for my research. Besides my advisor, I would like to thank Prof. Robert Shepherd as my thesis committee, for his encouragement and insightful comments.

My sincere thanks also goes to Hong Xu, for teaching me experimental skills from synthesis to evaluation. Without his guidance, I would not finish the project independently. I would also thank Yiren and Kazunori for offering critical advice whenever I got problems with my research. I'm also grateful to the friendship I received from all of Ober's group members during my graduate life. Thanks are also due to the JSR Corporation for the financial support and I otherwise would never be able to do such a great research project. Last, but not least, I would like to express my deepest gratitude to my family and friends for their warm love, continued patience and endless support.

CONTENTS

CHAPTER 1

INTRODUCTION

1.1 Background

1.1.1 Introduction to lithography

Since being invented in the 1960s, lithography has become an indispensable and important process for large-scale integrated circuits. According to Moore's law proposed by G. Moore in 1965[1], the amount of integrated circuit transistors doubles around every two years.

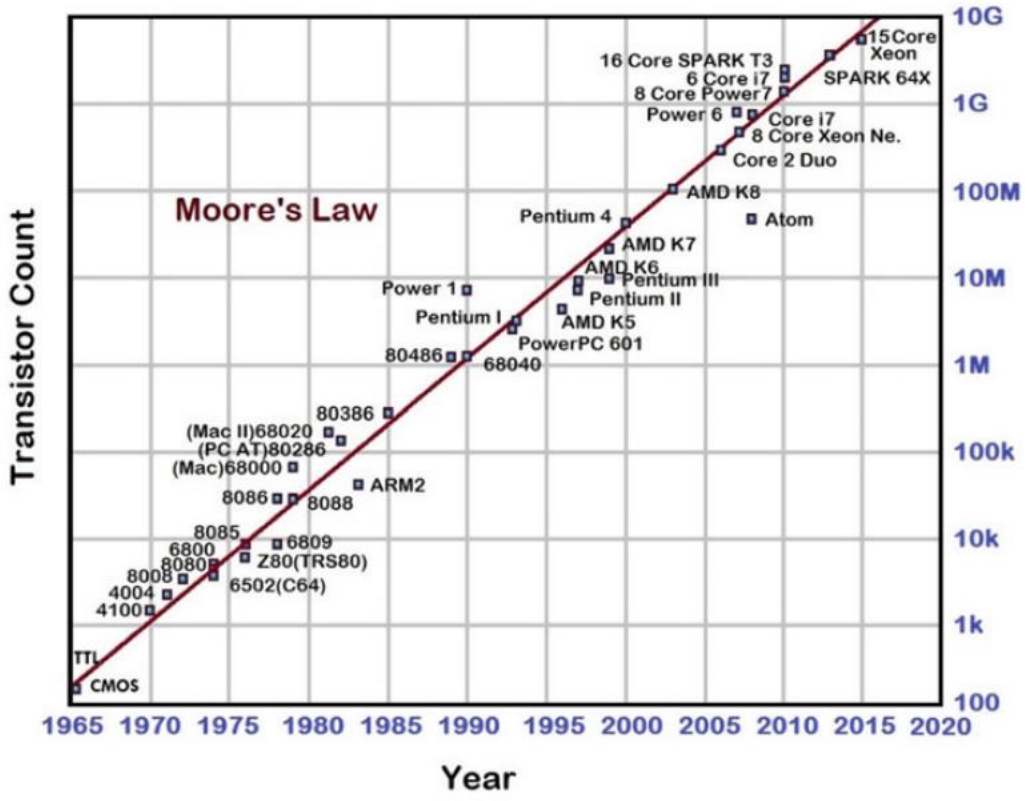

Figure 1.1. Transistor count trend for microprocessors.[2]

As shown in Figure 1.1, integrated circuits have evolved from just a few dozen devices per chip in the 1960s to billions of devices per chip today[2]. The rapid development of integrated circuits is closely related to the reduction in the physical size of individual devices, which is directly determined by lithography techniques. The continuous development of lithography technology provides two guarantees for the advancement of integrated circuit technology. Firstly, a large -area of uniform exposure enables a large number of devices and chips to be simultaneously fabricated on the same silicon wafer, which ensures high volume manufacturing. Secondly, the reduction of the line width significantly accelerates the operating speed of the device.

Conventional lithography is a technique that combines exposure and etching to transfer a nanoscale integrated circuit pattern onto the surface of the substrate through a series of processes. The manufacture of integrated circuits is a large and complex system. Chip manufacturing refers to permanently etching a complete set of integrated circuits on a wafer by means of replication. Known as photolithography, this process is the core of integrated circuit manufacturing. As shown in Figure 1.2, it mainly includes wafer pre-treatment, coating, pre-bake, exposure, development, post bake, etch, implantation and resist strip[3].

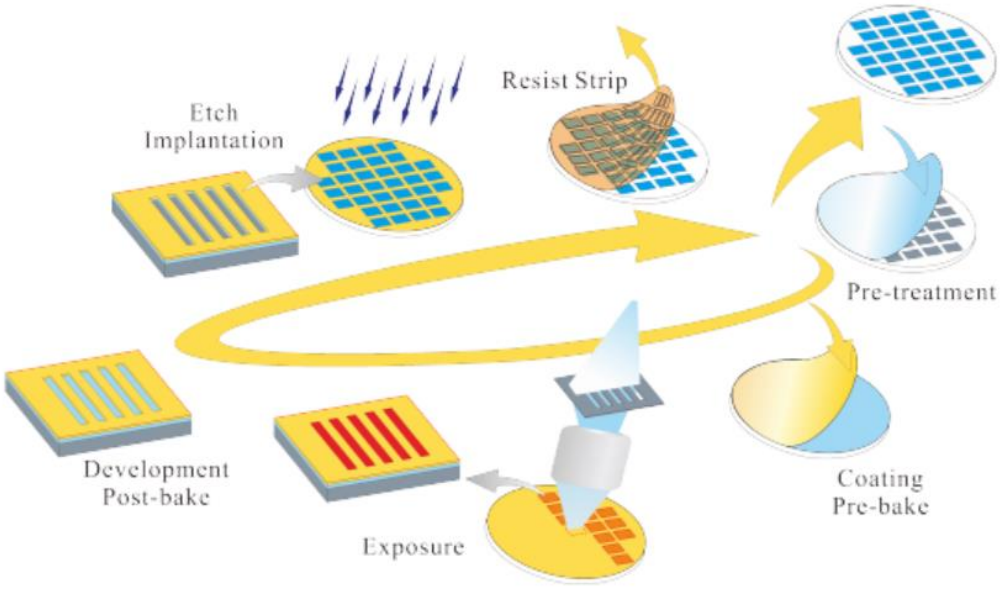

Figure 1.2. Traditional lithography process.[3]

Wafer pretreatment is to clean and dry the wafers, while surface treatment is to improve the state and characteristics of the wafer surface. In order to enhance the adhesion, sometimes it is necessary to deposit other film layers. Spin coating and pre-baking are used to cover the surface of the wafer with photoresist. Other methods commonly used are spray coating, flow coating and roll coating. Pre-baking is mainly done to eliminate the solvent in the photoresist and enhance the adhesion between the film and the wafer. After alignment, the target area on the wafer is irradiated through the mask and the objective lens system, causing a photochemical reaction of the photoresist. Development places the exposed wafer in its corresponding developer to remove any unnecessary portions (an exposed portion is removed for the positive-tone photoresist and unexposed portion is removed for the negative-tone photoresist). The wafer is taken out, post-baked and the pattern formed by the photoresist is cured to resist the harsh environment in the subsequent etching and doping processes. The region on the wafer that is not protected by the photoresist is etched and doped, so the

mask pattern is transferred and cured onto the wafer. Then the residual photoresist on the wafer is removed to obtain a clean, mask-patterned wafer, which theoretically means the end of the entire lithography process (regardless of the actual wafer inspection or other non-lithographic principle processes such as multiple exposures).

Implementation of the lithography process is inseparable from the lithography tool, photoresist and etching process. The exposure light source is a core component in the composition of the lithography machine. And the photoresist is the key material used in the photolithography process. In order to meet the demand for nanoscale devices, many resolution enhancement techniques have been developed. For example, 193 nm immersion lithography, 157 nm F_2 lithography and electron beam lithography.

193 nm immersion lithography has become a hot topic in nano-device lithography. This technique uses water instead of air between the optical lens and the wafer, like that of a conventional lithography machine which reduces the wavelength of the exposure source and increase large lens numerical apertures (NA), which leads to increased resolution and extended dry lithography. In 193 nm immersion lithography, pure water is preferred as the best immersion medium, which can make the NA value as high as 1.35. An interesting topic is how to further increase the refractive index of the water system in the early stage. The principal method is to add various inorganic ions and some surfactants to the water[4]. Because of direct contact with the photoresist, the water will penetrate into the film, which may cause the polar substances contained in the photoresist to be dissolved. This will not only cause defects in photoresist patterns, but also contaminate the water itself or even corrode the lens that comes in contact with it. Therefore, the disadvantage of water as an immersion liquid needs to

be compensated by further coating a top layer on the surface of the photoresist or improving the performance of the photoresist itself.

157 nm F_2 lithography[5] was widely considered to be another promising technology following 193 nm ArF lithography. In the early period (1999-2000), 90 nm technology node was considered to be the goal of 157 nm lithography. In 157 nm lithography, most organic materials (resist) are degraded and serious additive contamination is generated due to the irradiation of high-energy light, which will cause environmental pollution. In addition, silicon surface absorption and air leakage of the optical system can cause contamination. Overall, the biggest technical obstacle to the application of 157 nm lithography technology was from environmental pollution control and the design and processing of the projection optical system.

Pollution control of the optical system could be achieved by exhaust gas purification technology[5]. For the exposure system light path, it must be purged with an inert gas to ensure maximum transmission of the 157 nm line. Oxygen and water vapor entering the optical system should be excluded due to absorption of 157 nm radiation. Volatile and non-volatile hydrocarbons can cause contamination on the surface of optical lenses and must be eliminated. It has been found that an appropriate amount of oxygen in the optical path is beneficial for cleaning the optical lens with 157 nm radiation. Therefore, introducing a small amount of oxygen into the optical system allows the optical path to be cleaned.[5]

Electron beam lithography is another next-generation lithography technology because of its high resolution, stable performance, powerful function and relatively low price.[6] This direct write lithography originated from scanning electron microscopy.

Since the invention of the first electron beam exposure machine in the 1960s[7], many products have been developed and the functions have been continuously improved. In general, the direct-write exposure machine works by moving the precisely focused beam spot on the sample stage point by point. Its lens tube system consists mainly of an electron beam source, a deflection system, a switch baffle and a precisely positioned sample stage.

In combination with the etching and deposition process, direct-type exposure technology can be used to prepare 20 nm or finer patterns. The principle nano-electronic devices with a minimum size of 10 nm have also been achieved[8]. Due to ultra-high resolution of the direct-write exposure technology, it does not require expensive projection optics and time-consuming mask preparation, which endows it with great advantage in micro- or nano- processing. However, since the direct-write exposure process scans the electron beam spot point by point on the surface, each pixel of the graphic needs to stay for a certain time period, which limits the speed of the pattern exposure. The bottleneck in capacity of write-through electron beam lithography makes it exist as an auxiliary technology in the microelectronics industry, mainly used in mask preparation, prototyping, preparation and development of small batch devices.

1.1.2 Introduction to Extreme Ultraviolet (EUV) lithography

Following that discussed above, electronics and semiconductor industries continues to pursue smaller feature size, moving toward sub-10 nm resolution.

Based on Rayleigh's Equation[9], system resolution (CD) is determined by,

$$CD = k_1 \frac{\lambda}{NA}$$

Where k_1 is a constant ranging from 0.3 to 0.8, NA is the numerical aperture of the projection system and λ is the wavelength of the light source. Therefore, the system resolution is directly proportional to the light wavelength. The smaller wavelength of the light source is necessary in order to get a smaller feature size with perfect resolution. For this reason, wavelengths of light sources successfully decreased from 390~700 nm (visible light) to 157 nm in throughout the history of photolithography. In the past twenty years, semiconductor industries have been relying on immersion lithography with a wavelength of 193 nm. With 193 nm immersion technology, multiple patterning steps are necessary to create a smaller feature size, leading to higher cost and expenditure in high volume manufacturing (HVM).

Under the demand of printing smaller feature size in a single step, next generation lithography technologies such as Extreme Ultraviolet lithography (EUVL) have attracted scientists' attention. In the late 1980s, researchers in Japan and the United States first proposed the concept of EUVL[10], using soft X-rays in the range of 10 to 30 nm as projection lithography sources. With a new manufacturing process, EUVL is completely different from the 193 nm projection lithography system. The wavelength of the light source is only 13.5 nm. Because almost all of the materials absorb light of this wavelength, the exposure process must be performed in high vacuum. Photolithographic projection is performed using a reflective mask instead of a conventional transmissive mask.[11-12]

In the early 1980s, the concept of EUVL originated from soft X-ray imaging studies with wavelengths of 4 ~ 40 nm in Japan and the United States. In 1982, when the g-

line lithography machine was just in the practical stage, X-ray Proximity Lithography (XPL) was considered the best alternative lithography to achieve a target etch resolution of 0.5 μm. However, due to the difficulties in mask manufacturing, XPL was replaced by X-ray micro imaging technology. In 1984, H. Kinoshita of Nippon Telegraph and Telephone Corporation (NTT) developed a miniature exposure system based on Schwarzschild structure. In 1985, 4 μm resolution was successfully obtained. Point arrays were published at the annual meeting of the Japan Society of Applied Physics in 1986[13]. Three years later, H. Kinoshita presented the first 0.5 μm feature with the Schwarzschild objective and reflective mask at the 33rd International EIPB Symposium. Among scientists, it was hailed as "the dawn of the EUVL"[14]. The following year, diffraction-limited horizontal imaging of 50 nm lines was obtained by American Alcatel-Lucent Bell Labs using a Schwarzschild objective lens coated with a Mo/Si multilayer film under extreme ultraviolet light with a wavelength of 14 nm[15].

The EUV system consists of four main components, a reflective projection exposure system, a reflective photolithography reticle, an extreme ultraviolet light source system and a lithographic coating that can be used for extreme ultraviolet. The imaging principle is that extreme ultraviolet light waves, with a wavelength of 10 to 14 nm, are projected onto a reflective reticle through a periodic multilayer mirror. The reduced projection system projects the integrated circuit geometry on the reflective reticle into the photoresist on the surface of the silicon wafer to form a lithographic pattern required for integrated circuit fabrication.[16]

To achieve the industrialization of EUVL, EUV objective systems must develop towards higher resolution. A number of companies and institutions including

Lawrence Livermore National Laboratory (LLNL), Nikon, Carl Zeiss and Oxford have conducted extensive research in this area. In the industrialization process of EUVL, EUV LLC of the United States invested in the development of the engineering test prototype ETS (Engineering Test Stand) in 2011. The objective lens system is made up of four mirrors with the image side numerical aperture of 0.088. A 24×32.5 mm full field exposure is realized by step scanning, which accelerates the commercialization of EUVL[17]. A decade later, ASML is the world's largest manufacturer of lithography equipment and is currently the backbone of the EUVL industrialization.

ASML introduced the first EUVL industrial test prototype ADT (Alpha Demo Tool) in 2006 with an NA of 0.25 and a resolution of 32 nm[18]. In 2010, by upgrading the lithography platform to TWINSCAN NXE, reducing flare and optimizing lighting parameter, the NXE 3100 was successfully developed. This tool is able to achieve a resolution of 27 nm and successfully increases the energy of the light source to achieve a yield of 60 WPH (Wafers per Hour)[19]. The NXE 3300 B developed in 2012 increased the objective NA to 0.32 and adopted a high-efficiency ring illumination system to further increase the yield and achieve exposure of 22 nm lines. In February 2015, Taiwan Semiconductor Manufacturing Company (TSMC) announced the use of the NEX 3300 B to achieve a daily exposure of 1022 wafers, marking a milestone in EUVL industrialization. ASML's industrialization process for EUVL is still advancing, dominating the field of EUVL equipment and even the entire lithography equipment production market.

With the light source wavelength of 13.5 nm, smaller features become possible to be printed in a single step. However, the biggest roadblock of EUV lithography is its low source power and therefore low throughput. To improve the efficiency of EUV lithography, the first principle strategy is to intensify the EUV power source. At present, the power level of the light source is approximately 10 W, which is far less than 200 W power level required for mass production[20]. If applied to the 16 nm node, a more powerful light source is needed. The feasibility of greatly improving the power level of the light source is not optimistic.

The traditional lithography machine that works in air has its limit in resolution. At the EIPBN conference in June 2001, Michael Switkes and M. Rothchild from MIT applied the immersion lens to the objective lens design of the F_2 lithography machine for the first time[21]. In 2002, the immersion lens was applied to the objective lens design of the ArF lithography machine, leading the ArF lithography machine to higher resolution. High refractive index liquid fills the lens, the resist and the silicon wafer, resulting in the numerical aperture NA ≈1.3. However, the immersion lens type ArF (193nm) lithography machine still faces many problems, such as: (1) stability of liquid optical parameters; (2) liquid bubble (cavity) problem; (3) the interaction between liquid, gas and silicon wafer.

Compared to EUV and ArF of the same power density in the same volume, the EUV photon number is much less than the ArF photon number (less than one tenth of the latter). It can be seen from the cross-sectional view of the photon distribution (Figure. 1.3) that as the line width decreases and the illuminance decrease, the number

of photons per unit area becomes smaller and the unevenness of the distribution increases, thereby causing noise in the photon distribution[22].

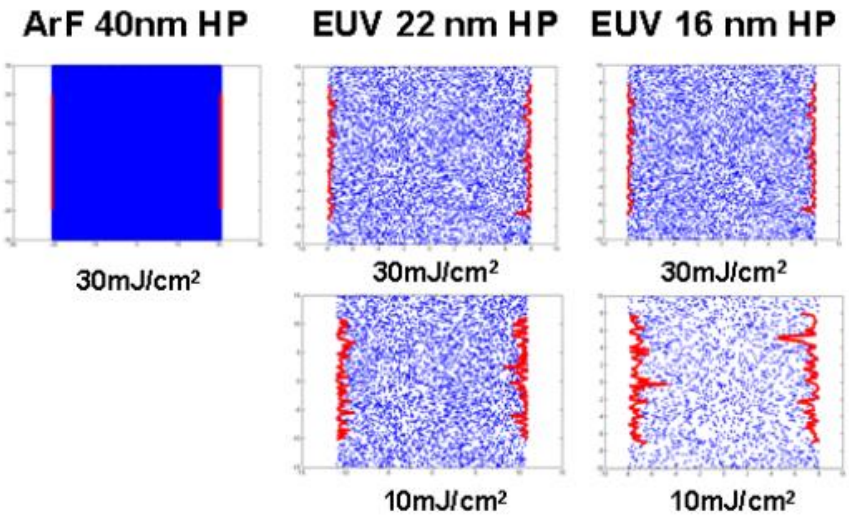

Figure 1.3. Comparison of shot noise (EUV vs. ArF).[22]

EUV is capable of ionizing irradiated materials. Different elemental atoms have different EUV absorption cross sections. Taking the commonly used chemically amplified resists (CAR) as an example, EUV exhibits non-selective absorption and the matrix material contributes the most to EUV absorption[23]. In the ArF system, the matrix exhibits transparency and the functional group of photo acid generation (PAG) directly absorbs a certain amount of light to produce an exposure effect.

In addition to developing high power light source systems, the other challenge of EUV lithography is the fabrication of mask substrates with low defect densities. High-power EUV lasers are the premise for EUV lithography to achieve mass production of chips, so the development of light sources has become the key to reduce the cost of EUV lithography machines. The design of the extreme ultraviolet light source is difficult, because the existing laser has a low output power in the extreme ultraviolet range, which does not meet the energy requirements of EUV lithography. The biggest

difficulty in developing a EUV light source is to reduce the pollution of particles in plasma, simultaneously avoiding the rapid deterioration of the light source while increasing the power of the EUV source[24].

Another major challenge of EUV lithography is to fabricate reflective masks that meet the requirement of nanoscale lithography, non-fatal defects and multilayer reflective film structures. High-precision mask defect correction techniques[25], such as electron beam localized gasification and ion milling, are often used in the fabrication process. Although EUV lithography technology faces many challenges, its developing potential is favored by many companies and scholars[26]. EUV is considered to be the main technology capable of meeting the future 16 nm production requirements.

From another perspective, the development of high-sensitivity EUV lithography materials can help to meet the high requirements on the power of the light source. Therefore, another strategy is to enhance sensitivity of photoresist materials without the loss of high resolution and pattern Line Edge Roughness (LER), which is the main focus of this work.

1.1.3 Introduction to photoresists

The development of lithography technology relates closely to the development of lithography materials which determines the development and application of lithography technology to a certain extent. Photolithography materials, also known as photoresists, are the most critical functional chemistry materials involved in lithography. These materials have light sensitive chemistry (including visible light, ultraviolet light, electron beam, etc.). By photochemical reaction, their solubility will

change in the developer. Developing on the photochemical reaction mechanism, the photoresist can be either positive or negative. If after exposure, the solubility of the photoresist in the developer increases, generating the same pattern as the mask, it is called a positive photoresist. In contrast, if the photoresist solubility reduces or even becomes insoluble in the developer after exposure, so a pattern opposite to the mask is obtained, it is known as a negative photoresist. Positive and negative photoresists are applied in different fields. Generally, positive photoresists are more common, accounting for more than 80% of the total photoresist industry.

In 1954, Eastman-Kodak Company produced the world's first photoresist made of synthetic poly(vinyl cinnamate)-based negative photoresist[27], which was also the first photoresist used in the electronics industry. The principle of the photopolymerization is shown in Figure 1.4: The double bond in the cinnamoyl group is opened by ultraviolet light and the double bonds on different molecules interact to form a four-membered ring, resulting in photo-dimerization crosslinking. In this way, the molecules in the exposed region are crosslinked to form a poorly soluble bulk network structure, while molecular properties of unexposed regions remain unchanged, microfabrication is performed by utilizing these characteristics.

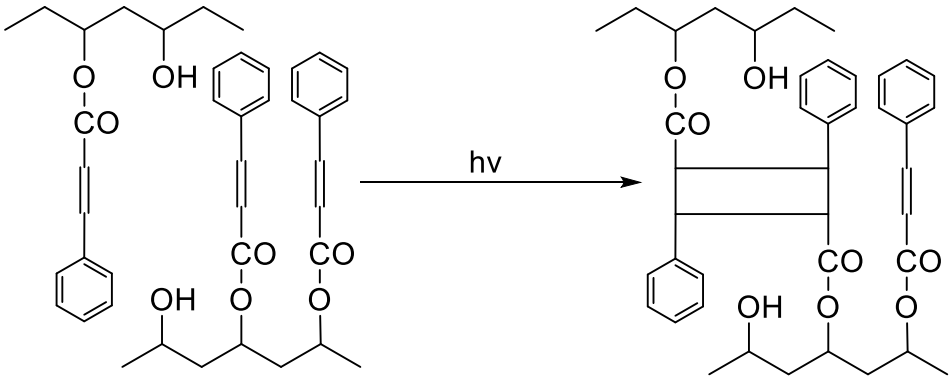

Figure 1.4. Dimerization reaction of Poly (vinyl cinnamate).

With the advantages of a long storage period, high sensitivity and good resolution (about 3 μm), the photoresist is mainly used for the preparation of integrated circuits and electronic components. It is also suitable for micro-pattern processing in the production of printed circuit boards, metal signs, optical instruments and precision measuring tools, while the poor adhesion on silicon wafers limits its wide application in the electronics industry.

In 1958, the Kodak Company[28] developed a cyclized rubber-diazido negative photoresist (sensing range 280~460 nm). Due to good adhesion on the silicon wafer, the photoresist had the advantages of fast photo-speed, minimum exposure of 3 mJ/cm^2, sensitivity range of 300~400 nm and strong resistance to wet etching. Based on these strengths, this material became the main photoresist used in the electronics industry, accounting for 90% of the total consumption at that time. The photo-polymerization principle is as shown in Figure 1.5. This type of photoresist uses a cyclized rubber with a double bond group as a film-forming resin. The the aromatic diazido compound is used as a crosslinking agent under ultraviolet light. The azido group decomposes into a nitrene, and then the nitrene takes up hydrogen on the molecular skeleton of the polymer to generate a radical, which causes cross-linking between different film-forming polymer molecules to become an insoluble network[27].

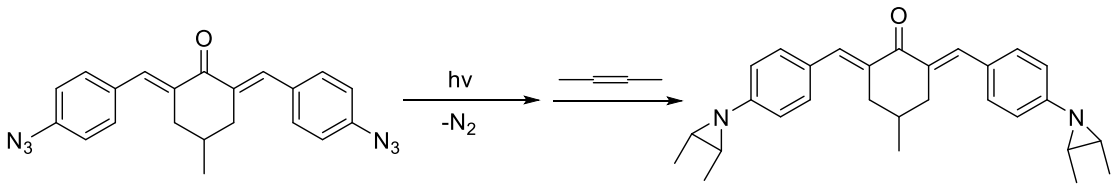

Figure 1.5. The mechanism of photo-polymerization of cyclized rubber-diazido photoresist.

These rubbers are mainly used in the fabrication of discrete devices of 5 μm, with 2-3 μm integrated circuits. However, with the reduction of processing line width in the microelectronics industry, the application of this series of negative adhesives in integrated circuit fabrication has been gradually reduced.

1.1.4 Introduction to EUV photoresists

According to International Technology Roadmap for Semiconductors (ITRS)[29], the goal of mass production of EUVL lithography materials includes low radiant bleed air, minimal contamination of the projection optics and complete removal of contamination. Resolution, sensitivity and Line Edge Roughness (LER) are three performance parameters of lithographic materials. A promising EUV photoresist should realize high resolution (line width ≦ 22 nm), great sensitivity under exposure (sensitivity ≦10 mJ/cm^2) and low LER (LER ≦ 1.5 nm). However, as shown in Figure 1.6, there is a trade-off among the three principal photoresist performance targets[30].

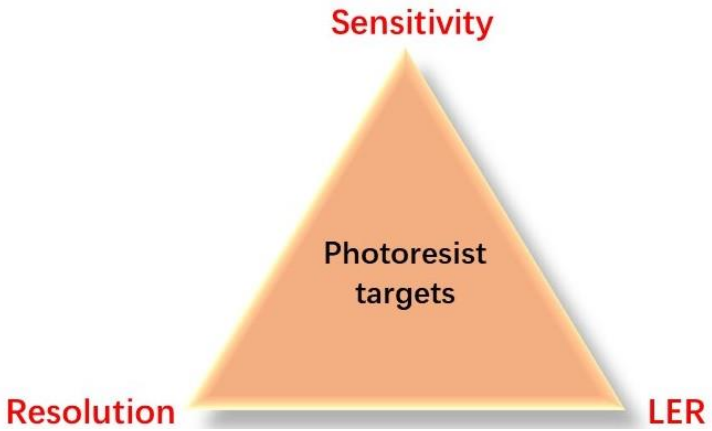

Figure 1.6. Trade-off among three principal photoresist performance targets.[30]

As introduced above, the most conventional and industrialized photoresists are built on polymers. One of the current most commercially used photoresists are chemically-amplified resists (CARs), consisting of a polymer with acid sensitive groups (such as tertiary esters), photo-acid generator (PAG), base and solvent[31-32]. In the early 1980s, the lithography process based on the concept of chemical amplification greatly accelerated the development of lithography[33]. The term *chemical amplification* means that under the action of light, a strong acid is generated by decomposition of a photo-acid generator and an acid sensitive portion of the host resin is decomposed into an alkali-soluble group under heat. Because of the solubility difference, some parts of the resin dissolve to obtain a positive or negative image. Figure 1.7 displays a specific example of a chemically-amplified positive-acting photoresist[34-35]. The t-Boc-protected p-hydroxystyrene (t-Boc-PHS) decomposes under the action of photoacid to produce alkali-soluble p-hydroxystyrene.

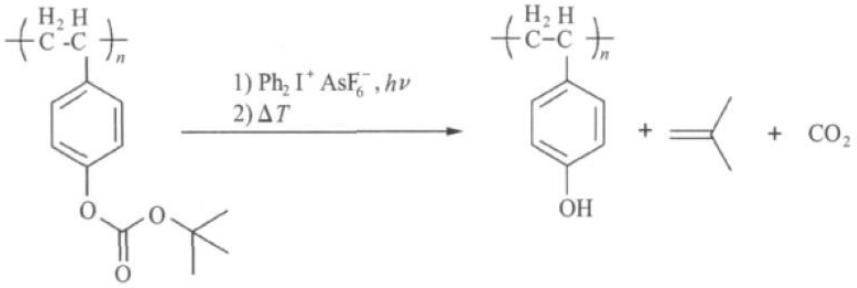

Figure 1.7. Chemically amplified positive-tone photoresist.[34-35]

Photo-acid generators are divided into two groups: ionic and nonionic[35]. Generally, the solubility of ionic PAG is inferior to that of non-ionic. Non-ionic PAG can significantly improve its thermal stability by introducing suitable sterically hindered groups at specific positions in the molecular structure. But compared to ionic PAG,

light sensitivity of non-ionic PAG is poor, thus it needs a greater light intensity and longer exposure time.

With high exposure sensitivity, CARs are very suitable for EUVL, whose exposure power is limited by the light source capability. For example, the Ober group developed a system of silicon-containing positive-tone polymers used in EUV patterning in 2003[36]. When exposed to light, PAG will decompose and form a strong acid, triggering the polymer chain to produce an acidic product, and then the solubility change. Experimental measurements show that the acid can trigger the reaction repeatedly like a catalyst. However, boundary blurring effects exists between exposed and unexposed regions caused by acid diffusion. Therefore, the resolution and LER do not meet the requirements.

In order to limit the acid diffusion of PAG in CAR and improve the uniformity of dispersion of PAG in matrix materials, James W. Thackeray et al. from Dow Corporation proposed in 2011[37] to bind PAG anionic groups to polymer branches by covalent bonding, forming a polymer-PAG integrated lithography material (Figure 1.8).

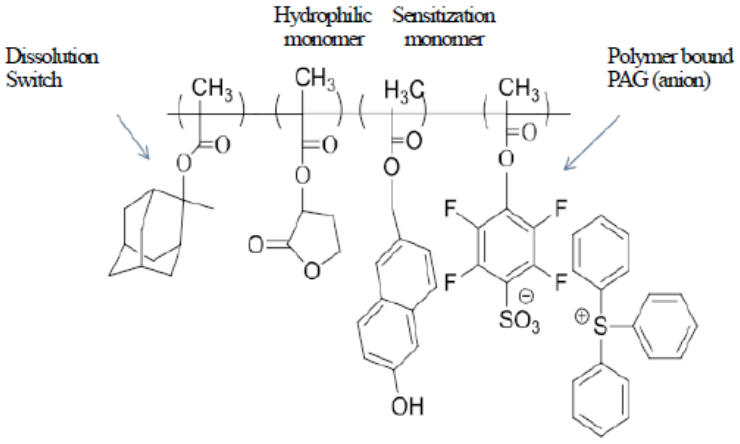

Figure 1.8. Traditional polymer PAG blend resist and PBP resist.[37]

Compared with conventional polymer PAG hybrid materials, the exposure sensitivity is slightly reduced to 10 mJ/cm^2 at a line width of 30 nm. But the line width roughness is greatly improved to one-half of the latter, so the resolution of the material is 22 nm or less.

In order to overcome the inherent limitations of traditional lithographic CAR materials in other ways, researchers have designed and synthesized various lithographic material systems focusing on matrix materials, PAG and exposure mechanisms. The research can be divided into two major systems, CARs and Non-CARs. Until 2009, CAR occupied about 89% of all EUV materials[38].

Using polymers as EUV photoresists, Whittaker's group and Blakey's group at the University of Queensland introduced a series of polycarbonate-based Non-Chemically Amplified EUV Resists[39](Figure 1.9). Without the use of PAG, this polymer directly absorbs photons as well as secondary electrons and then decompose under EUV exposure. Fragments with low molecular weight have higher solubility in developer, so selectively solubility has been achieved. With this design, 28.6 nm feature sizes can be created.

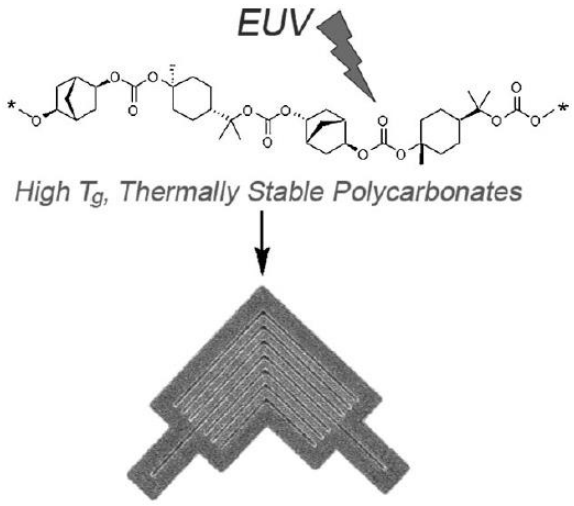

Figure 1.9. Polycarbonate-based Non-Chemically Amplified Resists.[39]

However, in the conventional EUV photoresist, the matrix material is a polymer. The molecular weight and the cluster size of a polymer are usually very large. Besides, the long molecular chains of the polymer are often entangled together, so the line width roughness is likely to be large after development. It was found that polymer chains in conventional photoresists have a root-mean-square end-to-end distance of 6-10 nm[40], which cannot be neglected compared with the decreasing target feature size. Under this notion, scientists are trying to explore EUV photoresists with no polymer involved.

In 2009, a group of researchers proposed the design of molecular glass photoresists[41], which is a small molecular weight organic material with a protective group. The organic material can be utilized to prepare a uniform and disordered amorphous film by spin coating. The size of the molecule after film formation is small and the film has a certain thermal stability (Tg > 150 °C). Later in 2010, Hiroaki Oizumi et al. from Selete reported the performance of EUV molecular glass

photoresist products provided by several companies[42]. These lithographic materials are ring-shaped resorcinol derivatives, "Noria-AD" water-wheeled molecules and fullerene derivatives. It was found that the obtained resorcinol derivative is available at a linear size of 45 nm. Clear patterns can be obtained with a line width roughness of around 5 nm. The resolution of the "Noria-AD" waterwheel molecule and fullerene derivative with a large molecular weight is improved compared with the cyclic resorcinol derivative and a clear pattern is obtained when the line width is 28 nm. But with a small line width, the pattern collapses and deformations are severe, so it is difficult to achieve a resolution of 22 nm line width for the above molecular glass photoresists.

Recently, a completely new resist system was developed by Montgomery et al. from the University of Birmingham in 2017[43]. Based on the concept of Multi-trigger, this system has been given the name “Multi-Trigger Resist”. Figure 1.10 shows the schematic mechanism difference between traditional chemically amplified approach and multi-trigger approach.

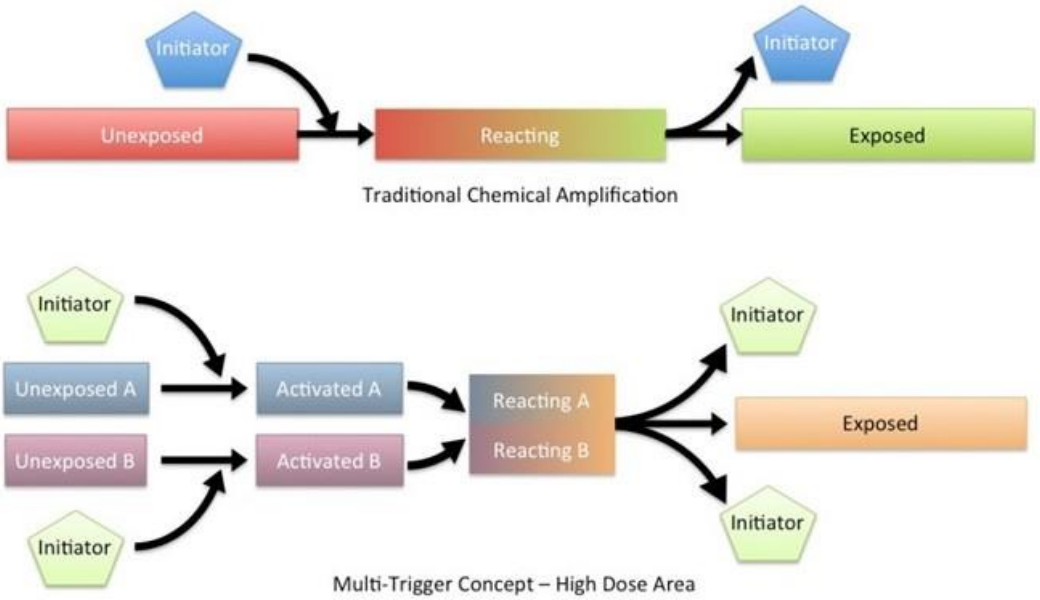

Figure 1.10. Mechanism of traditional chemically amplification and multi-trigger approach.[43]

In conventional chemically amplified photoresist mechanisms, an initiator (or PAG) reacts with the photoresist to cause cross-linking during exposure, which changes the solubility of the photoresist. The photoacid after the reaction is usually collected to participate in the next reaction. In multi-trigger resists systems, however, multiple initiators trigger multiple acid sensitive molecules. These molecules act as multiple reaction centers and react with each other, ensuring high reaction efficiency and high sensitivity. Supported and reported by Irresistible Materials (IM), this system has demonstrated results of 25 nm patterns at an exposure dose of 11.4 mJ/cm^2.

1.1.5 Introduction to metal-organic-based EUV photoresists

Among the emerging platform of non-polymer-based EUV photoresists, another novel EUV photoresists system that rose to prominence was metal oxide-based EUV

photoresists. Launched by Inpria Corporation, 13 nm lines and space patterns with the sensitivity of 35 mJ cm^{-2} have been achieved[44]. Researchers from Brainard's group at State University of New York Polytechnic Institute reported metal oxide EUV photoresists with different metals (Co, Fe and Cr)[45]. Additionally, Zr oxide and Hf oxide resists demonstrating high sensitivity and resolution were investigated by Ober's group at Cornell[46-51]. The photoresist developed by Ober's group is based on a metal oxide hybrid nanoparticle with the diameter of 2-5 nm. A schematic structure of the nanoparticle is shown in Figure 1.11.

Figure 1.11. Schematic structure of metal-oxide hybrid nanoparticle.[46-51]

The exposure intensity of this type of photoresist can be as low as 10% of that of current photoresist, creating the possibility for the semiconductor chip industry to continue Moore's Law[52]. These metal-based nanoparticles surrounded by organic matter, show low line edge roughness, high sensitivity and high resolution in line within industry requirements.

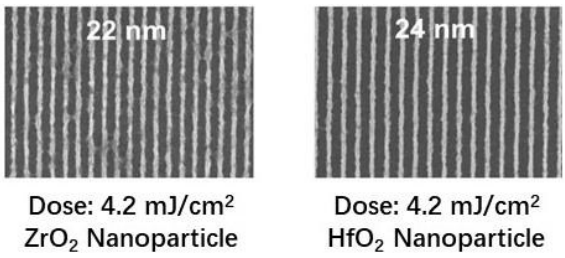

Figure 1.12. SEM images of Zr- and Hf-based nanoparticle exposed by EUV. [46-51]

Shown in Figure 1.12, the nanoparticle photoresist with a core-shell structure composed of an inorganic zirconium- or hafnium- oxide and an organic ligand exhibits excellent patterning ability under EUV exposure. Among the Zr-based photoresist, the Zirconia-Methacrylic Acid nanoparticle photoresist can reduce the feature size of the pattern to 22 nm under the exposure dose of 4.2 mJ/cm^2, which is only 10% of the commercial photoresist exposure dose, indicating a high productivity under the existing low EUV exposure power. Because the yield per unit time is the most important indicator of the economics of modern semiconductor production technology, these photoresists with high sensitivity, low line-edge roughness and high-resolution may lead the development of a next generation EUV photoresist.

1.2 Motivation

1.2.1 Motivation of zinc-based EUV photoresists

Regarding what has been introduced above about the EUV photoresists developed by Ober's group, Zr- and Hf- based nanoparticles give out promising over-all-performance. With significantly higher etch resistance and smaller particle size, these nanoparticle photoresists show excellent lithographic performance using DUV, e-beam and EUV exposure.

However, the Zr and Hf are relatively low EUV absorbing metals.[53] Therefore, integration of high EUV absorption elements is considered to be one promising route to further improve lithographic performance under EUV radiation. Under this notion, a series of photoresists was developed, using the high EUV absorption element Zn as the metal core. Zinc has shown higher EUV photo-absorption compared to both

zirconium and hafnium, and thus has a greater potential to achieve the high-sensitivity desired for EUV lithography (Figure 1.13).[54]

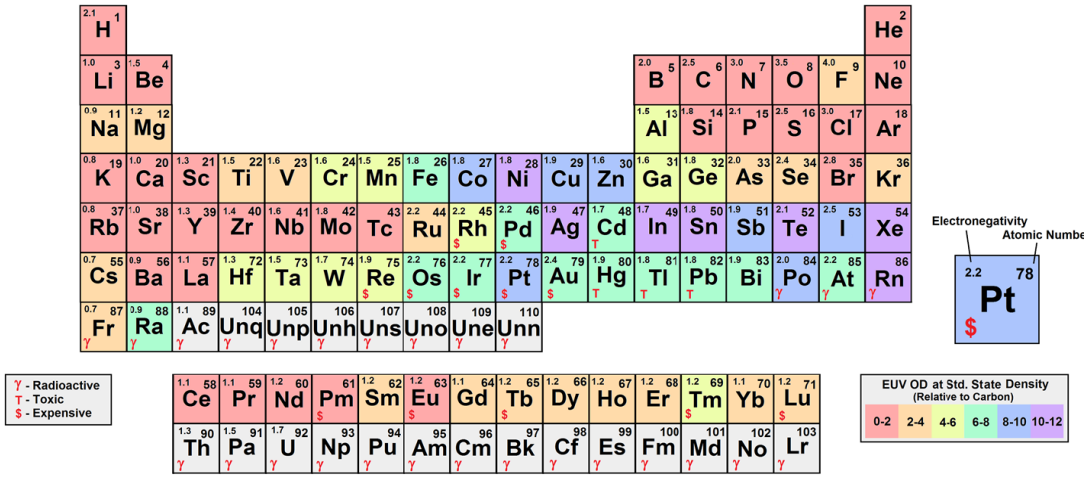

Figure 1.13. EUV optical density of the elements.[53]

As a continuation of the previous Zr- and Hf- based EUV photoresist work, Xu[52] et al. from Ober's group has reported some promising results of Zn-based nanoparticles. With the nanoparticle size as small as 1.6 nm, sub-15 nm patterns were successfully achieved by means of EUV lithography (Figure 1.14).[52]

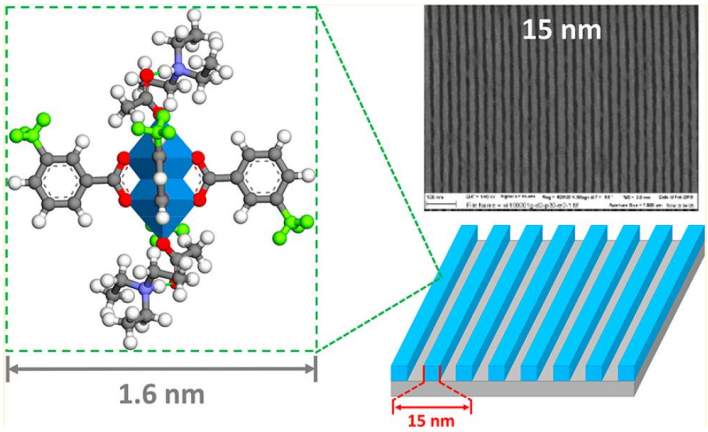

Figure 1.14. Zn-based nanoparticle and SEM image after EUV exposure.[52]

Based on Xu's work, a set of Zn-based photoresists was prepared through a similar approach used for ZrO_2 and HfO_2. These metal-oxide nanoparticles have a ZnO core and an organic shell consisting of an acid ligand and base ligand. The zinc-based photoresist possesses small particles size, good solubility in spin-coating solvents, excellent film-forming capabilities and pattern formation under UV and e-beam radiation.

REFERENCES

1. Moore, G., Cramming more components onto integrated circuits. *Electronics*, **1965**, *18*(8): 114-117.
2. Amiri, I.S., Mohammadi, H. and Hosseinghadiry, M., Invention and Evaluation of Transistors and Integrated Circuits. *Device Physics, Modeling, Technology, and Analysis for Silicon MESFET*, **2019**:1-9.
3. Levinson, H.J., *Principles of lithography*, **2005**, *146*.
4. Taylor, J.C., Shayib, R., Goh, S., Chambers, C.R., Conley, W., Lin, S.H. and Willson, C.G., Fluids and resists for hyper NA immersion lithography. *Proc. SPIE*, **2005**, *5753*: 836-847.
5. Mulkens, J., McClay, J.A., Tirri, B.A., Brunotte, M., Mecking, B. and Jasper, H., Optical lithography solutions for sub-65-nm semiconductor devices. *Proc. SPIE*, **2003**, *5040*: 753-763.
6. Fontana, R.E., Katine, J., Rooks, M., Viswanathan, R., Lille, J., MacDonald, S., Kratschmer, E., Tsang, C., Nguyen, S., Robertson, N. and Kasiraj, P., E-beam writing: a next-generation lithography approach for thin-film head critical features. *IEEE Trans. Magn.*, **2002**, *38*(1): 95-100.
7. Rai-Choudhury, P., *Handbook of microlithography, micromachining, and microfabrication: microlithography*, **1997**, *1*.
8. Khoury, M. and Ferry, D.K., Effect of molecular weight on poly (methyl methacrylate) resolution. *J. Vac. Sci. Technol. B*, **1996**, *14*(1): 75-79.
9. Lin, B.J., Where is the lost resolution? *Proc. SPIE*, **1986**, *633*: 44-51.

10. Hawryluk, A.M. and Seppala, L.G., Soft x-ray projection lithography using an x-ray reduction camera. *J. Vac. Sci. Technol. B*, **1988**, *B6*: 2162.
11. Silfvast, W.T. and Wood II, O.R., Tenth micron lithography with a 10 Hz 37.2 nm sodium laser. *Microelectron Eng.*, **1988**, *8*: 3-11.
12. Kinoshita, H., Kurihara, K., Ishii, Y. and Torii, Y., Soft x-ray reduction lithography using multilayer mirrors. *J. Vac. Sci. Technol. B*: Microelectronics Processing and Phenomena 7, **1989**, *B6*: 1648-1651.
13. Kinoshita, H., Kaneko, T., Takei, H., Takeuchi, N. and Ishihara, S., Study on X-ray reduction projection lithography. *47th Autumn Meeting Japan Society of Applied Physics*, **1986**, *28*-ZF: 15.
14. Kinoshita, H., Kurihara, K., Ishii, Y. and Torii, Y., Soft x-ray reduction lithography using multilayer mirrors. *J. Vac. Sci. Technol. B*, **1989**, *7*(6): 1648-1651.
15. Bjorkholm, J.E., Bokor, J., Eichner, L., Freeman, R.R., Gregus, J., Jewell, T.E., Mansfield, W.M., Mac Dowell, A.A., Raab, E.L., Silfvast, W.T. and Szeto, L.H., Reduction imaging at 14 nm using multilayer-coated optics: Printing of features smaller than 0.1 μm. *J. Vac. Sci. Technol. B*, **1990**, *8*(6): 1509-1513.
16. Lin, M.W., Hellebusch, D.J., Wu, K., Kim, E.K., Lu, K.H., Liechti, K.M., Ekerdt, J.G., Ho, P.S. and Willson, C.G., Role of surfactants in adhesion reduction for step and flash imprint lithography. *J. Micro-Nanolith. MEM.*, **2008**, *7*(3): 033005.
17. Tichenor, D.A., Ray-Chaudhuri, A.K., Lee, S.H., Chapman, H.N., Replogle, W.C., Berger, K.W., Stulen, R.H., Kubiak, G.D., Klebanoff, L.E., Wronosky, J.B. and

O'Connell, D.J., Initial results from the EUV engineering test stand. *Soft X-Ray and EUV Imaging Systems II*, **2001**, *4506*: 9-19.

18. Meiling, H., Meijer, H., Banine, V., Moors, R., Groeneveld, R., Voorma, H.J., Mickan, U., Wolschrijn, B., Mertens, B., van Baars, G. and Kürz, P., First performance results of the ASML alpha demo tool. *Emerging Lithographic Technologies X*, **2006**, *151*: 615108.
19. Wagner, C., Harned, N., Kuerz, P., Lowisch, M., Meiling, H., Ockwell, D., Peeters, R., van Ingen-Schenau, K., van Setten, E., Stoeldraijer, J. and Thuering, B., EUV into production with ASML's NXE platform. *Proc. SPIE*, 2010, *7636*: 76361H.
20. Wurm, S., Transition to EUV lithography. Proceedings of the 2012 International Symposium on VLSI Technology, Systems and Application (VLSI-TSA), **2012**.
21. Prasher, R.S. and Phelan, P.E., Non-dimensional size effects on the thermodynamic properties of solids. *Int. J. Heat Mass Transf.*, **1999**, *42*(11): 1991-2001.
22. Kim, H.W., Na, H.S., Cho, K.Y., Park, C.M., Yasue, T., Mayya, S. and Cho, H.K., Patterning with EUVL: the road to 22nm node. *Proc. SPIE*, **2010**, 76*36*: 76360Q.
23. Kozawa, T. and Tagawa, S., Radiation chemistry in chemically amplified resists. *Jpn. J. Appl. Phys.*, **2010**, *49*(3R): 030001.
24. Keij, S., Setija, I., Van der Zouw, G. and Ebert, E., Advances in phase-grating-based wafer alignment systems. *Proc. SPIE*, **2005**, 5752: 948-961.
25. Fadavieslam, M.R., Shahtahmasebi, N., Rezaee-Roknabadi, M. and Bagheri-Mohagheghi, M.M., Effect of deposition conditions on the physical properties of

SnxSy thin films prepared by the spray pyrolysis technique. *Journal of Semiconductors*, **2011**, *32*(11): 113002.

26. Lepson, J.K., Beiersdorfer, P., Clementson, J., Gu, M.F., Bitter, M., Roquemore, L., Kaita, R., Cox, P.G. and Safronova, A.S., EUV spectroscopy on NSTX. J. Phys. B, **2010**, *43*(14): 144018.
27. Minsk, L.M. and Van Deusen, W.P., Eastman Kodak Co, Photomechanical resist. *U.S. Patent*, **1954**, *2*, 690,966.
28. Martin, H. and Wagner, H.M., Eastman Kodak Co, Azide resin photolithographic composition. *U.S. Patent*, **1958**, *2*,852,379.
29. Hoefflinger, B., ITRS: The international technology roadmap for semiconductors. *Chips 2020*, **2011**, 161-174.
30. Kim, J., Lee, J.W., Kim, D. and Kim, J., Measurement of EUV resists performances RLS by DUV light source. *Proc. SPIE*, **2010**, *7636*: 76362Y.
31. Kruit, P. and Steenbrink, S.W.H.K., Local critical dimension variation from shot-noise related line edge roughness. *J. Vac. Sci. Technol. B*, **2005**, *23*(6): 3033-3036.
32. Saeki, A., Kozawa, T., Tagawa, S. and Cao, H.B., Correlation between proton dynamics and line edge roughness in chemically amplified resist for post-optical lithography. *J. Vac. Sci. Technol. B*, **2006**, *24*(6): 3066-3072.
33. Ito, H. and Willson, C.G., Chemical amplification in the design of dry developing resist materials. *Polym. Eng. Sci.*, **1983**, *23*(18): 1012-1018.
34. MacDonald, S.A., Willson, C.G. and Frechet, J.M., Chemical amplification in high-resolution imaging systems. *Acc. Chem. Res.*, **1994**, *27*(6): 151-158.

35. Shirai, M. and Tsunooka, M., Photoacid and photobase generators: chemistry and applications to polymeric materials. *Prog. Polym. Sci.*, **1996**, *21*(1): 1-45.

36. Dai, J., Ober, C.K., Wang, L., Cerrina, F. and Nealey, P.F., Organoelement resists for EUV lithography. *Proc. SPIE*, **2002**, 4690: 1193-1202.

37. Thackeray, J.W., Jain, V.J., Coley, S., Christianson, M., Arriola, D., LaBeaume, P., Kang, S.J., Wagner, M., Sung, J.W. and Cameron, J., Optimization of polymer-bound PAG (PBP) for 20nm EUV lithography. *J. Photopolym. Sci. Tec.*, **2011**, *24* (2): 179-183.

38. Koh, C., Georger, J., Ren, L., Huang, G., Goodwin, F., Wurm, S., Ashworth, D., Montgomery, W., Pierson, B., Park, J.O. and Naulleau, P., Characterization of promising resist platforms for sub-30 nm HP manufacturability and EUV CAR extendibility study. *Proc. SPIE*, **2010**, *7636*: 763604.

39. Yu, A., Liu, H., Blinco, J.P., Jack, K.S., Leeson, M., Younkin, T.R., Whittaker, A.K. and Blakey, I., Patterning of tailored polycarbonate based non-chemically amplified resists using extreme ultraviolet lithography. *Macromol. Rapid Commun.*, **2010**, *31*: 1449–1455.

40. Patsis, G.P., Constantoudis, V. and Gogolides, E., Effects of photoresist polymer molecular weight on line-edge roughness and its metrology probed with Monte Carlo simulations. *Microelectron. Eng.*, **2004**, *75*: 297-308.

41. Lawson, R.A., Tolbert, L.M. and Henderson, C.L., Single component molecular resists containing bound photoacid generator functionality. *Proc. SPIE*, **2009**, *7273*: 72733C.

42. Oizumi, H., Matsumaro, K., Santillan, J., Shiraishi, G., Kaneyama, K., Matsunaga, K. and Itani, T., Development of EUV resists based on various new materials. *Proc. SPIE*, **2010**, 7639: 76390R.
43. Montgomery, W., McClelland, A., Ure, D., Roth, J. and Robinson, A.P., Irresistible materials multi-trigger resist: the journey towards high volume manufacturing readiness. *Proc. SPIE*, **2017**, *10143*: 1014328.
44. Stowers, J., Anderson, J., Cardineau, B., Clark, B., De Schepper, P., Edson, J., Greer, M., Jiang, K., Kocsis, M., Meyers, S. and Telecky, A., Metal oxide EUV photoresist performance for N7 relevant patterns and processes. *Proc. SPIE*, **2016**, *9779*: 977904.
45. Grzeskowiak, S., Narasimhan, A., Murphy, M., Napolitano, L., Freedman, D.A., Brainard, R.L. and Denbeaux, G., Reactivity of metal-oxalate EUV resists as a function of the central metal. *Proc. SPIE*, **2017**, 10146:1014605.
46. Bae, W.J., Trikeriotis, M., Rodriguez, R., Zettel, M.F., Piscani, E., Ober, C.K., Giannelis, E.P. and Zimmerman, P., High-index nanocomposite photoresist for 193-nm lithography. *Proc. SPIE*, **2009**, *7273*: 727326.
47. Chakrabarty, S., Sarma, C., Li, L., Giannelis, E.P. and Ober, C.K., Increasing sensitivity of oxide nanoparticle photoresists. *Proc. SPIE*, **2014**, *9048*: 90481C.
48. Yu, M., Xu, H., Kosma, V., Odent, J., Kasahara, K., Giannelis, E. and Ober, C., Positive Tone Nanoparticle Photoresists: New Insight on the Patterning Mechanism. *J. Photopolym. Sci. Tec*. **2016**, *29*(3): 509-512.

49. Kasahara, K., Xu, H., Kosma, V., Odent, J., Giannelis, E.P. and Ober, C.K., Nanoparticle photoresist studies for EUV lithography. *Proc. SPIE*, **2017**, *10143*: 1014308.

50. Xu, H., Kosma, V., Giannelis, E.P. and Ober, C.K., In pursuit of Moore's Law: polymer chemistry in action. *Polymer J.*, **2018**, *50*(1): 45.

51. Kasahara, K., Xu, H., Kosma, V., Odent, J., Giannelis, E.P. and Ober, C.K., Recent Progress in EUV Metal Oxide Photoresists. *J. Photopolym. Sci. Tec*., **2017**, *30*(1): 93-97.

52. Xu, H., Sakai, K., Kasahara, K., Kosma, V., Yang, K., Herbol, H.C., Odent, J., Clancy, P., Giannelis, E.P. and Ober, C.K., Metal-organic framework-inspired metal-containing clusters for high resolution patterning. *Chem. Mater.*, **2018**, *30*(12): 4124-4133.

53. Henke, B.L., Gullikson, E.M. and Davis, J.C., X-ray interactions: photoabsorption, scattering, transmission and reflection E= 50-30,000 eV, Z= 1-92. *At. Data Nucl. Data Tables*, **1993**, *54*: 181-342.

54. Sortland, M., Hotalen, J., Del Re, R., Passarelli, J., Murphy, M., Kulmala, T.S., Ekinci, Y., Neisser, M., Freedman, D.A. and Brainard, R.L., Platinum and palladium oxalates: positive-tone extreme ultraviolet resists. *J. Micro-Nanolith. MEM.*, **2015**, *14*(4): 043511.

CHAPTER 2

ZINC-BASED PHOTORESIST WITH TOLUIC ACID LIGAND

2.1 Background and Motivation

Metal oxide nanoparticle-based EUV photoresists have been studied in the past several years and achieved desirable results. Compared with Zr- and Hf-based photoresists, Zn has greater photo-absorption under EUV exposure[1]. As a continuation of the previous Zr- and Hf- based EUV photoresist work, Xu[2] et al. have reported some promising results of Zn-based nanoparticles.

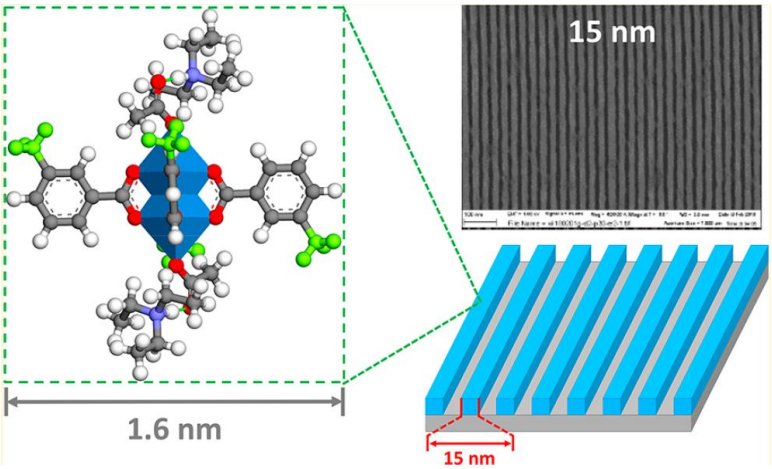

Figure 2.1. Zn-*m*TA nanoparticle and SEM image after EUV exposure.[2]

Using the *m*-toluic acid (*m*TA) as acid ligands, Xu successfully shrank the nanoparticle size to 1.6 nm, even smaller than the reported smallest Zr-based or Hf-based nanoparticle photoresist (2 nm).[3-8] With this ultra-small particle size, sub-15 nm patterns were successfully achieved by means of EUV lithography[2] (Figure 2.1). In terms of resolution, Zn-*m*TA gives better performance than the 22 nm resolution Zr- or Hf-based photoresist.[3-8] However, Zn-*m*TA shows poorer performance in sensitivity

compared to Zr- and Hf-based photoresists. In order to achieve sub-15 nm patterns, 47 mJ cm^{-2} is needed[2], 10 times larger than the sensitivity of Zr- and Hf-based photoresists (4.2 mJ cm^{-2}).[3-8]

Based on Xu's work, a set of Zn-based photoresists with toluic acid (ZnO-TA-NPs) as ligands were prepared. Through a similar approach that Xu used, the Zn-*m*TA nanoparticle was further optimized, and then the *m*-toluic acid was replaced with *o*-toluic acid and *p*-toluic acid. Compared to *m*-toluic acid, *p*-toluic acid has a smaller steric hindrance, while *o*-toluic acid has a bigger steric hindrance. From a rough calculation, the energy and stability of these three nanoparticles are also quite different.

These structures were used to identify the best performance of these toluic acid-based photoresists, especially resolution and sensitivity. The lithographic evaluation process can be divided into several basic steps: spin coating, exposure, development, etch and photoresist stripping. A scheme of the lithography process is illustrated in Figure 2.2.

First, the photoresist film is spin coated onto the prepared silicon wafer. Then the substrate is irradiated, and the photoresist in the exposed region undergoes a chemical reaction. The pattern on the reticle is then transferred to the photoresist by development. Finally, the etch technique is utilized to transfer the pattern onto the substrate and the photoresist is stripped.

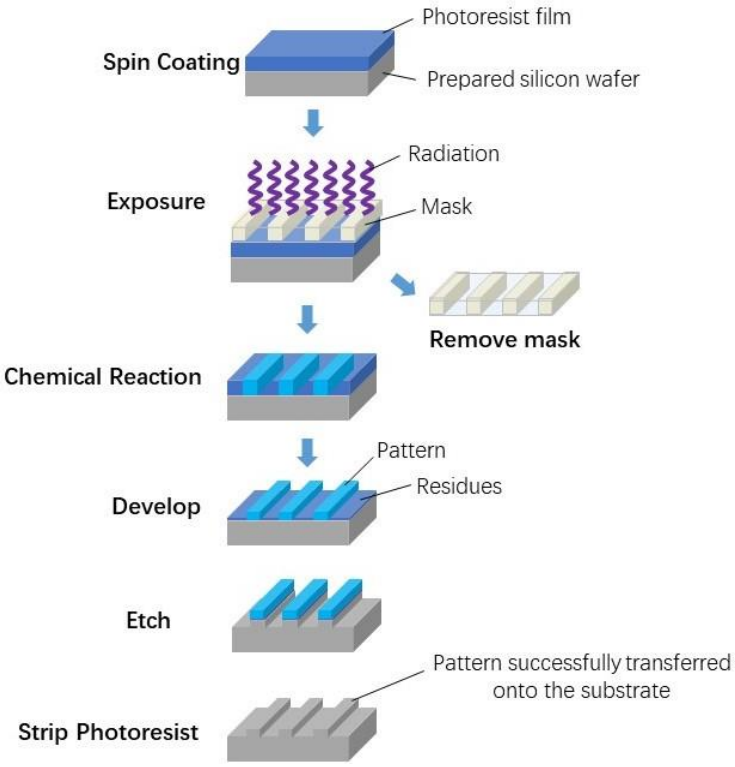

Figure 2.2. Scheme of lithography process.

Spin coating uniformly coats a layer of photoresist on a wafer substrate, requiring the photoresist to adhere well and evenly. Generally, the wafer is first placed on the vacuum chuck of a spin coater. Then the liquid photoresist is dropped on the center of the wafer and rotating at a high speed. The centrifugal force helps to evenly coat the photoresist onto the silicon wafer. Different photoresists require different spin coating conditions, such as initial slow rotation (e.g. 500 rpm), followed by a jump to a maximum speed of 3000 rpm or higher. Crucial quality indicators for some photoresist applications are time, speed, thickness and uniformity. Improper spin coating parameters may cause particle contamination and photoresist defects, such as pinholes. In this experiment, filtrated photoresist solution was spin coated directly onto a silicon wafer at 2000 rpm for 60 seconds, accelerating with 400 rpm/sec to form a thin and

uniform film. A soft bake is necessary after spin coating, in order to remove the solvent from the photoresist. In addition, the soft bake helps to improve adhesion, uniformity of the photoresist on the silicon wafer and provides better line width control during etching.

Exposure is then conducted after soft bake. The mask is aligned with the correct position on the spin coated wafer. The mask and the wafer are exposed and the mask pattern is transferred to the silicon wafer with photoresist. Light energy activates the photosensitive component in the photoresist. The important quality indicators for alignment and exposure are line-space resolution and overlay accuracy. In this experiment, wafers were exposed at Cornell NanoScale Science and Technology Facility (CNF) using ABM Contact Aligner stepper or ASML DUV stepper at a desired dosage to apply a pattern onto the photoresist. The operating details of these two exposure instruments will be introduced in the experimental section.

After exposure, each wafer is cut into ~2 cm^2 pieces for development and each piece is submerged in the specific developer for a set length of time. Development is a critical step in creating a pattern in the photoresist. Soluble areas on the photoresist are dissolved by the chemical developer leaving visible islands or window patterns on the surface of the wafer. For synthetic photoresists, the developer is often unknown and needs to be identified. A common strategy is to start from the weakest developer, and then move on to stronger ones. Developer will directly determine the efficiency of pattern transfer. For negative photoresists, if a developer is too weak it will not dissolve the unexposed portion to a good extent. In contrast, if the developer is too strong, not only the unexposed portion but also the exposed area will be dissolved. In

both cases, no pattern can be successfully transferred onto the photoresist. The most common development methods are spinning, spraying and wetting. Once the photoresist is patterned on the silicon wafer, an inspection is needed to find quality problems in the photoresist and to evaluate the process performance of the photoresist with regard to the specifications.

2.2 Experimental Section

2.2.1 Materials

Chemicals and solvents were purchased from Aldrich and used without further purification unless otherwise indicated. Ethyl acetate was purchased from Fisher Scientific, decahydronaphthalene was purchased from Beantown Chemical and Chloroform-D was purchased from Cambridge Isotope Laboratories Inc. Silicon wafers used for lithographic purposes were purchased from Pure wafer and used as received [Diameter: 100 mm; Type/Dopant: p/Boron**;** Res: 10 - 20 ohm-cm**;** Thickness: 500 - 550 µm].

2.2.2 Synthesis

ZnO-*o*TA-NP: In a 100 mL round-bottomed flask, zinc acetate dihydrate (4.38 g, 0.02 mol), *o*-Toluic acid (5.44 g, 0.04 mol) and triethylamine (3.06 g, 0.03 mol) were mixed, followed by addition of 50 mL ethyl acetate. The reaction mixture was stirred at 65^{o}C for 15 hours. The solvent was removed with a rotary evaporator at 65^{o}C and the residue was further dried under vacuum for 6 hours. The final product, ZnO-*o*TA-NP, was obtained as a transparent gel.

ZnO-*m*TA-NP and **ZnO-*p*TA-NP** were synthesized with a similar method as ZnO-*o*TA-NP, *m*-Toluic acid and *p*-Toluic acid were used in exactly the same molar amount as *o*-Toluic acid.

2.2.3 Characterization

^{1}H NMR spectra were recorded at the Cornell Chemistry NMR Facility on a Varian INOVA 400 spectrometer at 400 MHz in order to characterize the structure of products. Samples were dissolved in Chloroform-D under 2 mg/mL concentration.

Dynamic light scattering (DLS) spectroscopy was measured on Malvern Zetasizer Nano 90 at Cornell NanoScale Facility (CNF) in order to evaluate the hydrodynamic diameter of the nanoparticles dispersed in the solvent. A SEMI-MICRO disposable cuvette cell was used during measuring. Testing temperature was set to be 25°C

Quartz Crystal Microbalance (QCM) was utilized to examine the film dissolution rate and to compare dissolution difference before and after exposure. The QCM test solution contains 5 wt% photoresist and PGMEA as solvent. And this test was conducted under room temperature.

2.2.4 Lithography process

Sample preparation: To make photoresist solution before measuring, a controlled amount of zinc-based photoresist (10 wt% of solution) synthesized as above was dissolved in PGMEA, photo-acid generator (PAG) was added at an amount of 10 wt% of photoresist. The mixture was then stirred for 5 minutes and filtrated by a 0.2 μm syringe filter. A spin coater quartz crystal with double-faced adhesive tape was used

for film preparation. The spin coating procedure was at 2000 rpm for 60 seconds, accelerating with 400 rpm/sec to form a thin and uniform film. Soft bake was conducted after spin coating under a certain temperature. Soft bake temperature varies for different zinc-based nanoparticles, which will be discussed in the next chapter.

Mid-UV exposure was performed by ABM Contact Aligner. The exposure mirror was changed to 254 nm light mirror and the exposure time was calculated based on the dosage needed for the exposure. For standard 150 mJ cm^{-2} dosages, 20.3s was used as exposure time.

Deep-UV (DUV) exposure was performed by ASML 300C DUV Stepper at the wavelength of 248 nm. Reticle Box D was used for DUV exposure. The first few steps were program editing, Batch ID setting and Job Name selecting. In this experiment, the job name is “users/bj39/psm”. “CNF T1” was used as mask the exposure dose was set to 150 mJ cm^{-2}.

Electron-Beam (E-Beam) evaluation was performed using a JEOL JBX9500FS Electron Beam Lithography System. Current of the E-beam evaluation was 500 pA and the exposure energy was 100 $\mu C/cm^2$. A full 4-inch wafer coated with zinc-based photoresist was used.

Extreme Ultraviolet (EUV) exposure was conducted using EUV tools at Paul Scherrer Institute (PSI). DUV exposure conditions were used for EUV exposure guidance, but parameters were varied during EUV evaluation.

Development and pattern evaluation: Each wafer was cut into ~2 cm^2 pieces for development and each piece was submerged in the specific developer for a set length of time. The silicon wafer was dried with a nitrogen gun and patterns were examined

under an optical microscope. After obtaining the optimal patterns, further pattern evaluation was conducted using a scanning electron microscope (SEM). Optical microscope images were taken with a Nikon Digital Sight DS-5M-L1. And SEM images were taken on a Zeiss Ultra SEM.

2.3 Results and Discussion

2.3.1 Solubility and film forming

Good solubility in spin-coating solvents endows these nanoparticles with excellent film-forming ability, which is critical to the resultant film quality. To study the effects of the simple methyl substitution of ligands on the solubility of the related NPs, toluic acids with various methyl substitution (*ortho*-, *meta*-, *para*-) were used in our synthesis to give three nanoparticle (NP) samples, namely ZnO-*o*TA-NP, ZnO-*m*TA-NP and ZnO-*p*TA-NP. As shown in Figure 2.4, all products are transparent gels and demonstrate satisfactory solubility in common spin-coating solvents, such as propylene glycol monomethyl ether acetate (PGMEA). Taking ZnO-*m*TA-NP as an example, clear and transparent solutions can be obtained even when the ZnO-*m*TA-NP concentration is increased to 40 wt%(Figure 2.4d), far exceeding the industrial requirement of 10 wt%. This excellent solubility indicates that less photoresist solution preparation time is required for ZnO-*m*TA-NP, and thus production efficiency is increased. The solubility of ZnO-*o*TA-NP and ZnO-*p*TA-NP is as good as ZnO-*m*TA-NP, which will not be presented here.

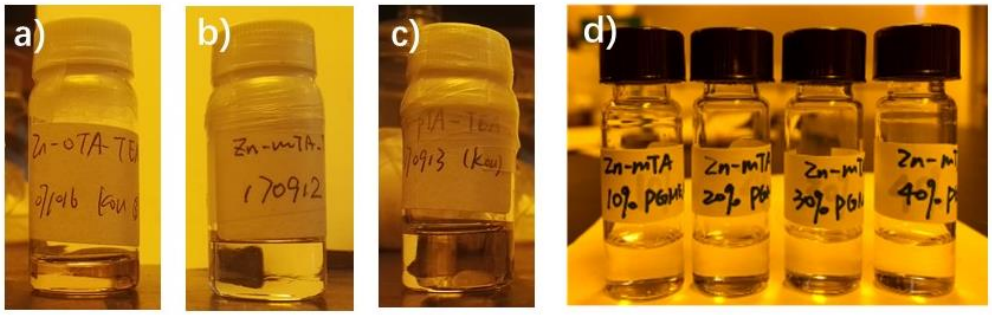

Figure 2.4. Zn-based photoresists and solubility test: a) ZnO-*o*TA-NP; b) ZnO-*m*TA-NP; c) ZnO-*p*TA-NP; d) Solubility test of ZnO-*m*TA-NP from 10% to 40%, solution: PGMEA.

As indicated in Figure 2.5, homogeneous films can be fabricated by simply spin-coating these materials from a PGMEA solution onto a silicon wafer with no observable particle aggregation when examined by optical microscope. The film forming properties of ZnO-*o*TA-NP, ZnO-*m*TA-NP and ZnO-*p*TA-NP are very similar, so only the ZnO-*m*TA-NP film is displayed here as an example. In contrast, the dispersion of bare (commercial) ZnO nanoparticles without ligation of toluic acid and base gave inhomogeneous films due to their large particle size and broad size distribution (Figure 2.5c)[9]. The undesirable film indicates that commercial ZnO nanoparticles cannot be directly used as photoresists because of their poor film forming ability. The divergence between ZnO-TA-NPs and commercial ZnO nanoparticles indicates the importance of the acid and base ligands. Only with these organic ligands can zinc oxide-based nanoparticles show good solubility in organic solvents.

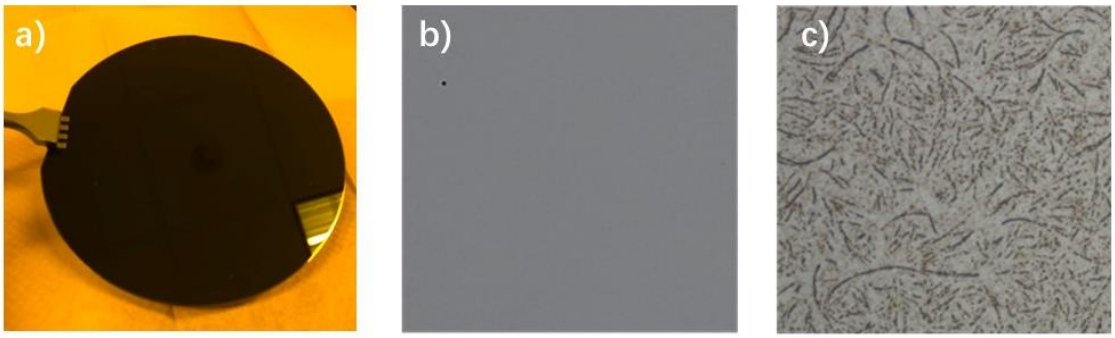

Figure 2.5. a) ZnO-*m*TA-NP film on a silicon wafer; b) Optical image of ZnO-*m*TA-NP film (the black dot is to ensure the microscope is well-focused but such defects are quite rare in spin-coating film); c) Optical image of ZnO nanoparticle film[9].

2.3.2 DLS measurement

Dynamic light scattering (DLS) is a practical method for the measurements of the particle sizes and size distribution of the NPs. As can be seen from the size distribution profile in Figure 2.6, all of the three zinc-based nanoparticles in this toluic acid system are monodisperse with a narrow distribution. The average size of ZnO-*o*TA-NP and ZnO-*m*TA-NP is around 10 nm. From computational calculation reported by Xu[2], sizes of the simulated structures of ZnO-TA-NPs is close to 2 nm. A possible reason for the size discrepancy among the three NPs is that ZnO-*o*TA-NP and ZnO-*m*TA-NP are actually clusters consisting of four or five nanoparticles. Remarkably, ZnO-*p*TA-NP (~2 nm) has a smaller average size compared to ZnO-*o*TA-NP and ZnO-*m*TA-NP, indicating ZnO-*p*TA-NP exists as nanoparticles instead of clusters.

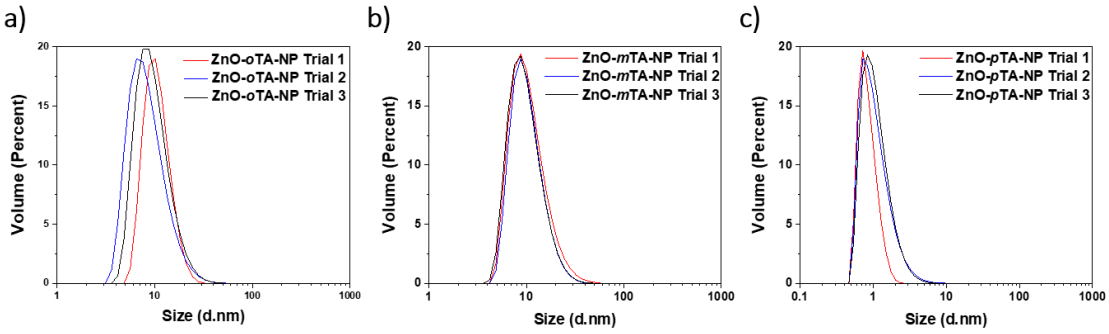

Figure 2.6. Dynamic light scattering spectra of toluic acid-based nanoparticles: a) ZnO-*o*TA-NP; b) ZnO-*m*TA-NP; c) ZnO-*p*TA-NP.

2.3.3 Mid-UV evaluation

2.3.3.1 Developer

Using exposure light with 254nm wavelength, mid-UV evaluation was conducted after photoresist solution preparation. The main purpose of mid-UV exposure is to identify the best developer for each toluic acid-based photoresist. It was found that the exposed portion of ZnO-TA-NPs became insoluble in developer. As a result, a pattern opposite to the mask was copied onto the substrate, indicating that ZnO-TA-NPs behaves as negative-tone photoresist.

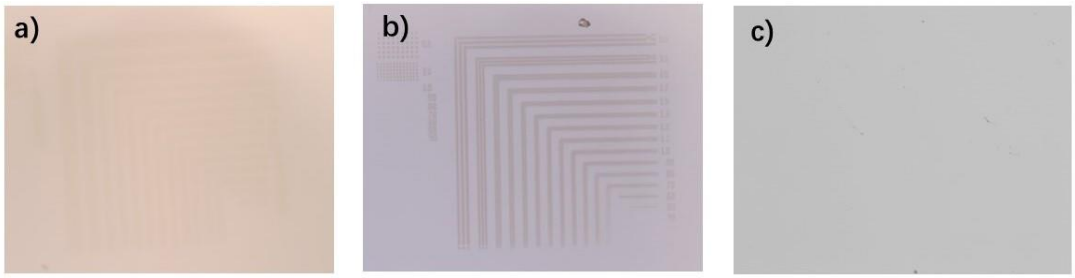

Figure 2.7. Optical microscope images of ZnO-*o*TA-NP with different developers: a) developed in hexane for 150s; b) developed in DHN for 20s; c) developed in toluene for 5s.

Different solvents were also used as developers for ZnO-TA-NPs based on their ability to dissolve the photoresist after exposure. Hexane and toluene were tested first because they are the weakest and strongest developer, respectively. Because the three photoresists in ZnO-TA-NP system have large similarities in structure, they performed very similar in this test. Therefore, only ZnO-*o*TA-NP was discussed here as an example of developer selection. Shown in Figure 2.7, no patterns formation was observed in hexane even after extended development of up to 150 s (Figure 2.7a). On the other hand, no pattern can be obtained when toluene, a stronger developer, was used because it dissolved both exposed and unexposed regions (Figure 2.7c). Later, DHN was found to be a good developer since good-quality patterns can be generated in around 20s (Figure 2.7b). It was found that DHN is also the best developer for the other two photoresists in this ZnO-TA-NP system. Figure 2.8 shows the optical microscope images of these three photoresists under optimal condition, indicating that the ZnO-TA-NP system can give desirable quality patterns after mid-UV exposure.

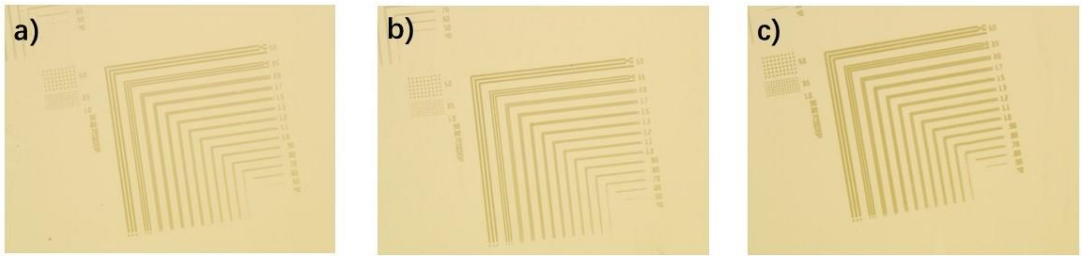

Figure 2.8. Optical microscope images of toluic acid-based photoresists developed in DHN for 20s at the exposure dose of 150 mJ cm^{-2}: a) ZnO-*o*TA-NP; b) ZnO-*m*TA-NP; c) ZnO-*p*TA-NP.

2.3.3.2 Role of PAG

For conventional metal oxide-based nanoparticle photoresists, PAGs act as a necessary component in the process of photolithography due to the poor photosensitivity of the photoresists themselves. Although photoacid generator (PAG) was introduced in the initial mid-UV evaluation (254 nm) following the conventional procedures, a series of lithography tests were also carried out on the pure ZnO-TA-NPs. Interestingly, clear patterns were obtained even without PAG, indicating the photosensitive nature of the ZnO-TA-NP photoresists (Figure 2.9). To the best of our knowledge, this is the first photosensitive Zn-based photoresist that has been reported.

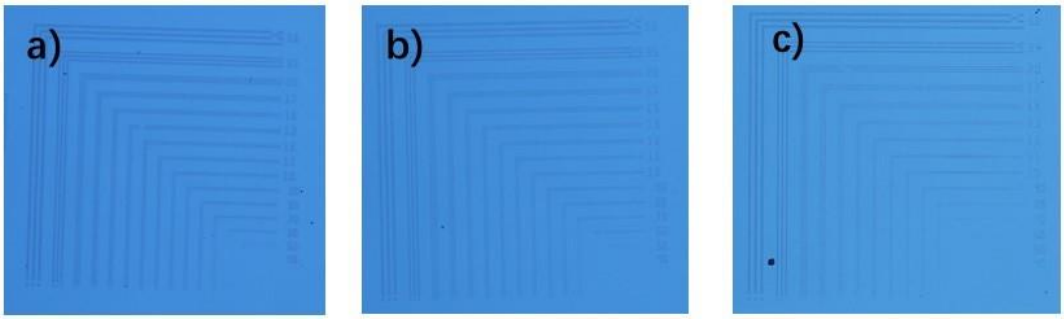

Figure 2.9. Optical microscope images of zinc-toluic acid-based photoresists without PAG at an exposure dose of 150 mJ cm^{-2}: a) ZnO-*o*TA-NP, developed in hexane for 20s; b) ZnO-*m*TA-NP developed in DHN for 20s; c) ZnO-*p*TA-NP, developed in hexane for 20s.

To further study the self-photosensitive characteristic as well as the role of PAG, ZnO-*m*TA-NP was used as a model compound for quartz crystal microbalance (QCM) experiments. QCM curves of ZnO-*m*TA-NP film with PAG both before and after exposure are shown in Figure 2.10; the result of films without PAG are also given as a control group. For the control group, there is a distinct dissolution rate change upon exposure even without PAG (Figure 2.10a). While film thickness of pure ZnO-*m*TA-NP decreased to 0 after 25 seconds with no exposure, the one with 150 mJ cm^{-2} exposure was delayed by 80% after 45 seconds. This can be explained by the decomposition of ZnO-*m*TA-NP upon light radiation and charge exposure in the initially neutral nanoparticle, which caused drastic solubility change. By comparing the ZnO-*m*TA-NP with (Figure 2.10b) and without PAG(Figure 2.10a), a more drastic solubility change was observed upon exposure. This result suggested PAG plays a large role during exposure in altering photoresist solubility.

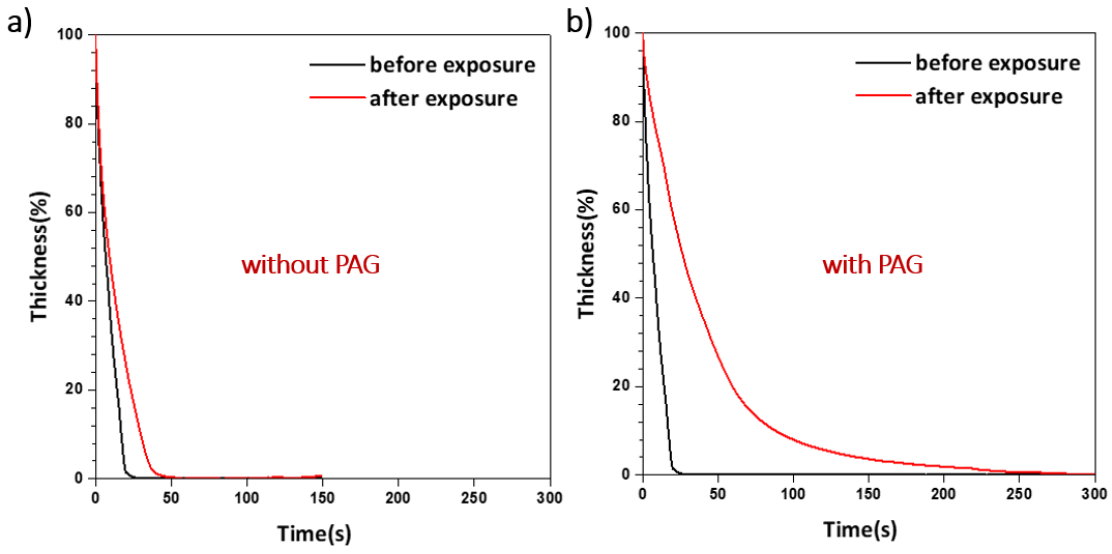

Figure 2.10. QCM curves of the ZnO-*m*TA-NP thin film before and after 150 mJ cm^{-2} DUV exposure in DHN: a) no PAG added; b) initiated by photo-acid generator (PAG).

2.3.3.3 Exposure dose

Besides the developer and the PAG, exposure energy also plays an important role in good-quality pattern formation. To study the effect of dosages on pattern formation, the three ZnO-TA-NP samples were tested with either 150 mJ cm^{-2} or 1000 mJ cm^{-2}, and the results are shown in Figure 2.11. For pure ZnO-TA-NPs, the patterns quality can be improved when higher exposure is used, which is consistent with the abovementioned proposed decomposition theory. Higher energy enables the decomposition of more zinc, thus facilitating solubility.

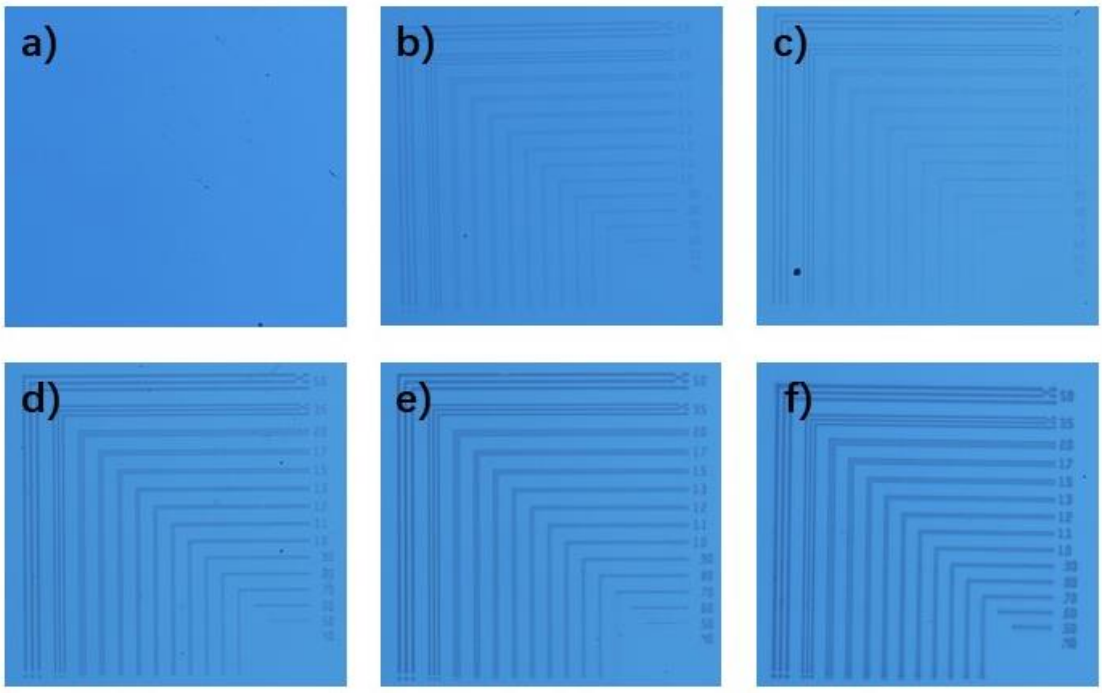

Figure 2.11. Optical microscope images of toluic acid-based photoresists developed in DHN for 20s: a) ZnO-*o*TA-NP, exposure dose: 150 mJ cm^{-2}; b) ZnO-*m*TA-NP, exposure dose: 150 mJ cm^{-2}; c) ZnO-*p*TA-NP, exposure dose: 150 mJ cm^{-2}; d) ZnO-*o*TA-NP, exposure dose: 1000 mJ cm^{-2}; e) ZnO-*m*TA-NP, exposure dose: 1000 mJ cm^{-2}; f) ZnO-*p*TA-NP, exposure dose: 1000 mJ cm^{-2};

2.3.4 DUV evaluation

After mid-UV examination, DUV evaluation was conducted with a 248 nm wavelength deep ultra-violate light source. The purpose of DUV exposure was to optimize another photolithographic parameter, the developing time. The DUV exposure mask used in this experiment contains 1:1 line and space patterns from 200 nm to 1000 nm. The closer the pattern line width to the mask geometry width, the better the developing time is. Figure 2.12 shows the SEM images of ZnO-*m*TA-NP with various developing time. When developing time was 20s, the pattern line width was 586.1 nm, which was much wider than the standard 500 nm pattern on the mask (Figure 2.12a). On the other hand, 461.9 nm patterns were obtained (Figure 2.12c) when longer developing time (60s) is used. After more attempts were made, the optimized developing time was found to be 40s, with which a pattern line width of 496.7 nm can be obtained and is within a standard deviation of the expected 500 nm pattern line width (Figure 2.12b).

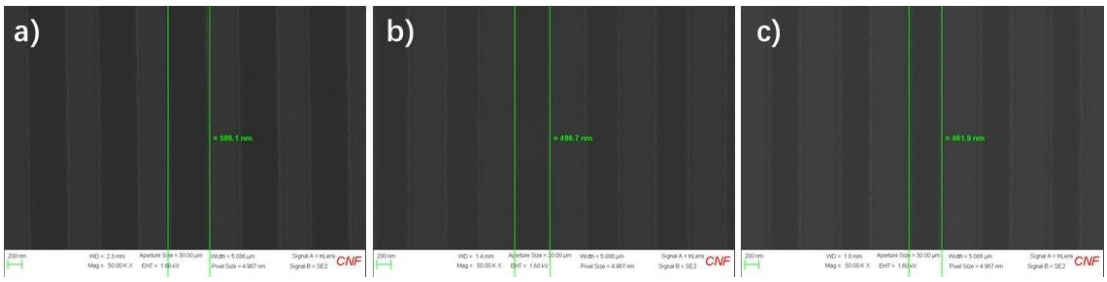

Figure 2.12. SEM images of ZnO-*m*TA-NP exposed at 150 mJ cm^{-2} and developed in DHN for different developing time: a) 20s; b) 40s; c) 60s.

By optimizing the above-mentioned factors, the generated pattern with the best resolution were obtained for all three ZnO-TA-NP samples. The detailed photolithographic parameters are presented in Table 2.3, and the corresponding SEM images are compiled in Figure 2.13. From the SEM images, no perceptible difference in formation of 250 nm patterns can be observed among the three nanoparticles. In order to further explore the resolution limit, E-beam evaluation was performed.

Table 2.3. Photolithographic parameters of ZnO-*o*TA-NP, ZnO-*m*TA-NP and ZnO-*p*TA-NP after optimization.

Sample	Photo Active Compound	Soft Bake Temperature (°C)	Developer	Developing Time (s)
ZnO-*o*TA-NP	PAG	60	DHN	50
ZnO-*m*TA-NP	PAG	80	DHN	40
ZnO-*p*TA-NP	PAG	100	DHN	40

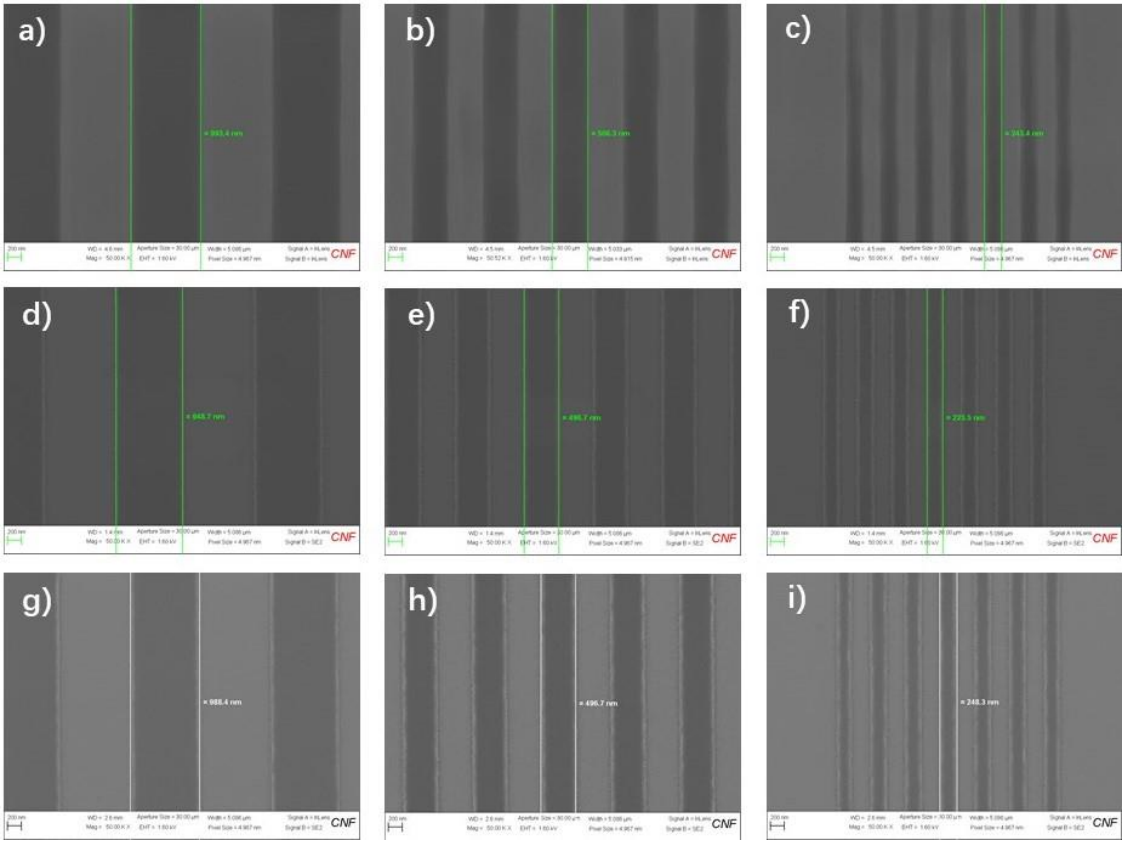

Figure 2.13. SEM images of toluic acid-based photoresists exposed at a dosage of 150 mJ cm^{-2} and developed with their best photolithographic parameters presented in Table 2.3: a) ZnO-*o*TA-NP, pattern line width: 1000 nm; b) ZnO-*o*TA-NP, pattern line width: 500 nm; c) ZnO-*o*TA-NP, pattern line width: 250 nm; d) ZnO-*m*TA-NP, pattern line width: 1000 nm; e) ZnO-*m*TA-NP, pattern line width: 500 nm; f) ZnO-*m*TA-NP, pattern line width: 250nm; g) ZnO-*p*TA-NP, pattern line width: 1000 nm; h) ZnO-*p*TA-NP, pattern line width: 500 nm; i) ZnO-*p*TA-NP, pattern line width: 250 nm.

2.3.5 E-beam evaluation-resolution

From the results discussed above, all three ZnO-TA-NP photoresists show excellent 1:1 line and space patterns under DUV exposure. However, the smallest patterns obtained through DUV exposure are 250 nm. To further evaluate their performance with resolution under 100 nm, an E-beam test was conducted.

Figure 2.14 shows the SEM images of photoresists after E-beam exposure. It was found that although ZnO-*o*TA-NP shows good resolution in DUV evaluation with the pattern line width of 250 nm (Figure 2.14c), its resolution is significantly lower when the pattern size is decreased to 100 nm and 50 nm (Figure 2.14a and Figure 2.14b) in E-beam evaluation. On the other hand, ZnO-*m*TA-NP and ZnO-*p*TA-NP show significantly better performance after E-beam exposure. The best resolution of ZnO-*m*TA-NP is believed to be 25 nm without a problem of bridging[2]. The resolution of ZnO-*p*TA-NP is even higher than that of ZnO-*m*TA-NP. As shown in Figure 2.14f-h, the SEM images of ZnO-*p*TA-NP from 35 nm to 20 nm give patterns with good shape. To conclude, ZnO-*p*TA-NP gives the best resolution in the ZnO-TA-NP system, which may be ascribed to its smaller size (~ 1nm) compared with the other two toluic-based NPs (~ 10 nm).

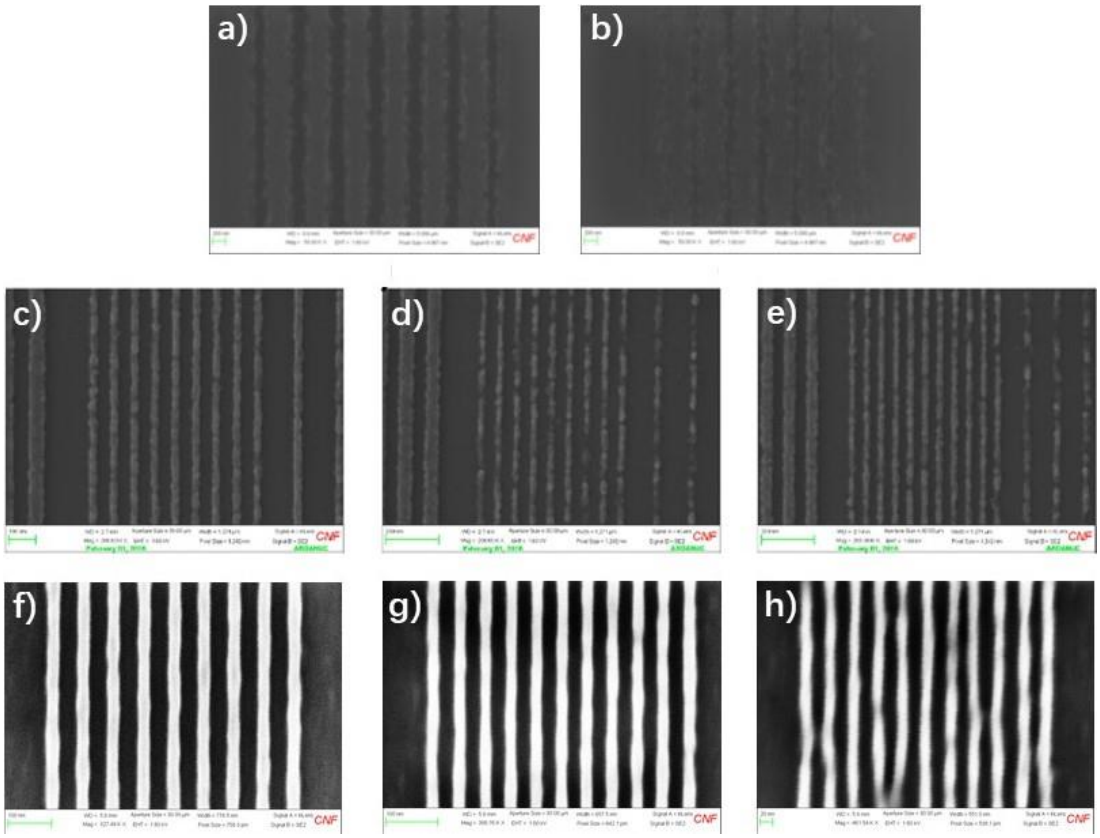

Figure 2.14. SEM images after E-beam evaluation at a dosage of 100 μC cm^{-2}: a) ZnO-*o*TA-NP, pattern line width: 100 nm; b) ZnO-*o*TA-NP, pattern line width: 50 nm; c) ZnO-*m*TA-NP, pattern line width: 35 nm; d) ZnO-*m*TA-NP, pattern line width: 30 nm; e) ZnO-*m*TA-NP, pattern line width: 25 nm; f) ZnO-*p*TA-NP, pattern line width: 35nm; g) ZnO-*p*TA-NP, pattern line width: 25nm; h) ZnO-*p*TA-NP, pattern line width: 20nm.

2.3.6 EUV evaluation

Inspired by the E-beam evaluation results, EUV exposure was conducted to further evaluate these photoresists. Due to limited opportunities and confidentiality, EUV evaluations were only carried out for ZnO-*m*TA-NP and ZnO-*o*TA-NP samples using Berkeley Microfield Exposure Tool (BMET). SEM images of ZnO-*m*TA-NP (Figure

2.15) and the contrast curve of ZnO-*o*TA-NP (Figure 2.15) were obtained. As can be seen from the SEM images in Figure 2.15, the best resolution obtained from EUV exposure is 18 nm at the exposure dose of 124 mJ cm^{-2}. Compared to the previously reported Zr- or Hf- based photoresists[10-13], the resolution and roughness are significantly improved.

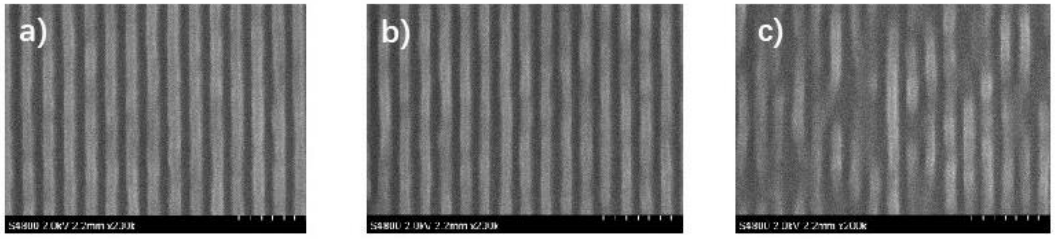

Figure 2.15. SEM images of ZnO-*m*TA-NP line-and-space dense patterns after EUV exposure at a dosage of 124 mJ cm^{-2} and developed in DHN: a) 19 nm patterns; b) 18 nm patterns; c) 17 nm patterns.

According to the contrast curve of ZnO-*o*TA-NP in Figure 2.16, the developing time increases greatly as the exposure energy increases from 0 mJ cm^{-2} to 20 mJ cm^{-2}. And the curve becomes relatively flat when the exposure dose increases from 20 mJ cm^{-2} to 100 mJ cm^{-2}. The result indicates that the sensitivity of ZnO-*o*TA-NP is around 40 mJ

cm^{-2}, which is a considerable improvement compared to ZnO-*m*TA-NP (124 mJ cm^{-2}).

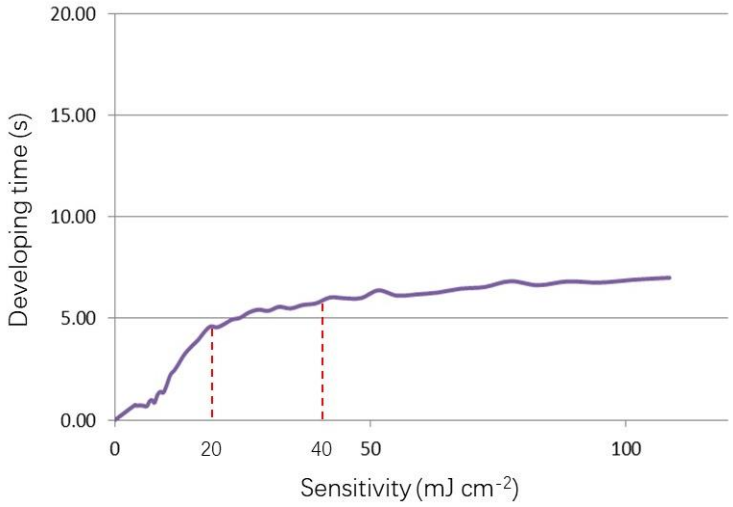

Figure 2.16. EUV evaluation contrast curve of ZnO-*o*TA-NP, developer: DHN.

2.3.7 Comparison and discussion

From the discussion above, the minor change in the substituent position can change the resolution and sensitivity of the three ZnO-TA-NP photoresists. ZnO-*p*TA-NP has the best resolution in E-beam exposure, while ZnO-*o*TA-NP shows a higher sensitivity. In order to further explore the sensitivity difference between these three photoresists, Quartz Crystal Microbalance (QCM) evaluations were conducted.

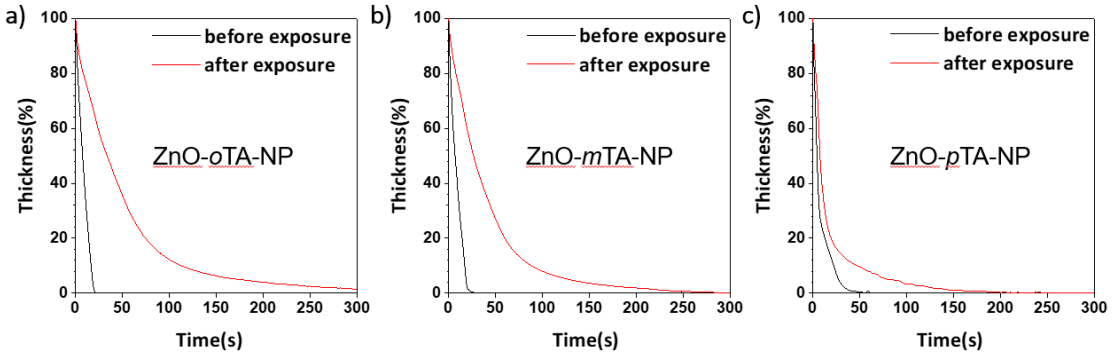

Figure 2.17. QCM curves of toluic acid-based photoresists thin film before and after DUV exposure in DHN, exposure dose: 150 mJ cm^{-2}: a) ZnO-*o*TA-NP; b) ZnO-*m*TA-NP; c) ZnO-*p*TA-NP.

Inspired by the different performance of these three photoresists, structures of these photoresists were simulated by computational calculations (Figure 2.18) with the assistance from Hong Xu[2]. On top of Figure 2.18 is the side view of zinc toluic acid-based photoresists, and their top view is on the bottom. From Figure 2.18b, c, e and f, it was found that both ZnO-*m*TA-NP and ZnO-*p*TA-NP have relatively symmetric structures. However, ZnO-*o*TA-NP possesses a twisted structure due to steric effects (Figure 2.18 a, d). It is believed that this asymmetrical structure causes a difference in photolithographic performance compared to the other two symmetrically-structured materials. From a roughly calculation, the energy of ZnO-*o*TA-NP is 120 kJ higher than the other two, indicating that this photoresist is far more unstable. Therefore, ZnO-*o*TA-NP might be more likely to decompose after exposure, causing a higher sensitivity in the photolithographic evaluation.

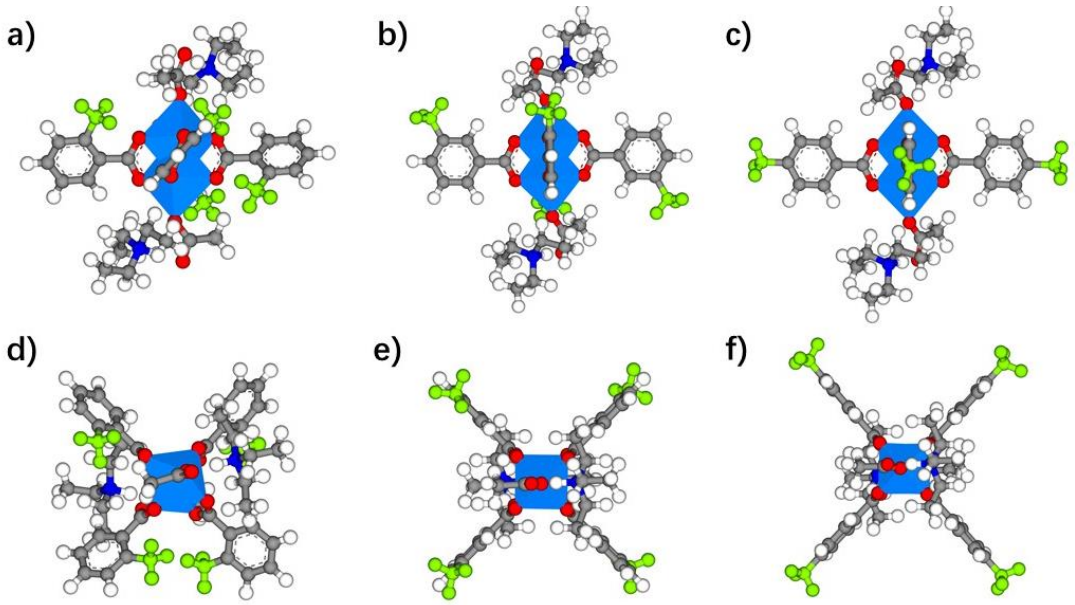

Figure 2.18. Computational structure simulation. The light blue regular octahedrons in the center indicates the Zn core, around which acid and base ligands are located. The white balls are hydrogen atoms, green ones are carbon atoms, navy blue ones are nitrogen atoms and red ones are oxygen atoms. a) Side view of ZnO-*o*TA-NP; b) Side view of ZnO-*m*TA-NP; c) Side view of ZnO-*p*TA-NP; d)Top view of ZnO-*o*TA-NP; e) Top view of ZnO-*m*TA-NP; f) Top view of ZnO-*p*TA-NP.

2.4 Conclusion

From the studies of zinc-based nanoparticles used as EUV photoresists, the modification of ZnO core through ligation with carboxylic acid and base ligands can decrease nanoparticle size and improve film quality in photolithography and wafer nanofabrication. For the three zinc-based photoresists with toluic acid as ligands (ZnO-*o*TA-NP, ZnO-*m*TA-NP and ZnO-*p*TA-NP), they possess small particle sizes, excellent solubility in spin-coating solvents, excellent film-forming capability and pattern formation under UV and E-beam radiation. Based on the previous work,

patterning performance of ZnO-*m*TA-NP without PAG was investigated. Good-quality patterns can be obtained even without PAG, suggesting ZnO-*m*TA-NP is a light-sensitive nanoparticle. Though similar in structure, these three zinc-based photoresists perform differently in sensitivity and resolution. From E-beam evaluation, ZnO-*p*TA-NP displays the best resolution (20 nm patterns at a dosage of 100 μC cm^{-2}). In terms of sensitivity, ZnO-*o*TA-NP has the best performance in the QCM evaluation. In addition, ZnO-*o*TA-NP shows a higher sensitivity (~ 20 mJ cm^{-2}) than ZnO-*m*TA-NP (124 mJ cm^{-2}). Further EUV evaluation will be carried out in the future.

REFERENCES

1. Henke, B.L., Gullikson, E.M. and Davis, J.C., X-ray interactions: photoabsorption, scattering, transmission and reflection E= 50-30,000 eV, Z= 1-92. *At. Data Nucl. Data Tables*, **1993**, *54*: 181-342.
2. Xu, H., Sakai, K., Kasahara, K., Kosma, V., Yang, K., Herbol, H.C., Odent, J., Clancy, P., Giannelis, E.P. and Ober, C.K., Metal-organic framework-inspired metal-containing clusters for high resolution patterning. *Chem. Mater.*, **2018**, *30*(12): 4124-4133.
3. Bae, W.J., Trikeriotis, M., Rodriguez, R., Zettel, M.F., Piscani, E., Ober, C.K., Giannelis, E.P. and Zimmerman, P., High-index nanocomposite photoresist for 193-nm lithography. *Proc. SPIE*, **2009**, *7273*: 727326.
4. Chakrabarty, S., Sarma, C., Li, L., Giannelis, E.P. and Ober, C.K., Increasing sensitivity of oxide nanoparticle photoresists. *Proc. SPIE*, **2014**, *9048*: 90481C.
5. Yu, M., Xu, H., Kosma, V., Odent, J., Kasahara, K., Giannelis, E. and Ober, C., Positive Tone Nanoparticle Photoresists: New Insight on the Patterning Mechanism. *J. Photopolym. Sci. Tec*. **2016**, *29*(3): 509-512.
6. Kasahara, K., Xu, H., Kosma, V., Odent, J., Giannelis, E.P. and Ober, C.K., Nanoparticle photoresist studies for EUV lithography. *Proc. SPIE*, **2017**, *10143*: 1014308.
7. Xu, H., Kosma, V., Giannelis, E.P. and Ober, C.K., In pursuit of Moore's Law: polymer chemistry in action. *Polymer J.*, **2018**, *50*(1): 45.

8. Kasahara, K., Xu, H., Kosma, V., Odent, J., Giannelis, E.P. and Ober, C.K., Recent Progress in EUV Metal Oxide Photoresists. *J. Photopolym. Sci. Tec*., **2017**, *30*(1): 93-97.
9. Xu, H., Yang, K., Sakai, K., Kosma, V., Kasahara, K., Giannelis, E.P. and Ober, C.K., EUV metal oxide hybrid photoresists: ultra-small structures for high-resolution patterning. *Proc. SPIE*, **2018**, *10583*: 105831P.
10. Cook, T.R., Zheng, Y.R. and Stang, P.J., Metal–organic frameworks and self-assembled supramolecular coordination complexes: comparing and contrasting the design, synthesis, and functionality of metal–organic materials. *Chemical reviews*, **2012**, *113*(1): 734-777.
11. Trikeriotis, M., Krysaki, M., Chung, Y.S., Ouyang, C., Cardineau, B., Brainard, R., Ober, C.K., Giannelis, E.P. and Cho, K., Nanoparticle photoresists from HfO2 and ZrO2 for EUV patterning. *J. Photopolym. Sci. Tec.*, **2012**, *25*(5): 583-586.
12. Ouyang, C.Y., Chung, Y.S., Li, L., Neisser, M., Cho, K., Giannelis, E.P. and Ober, C.K., Non-aqueous negative-tone development of inorganic metal oxide nanoparticle photoresists for next generation lithography. *Proc. SPIE,* **2013**, *8682*: 86820R.
13. Jiang, J., Chakrabarty, S., Yu, M. and Ober, C.K., Metal oxide nanoparticle photoresists for EUV patterning. *J. Photopolym. Sci. Tec.*, **2014**, *27*(5): 663-666.

CHAPTER 3

ZINC-BASED PHOTORESIST WITH METHACRYLIC ACID LIGAND

3.1 Background and Motivation

Among metal oxide-based photoresists developed by our group, the methacrylic acid (MAA) modified zirconium oxide photoresist (ZrO_2-MAA-NP) gives the best over-all-performance[1]. Another type of Zn-based photoresist was prepared through the approach via complexation between methacrylic acid and zinc, which is described in Chapter 2. With methacrylic acid as the ligand, the zinc oxide-methacrylic acid photoresist (ZnO-MAA-NP) has a ZnO core and a methacrylic acid shell (Figure 3.1). The ZnO-MAA-NP photoresist possesses small particle size, good solubility in spin-coating solvents, good film-forming capability and pattern formation as the previously introduced toluic acid-based photoresist. Specifically, this methacrylic acid-based photoresist shows better resolution patterns when photo-radical generator (PRG) is applied as photo sensitive initiator.

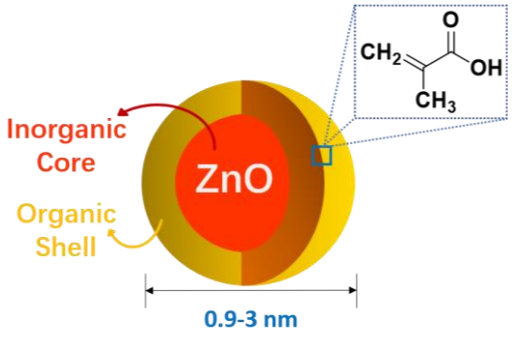

Figure 3.1. Schematic representation of ZnO-MAA-NP.

3.2 Experimental Section

Details of chemicals, solvents and silicon wafers used for this experiment have been listed in Chapter 2. Synthesis procedure of ZnO-MAA-NP is given below. Characterization methods have also been introduced in Chapter 2.

ZnO-MAA-NP: In a 100 mL round-bottomed flask, zinc methacrylate (4.7 g, 0.02 mol), methacrylic acid (1.75 g, 0.02 mol) and triethylamine (2.05 g, 0.02 mol) were mixed, followed by addition of 50mL ethyl acetate. The reaction mixture was stirred at room temperature for 8 days. The solvent was removed with a rotary evaporator and further dried in vacuum for 6 hours. The final product, ZnO-MAA-NP, was obtained as a milky suspension.

3.3 Results and Discussion

3.3.1 DLS measurement

Dynamic light scattering (DLS) measurements (Figure 3.2) show that the ZnO-MAA-NP nanoparticles are monodisperse, with a particle size of 0.9 nm to 3 nm, which are smaller than ZrO_2 and HfO_2 based nanoparticles (3 ~ 4 nm)[2]. The small particle size is another reason for the good film forming ability of the nanoparticles. Ultra-small size nanoparticles enhance the possibility to achieve high resolution in lithography.

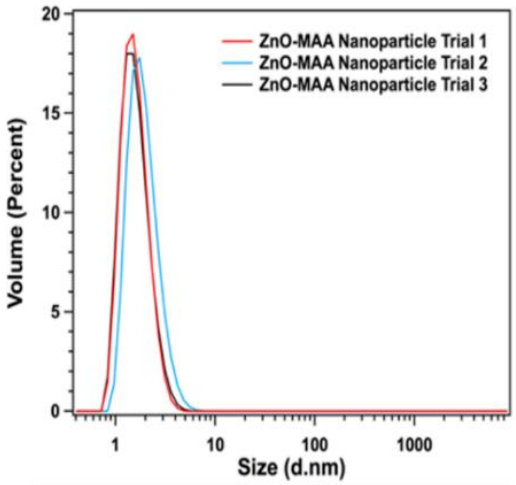

Figure 3.2. Dynamic light scattering spectra of ZnO-MAA Nanoparticle.

3.3.2 Solubility and film forming

As toluic acid-based photoresists, ZnO-MAA-NP also demonstrates very good solubility in commonly used spin-coating solvents, such as propylene glycol monomethyl ether acetate (PGMEA). As shown in Figure 3.3a, clear and transparent solutions can be obtained even if the ZnO-MAA-NP concentration is increased to 20 wt%. Good solubility in spin-coating solvents endows the ZnO-MAA-NP nanoparticles with good film-forming ability. As shown in Figure 3.3b, excellent ZnO-MAA-NP nanoparticle films can be fabricated by simply spin-coating nanoparticles in PGMEA solution onto a silicon wafer just as the ZnO-*m*TA-NP film discussed in Chapter 2. Uniform films can be obtained after spin-coating and no obvious particle aggregation was observed.

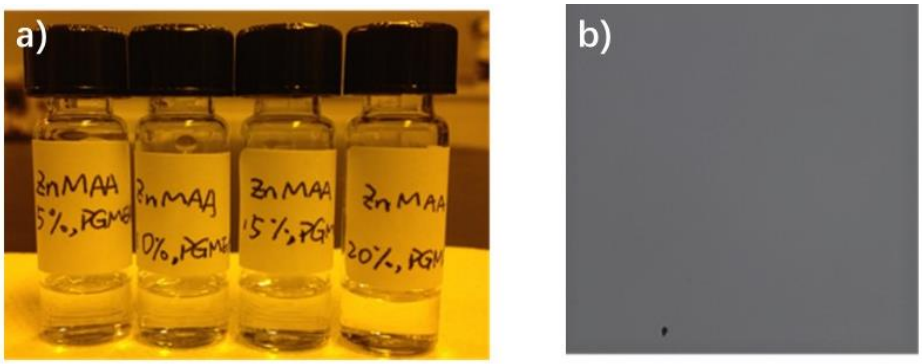

Figure 3.3. a) Solubility test of ZnO-MAA-NP from 5% to 20%, solution: PGMEA and b) Optical image of ZnO-MAA-NP film (the black dot is to ensure the microscope is well-focused but such defects are quite rare in spin-coating film).

3.3.3 Mid-UV evaluation

In this study, photo-acid generator (PAG) was used following the convention of photoresist solution preparation. However, low-quality patterns were obtained after mid-UV exposure (Figure 3.4a). Unlike toluic acid, methacrylic acid has a carbon-carbon double bond, which is more susceptible to photo-radical generators (PRGs) rather than to PAG. In this way, a PRG was introduced into the resist solution and the imaging result shown in Figure 3.4b. Since the pattern quality is significantly improved with PRG initiation, PRG was adopted as a better option for ZnO-MAA-NP lithography.

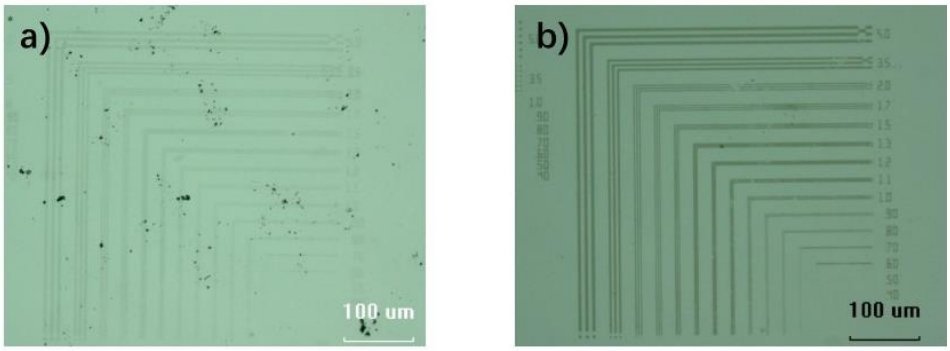

Figure 3.4. Optical microscope images of ZnO-MAA-NP exposed at a dosage of 150 mJ cm^{-2} and developed in DHN for 40s: a) initiated by PAG; b) initiated by PRG.

3.3.4 Pattern optimization

Previous optimization of ZnO-MAA-NP mainly focused on the synthesis methods and the PRG concentration. Here we started from the optimization of synthesis conditions, since both reaction temperature and time can have great influence on the particle formation, which can determine the final resist performance. Two batches of ZnO-MAA-NP were synthesized using different conditions, one stirred at room temperature for 8 days and the other at 65℃ for 15 hours. The materials were then purified and tested under mid-UV exposure, and the resultant optical microscope images are shown in Figure 3.5. The materials synthesized at room temperature (Figure 3.5a) have sharper and more well-defined line edges compared to their counterpart prepared at 65℃, indicating that lower temperature and longer reaction time have a beneficial effect on the particle synthesis. (Figure 3.5b). Here, the materials synthesized at room temperature were used for the subsequent processing.

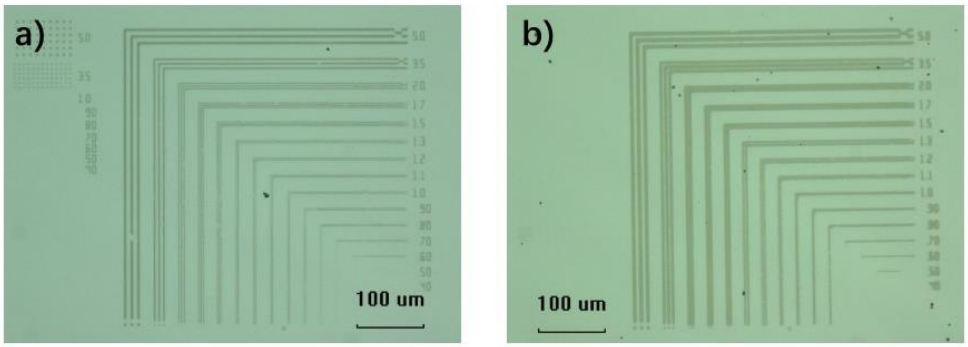

Figure 3.5. Optical microscope images of ZnO-MAA-NP exposed at 150 mJ cm^{-2}: a) synthesized at room temperature for 8 days, developed in DHN for 20s; b) synthesized at 65℃ for 15 hours, developed in 1,3,5-trimethylbenzene for 20s.

The patterning performance of 2, 5 and 10 wt% PRG concentrations were also investigated and the results are indicated below in Table 3.2 and Figure 3.6. It was found that the solubility strength required to achieve the optimal pattern decreases as the concentration of PRG increases. Samples under the best development conditions were evaluated by optical microscope and the images are presented in Figure 3.6. Figure 3.6 displays the best patterns achieved from each PRG concentration, with the optimal concentration found to be 5 wt%, as pattern lines are better in shape and resolution than the other two samples.

Table 3.2. Developing conditions for different concentrations of PRG added to ZnO-MAA-NP synthesized at room temperature for 8 days. A cross mark corresponds to an unfavorable pattern developed or no pattern obtained. A check mark indicates a satisfactory pattern.

	Decahydronaphthalene (DHN)				1,3,5-trimethylbenzene (1,3,5-TMB)					
wt % PRG	10s	20s	30s	40s	2s	5s	10s	30s	60s	70s

2%	×	×	×	×	×	×	×	×	√	×
5%	×	×	×	√	√	√	×	×	×	×
10%	×	√	√	√	√	√	×	×	×	×

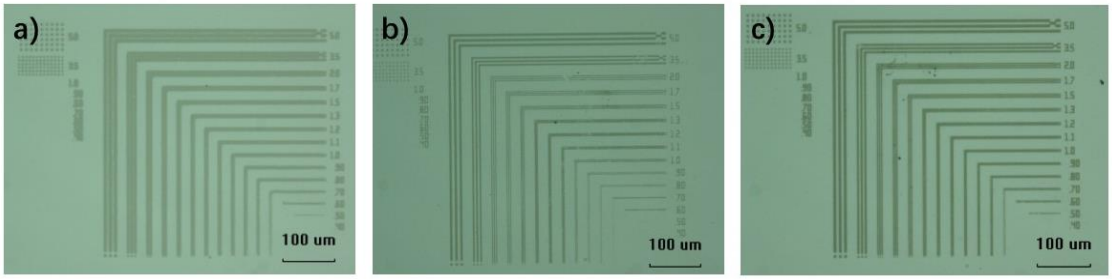

Figure 3.6. Optical microscope images of ZnO-MAA-NP synthesized at room temperature for 8 days and exposed at 150 mJ cm^{-2}: a) 2 wt% PRG in 1,3,5-TMB for 60s; b) 5 wt% PRG in DHN for 40s; c) 10 wt% PRG in DHN for 40s

3.3.5 QCM curves

In order to further explore ZnO-MAA-NP's performance with two different initiators, a QCM test was carried out. It was found that ZnO-MAA-NP shows totally different dissolution performance compared with toluic acid-based photoresists. Figure 3.7 are quartz crystal microbalance (QCM) curves of ZnO-MAA-NP thin film before and after DUV exposure with different initiators, indicating their distinct dissolution characteristics. Before exposure, the time difference when the curve becomes relatively flat is close to 2 seconds. However, there is a noticeable dissolution rate change after exposure, indicating that the hybrid photoresist film was more difficult to dissolve after exposure. Results in Figure 3.7a support the previous ligand exchange mechanism explained in the above toluic acid-based photoresists case. By contrast

between Figure 3.7a and b, the dissolution difference is more apparent with PRG compared to PAG.

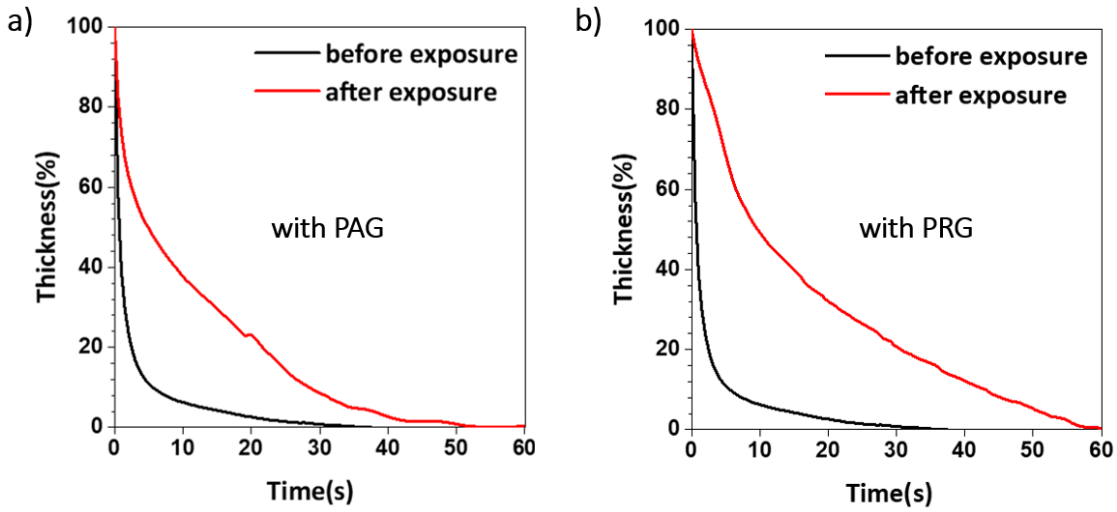

Figure 3.7. QCM curves of ZnO-MAA-MP thin film before and after 150 mJ cm^{-2} DUV exposure and developed in DHN: a) initiated by PAG; b) initiated by PRG.

3.3.6 DUV evaluation

After mid-UV and QCM characterization, DUV evaluation was carried out using 248 nm ASML DUV stepper. With PAG added, the unexposed areas are clean under SEM image conditions, but top-loss and side-loss occur and cause twisted patterns (Figure 3.8a). In contrast, the PRG gives much better patterning performance at 500 nm line-and-space 1:1 pattern, as shown in Figure 3.8b. The exposure energies used in Figure 3.8a and b were the same, 150 mJ cm^{-2}. However, a significant difference in patterning efficiency can be observed. PRG demonstrated higher efficiency than PAG in terms of triggering dissolving behavior change. This point is consistent with the

previously discussed QCM measurement that the dissolution rate of PRG containing film is slower than that of PAG after exposure.

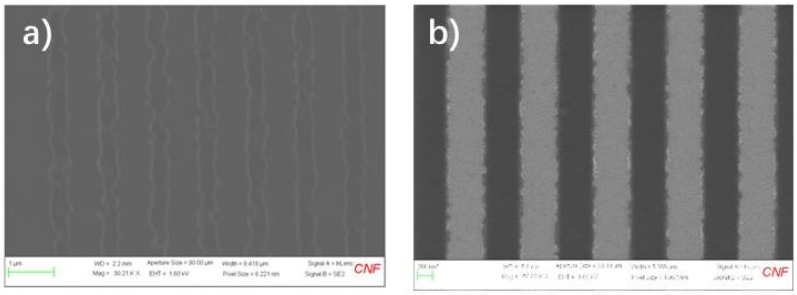

Figure 3.8. Scanning electron microscope images of ZnO-MAA-NP, developer: DHN, developing time: 40s, exposure dose: 150 mJ cm^{-2}: (a) initiated by PAG; (b) initiated by PRG.

3.3.7 Patterning mechanism exploration

PRG triggered patterning has also been observed in the previous reported ZrO_2-based photoresists[3]. However, the photo-acid generator proved to be a very efficient initiator in these systems[2-3, 6-10]. Considering the vinyl-group modified nanoparticle surface, a plausible explanation for the high sensitivity of PRG is that PRG may trigger the olefin polymerization of the methacrylic acid modified ZnO nanoparticles. Therefore, solubility changed after exposure due to ZnO-MAA-NP nanoparticle polymerization or aggregation.

In order to explore the pattering mechanism of ZnO-MAA-NP, X-ray photoelectron spectroscopy (XPS) evaluation was performed. Four sets of samples were prepared to compare the role of PAG and PRG. Sample A includes ZnO-MAA-NP with PAG before 248 nm DUV exposure. Sample B includes ZnO-MAA-NP with PAG after 248

nm DUV exposure. Sample C includes ZnO-MAA-NP with PRG before 248 nm DUV exposure. And sample D includes ZnO-MAA-NP with PRG after 248 nm DUV exposure. Unfortunately, no distinct difference was found among the four groups of results shown in Figure 3.9. A possible reason for this failure is that all samples exposed by the white light during XPS testing, and thus no difference can be found between the unexposed and exposed samples. Detailed surveys of carbon, phosphor and zinc orbits will be shown in supporting information. Exploring the patterning mechanism of ZnO-MAA-NP will be one of the future goals.

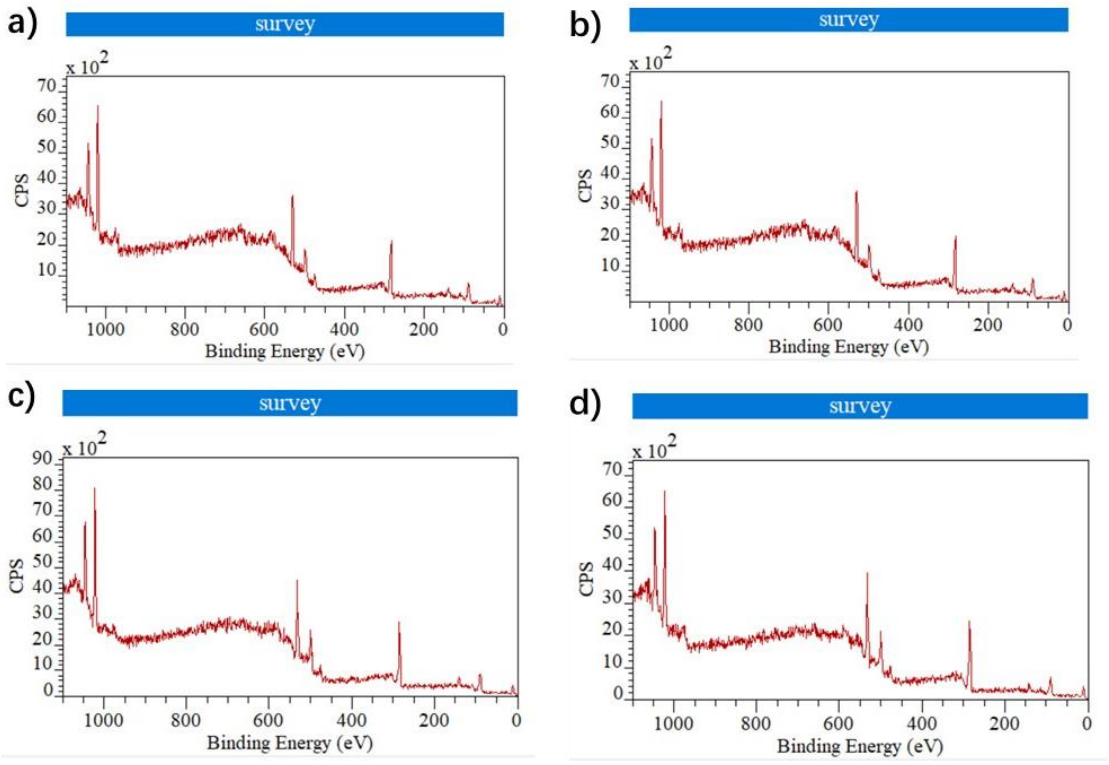

Figure 3.9. X-ray photoelectron spectroscopy of ZnO-MAA-NP: (a) initiated by PAG before exposure; (b) initiated by PAG after exposure; (c) initiated by PRG before exposure; (d) initiated by PRG after exposure.

3.3.8 ZnO-MAA-NP used for 3D printing

In a collaboration with Dungyi Wu in our group, ZnO-MAA-NP was utilized as an ink for 3D printing. It was found that 3D structures can be fabricated with ZnO-MAA-NP at room temperature. Figure 3.10 shows structures with a resolution approaching 50 μm, which is four times higher than current techniques with a height variation of only several nanometers. Printing speed of ZnO of up to 3.3 μm/s was reached as the intensity reached 3.0 mW/cm^2 under a nitrogen atmosphere. These promising results offer a prospective way to manufacture 3D printed ZnO macrostructures for future development of optoelectronic and semiconductor devices.

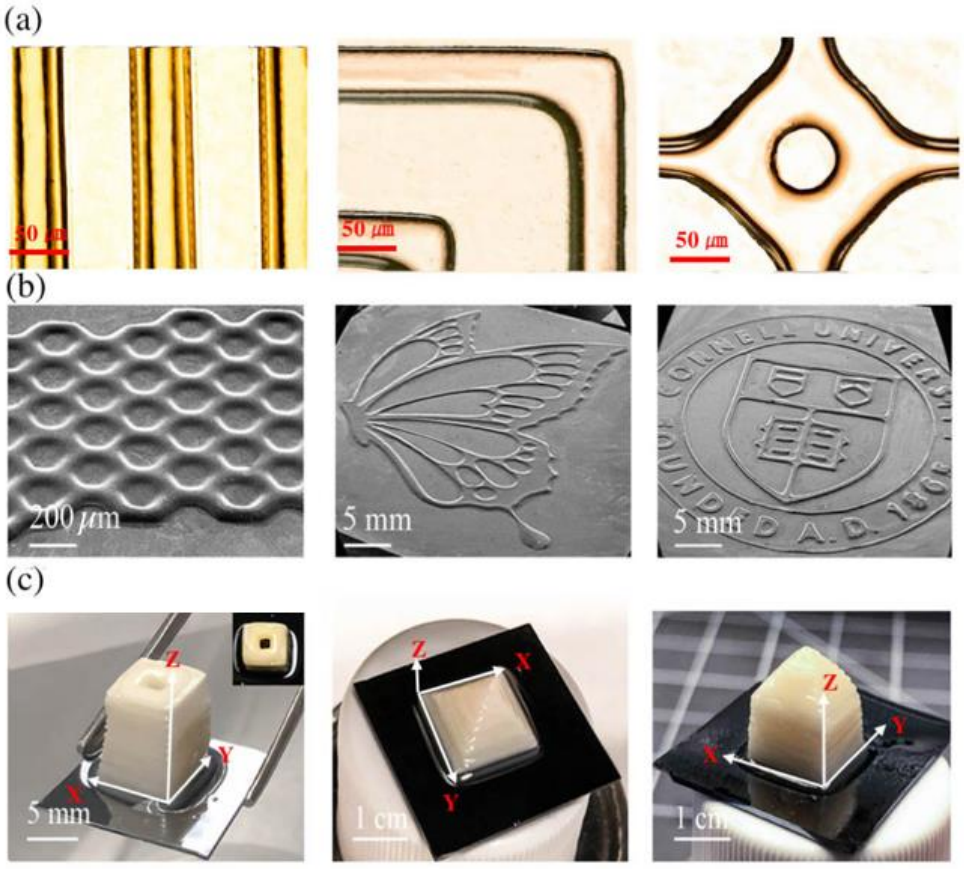

Figure 3.10. 3D printing of structures: a) Parallel lines, bent corners and a square array with voids; b) Honeycomb, butterfly and Cornell logo microstructures printed by the digital light processing technique; c) Hollow cuboid, pyramidal and townhouse 3D structures manufactured by this technique.

3.4 Conclusion

Similar to the toluic acid-based photoresists, ZnO-MAA-NP possesses small particles size, good solubility in spin-coating solvents, good film-forming ability and moderate patterning performance under deep-UV radiation. Different from the PAG triggered patterning mechanism of the reported metal oxide-based nanoparticles, ZnO-MAA-NP demonstrates higher sensitivity and better resolution when a photo-radical generator is used as a photo-initiator. Considering the high EUV photo-absorption of zinc metal together with photoelectron triggered radical mechanism under EUV radiation, this preliminary work indicates that such zinc-based nanoparticles could be promising candidates for EUV lithography and 3D printing. They act as building blocks that are used to construct mesoscale 3D structures. Several promising 3D printing results have been achieved, such as 50 μm resolution, 3.3 μm/s printing speed and intensity of 3.0 mW/cm^2 under a nitrogen atmosphere.

REFERENCES

1. Trikeriotis, M., Krysaki, M., Chung, Y.S., Ouyang, C., Cardineau, B., Brainard, R., Ober, C.K., Giannelis, E.P. and Cho, K., Nanoparticle photoresists from HfO2 and ZrO2 for EUV patterning. *J. Photopolym. Sci. Tec.*, **2012**, *25*(5): 583-586.
2. Li, L., Chakrabarty, S., Spyrou, K., Ober, C.K. and Giannelis, E.P., Studying the mechanism of hybrid nanoparticle photoresists: effect of particle size on photopatterning. *Chem. Mater.*, **2015**, *27*(14): 5027-5031.
3. Yu, M., Xu, H., Kosma, V., Odent, J., Kasahara, K., Giannelis, E. and Ober, C., Positive Tone Nanoparticle Photoresists: New Insight on the Patterning Mechanism. *J. Photopolym. Sci. Tec*., **2016**, *29*(3): 509-512.
4. Xu, H., Yang, K., Sakai, K., Kosma, V., Kasahara, K., Giannelis, E.P. and Ober, C.K., EUV metal oxide hybrid photoresists: ultra-small structures for high-resolution patterning. *Proc. SPIE*, **2018**, *10583*: 105831P.
5. Xu, H., Sakai, K., Kasahara, K., Kosma, V., Yang, K., Herbol, H.C., Odent, J., Clancy, P., Giannelis, E.P. and Ober, C.K., Metal-organic framework-inspired metal-containing clusters for high resolution patterning. *Chem. Mater.*, **2018**, *30*(12): 4124-4133.
6. Trikeriotis, M., Bae, W.J., Schwartz, E., Krysak, M., Lafferty, N., Xie, P., Smith, B., Zimmerman, P.A., Ober, C.K. and Giannelis, E.P., Development of an inorganic photoresist for DUV, EUV, and electron beam imaging. *Proc. SPIE*, **2010**, *7639*: 76390E.
7. Bae, W.J., Trikeriotis, M., Sha, J., Schwartz, E.L., Rodriguez, R., Zimmerman, P., Giannelis, E.P. and Ober, C.K., High refractive index and high transparency HfO_2

nanocomposites for next generation lithography. *J. Mater. Chem. A.*, **2010**, *20*(25): 5186-5189.

8. Krysak, M., Trikeriotis, M., Schwartz, E., Lafferty, N., Xie, P., Smith, B., Zimmerman, P., Montgomery, W., Giannelis, E. and Ober, C.K., Development of an inorganic nanoparticle photoresist for EUV, e-beam, and 193nm lithography. *Proc. SPIE*, **2011**, *7972*: 79721C.
9. Trikeriotis, M., Krysak, M., Chung, Y.S., Ouyang, C., Cardineau, B., Brainard, R., Ober, C.K., Giannelis, E.P. and Cho, K., A new inorganic EUV resist with high-etch resistance. *Proc. SPIE*, **2012**, *8322*: 83220U.
10. Chakrabarty, S., Sarma, C., Li, L., Giannelis, E.P. and Ober, C.K., Increasing sensitivity of oxide nanoparticle photoresists. *Proc. SPIE*, **2014**, *9048*: 90481C.

CHAPTER 4

COMPLEMENTARY WORK AND FUTURE GOALS

4.1 Zinc-based Photoresist with Methoxybenzoic Acid Ligands

4.1.1 Experimental section

Details of chemicals, solvents and silicon wafers used for this experiment have been listed in Chapter 2. Synthesis procedure of ZnO-MAA-NP is given below. Characterization methods have also been introduced in Chapter 2.

ZnO-2MA-NP: In a 100 mL round-bottomed flask, zinc acetate dihydrate (4.38 g, 0.02 mol), 2-methoxybenzoic acid (6.09 g, 0.04 mol) and triethylamine (3.06 g, 0.03 mol) were mixed, followed by addition of 50 mL ethyl acetate. The reaction mixture was stirred at 65^{o}C for 15 hours. The solvent was removed with a rotary evaporator at 65^{o}C and the residue was further dried under vacuum for 6 hours. The final product, ZnO-2MA-NP, was obtained as a transparent gel.

ZnO-3MA-NP and **ZnO-4MA-NP** were synthesized with the similar method as ZnO-2MA-NP, 3-methoxybenzoic acid and 4-methoxybenzoic acid were used as exactly the same molar amount as 2-methoxybenzoic acid.

4.1.2 Results and discussion

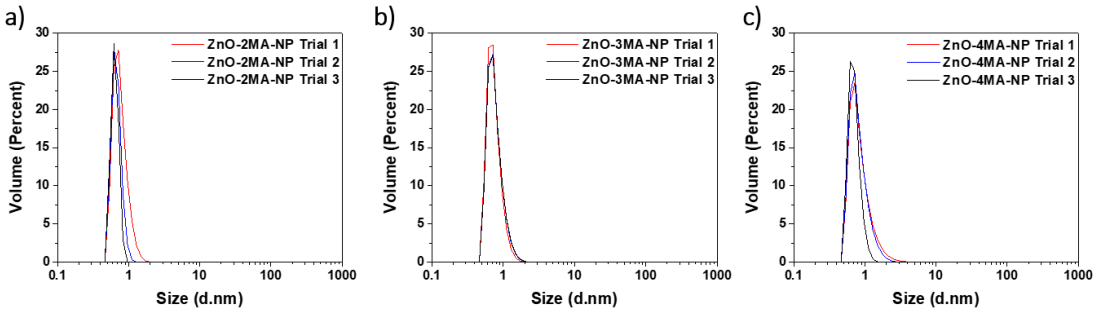

Figure 4.1. Dynamic light scattering spectra of methoxybenzoic acid-based nanoparticles: a) ZnO-2MA-NP; b) ZnO-3MA -NP; c) ZnO-4MA -NP.

As can be seen from results of DLS measurement (Figure 4.1), with the average size around 0.8 nm, methoxybenzoic acid-based nanoparticles possess smaller size and narrower size distribution than toluic acid-based nanoparticles. Mid-UV and DUV evaluation were conducted as the method introduced in the previous chapters. Here shows the best developing parameters (Table 4.1) and SEM images (Figure 4.2) up to now. However, unfavorable patterns were obtained after DUV exposure (Figure 4.2). Compared to toluic acid-based nanoparticles, these three nanoparticles show poorer resolution. In order to analyze the pattern height difference, we took the sample (ZnO-4MA-NP) with the best lithographic performance after DUV exposure to analyze with AFM.

Table 4.1. Best photolithographic parameters of ZnO-2MA-NP, ZnO-3MA-NP and ZnO-4MA-NP.

Sample	Photo Active Compound	Soft Bake Temperature	Developer	Developing Time (s)

		(°C)		
ZnO-2MA-NP	PAG	100	o-xylene	20
ZnO-3MA-NP	PAG	90	1,3,5-TMB	10
ZnO-4MA-NP	PAG	60	DHN	15

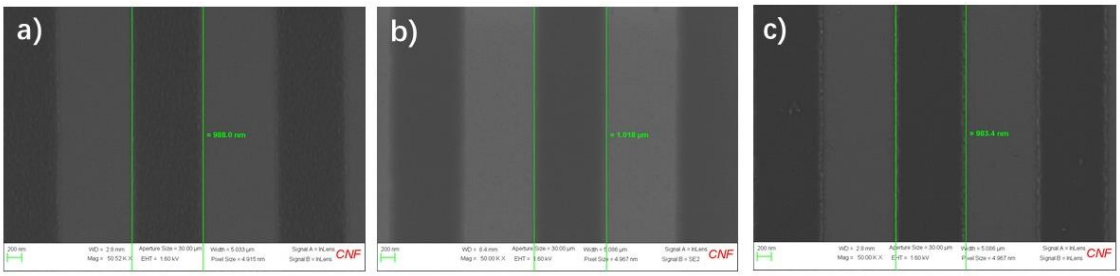

Figure 4.2. SEM images of zinc methoxybenzoic acid based photoresists with their best photolithographic parameters shown in Table 4.1 after 150 mJ cm^{-2} exposure: a) ZnO-2MA-NP; b) ZnO-3MA-NP; c) ZnO-4MA-NP.

Shown in Figure 4.3, good height profile can be acquired with AFM when the pattern width is 1000 nm or 500 nm. The exposed portion of the nanoparticles successfully resisted the rinsing of the developer, retaining a thickness of about 30 nm. However, most of the photoresist was washed away, with the thickest part merely 6 nm. These results indicate that further optimization based on synthesis or lithography process is needed for the methoxybenzoic acid-based system.

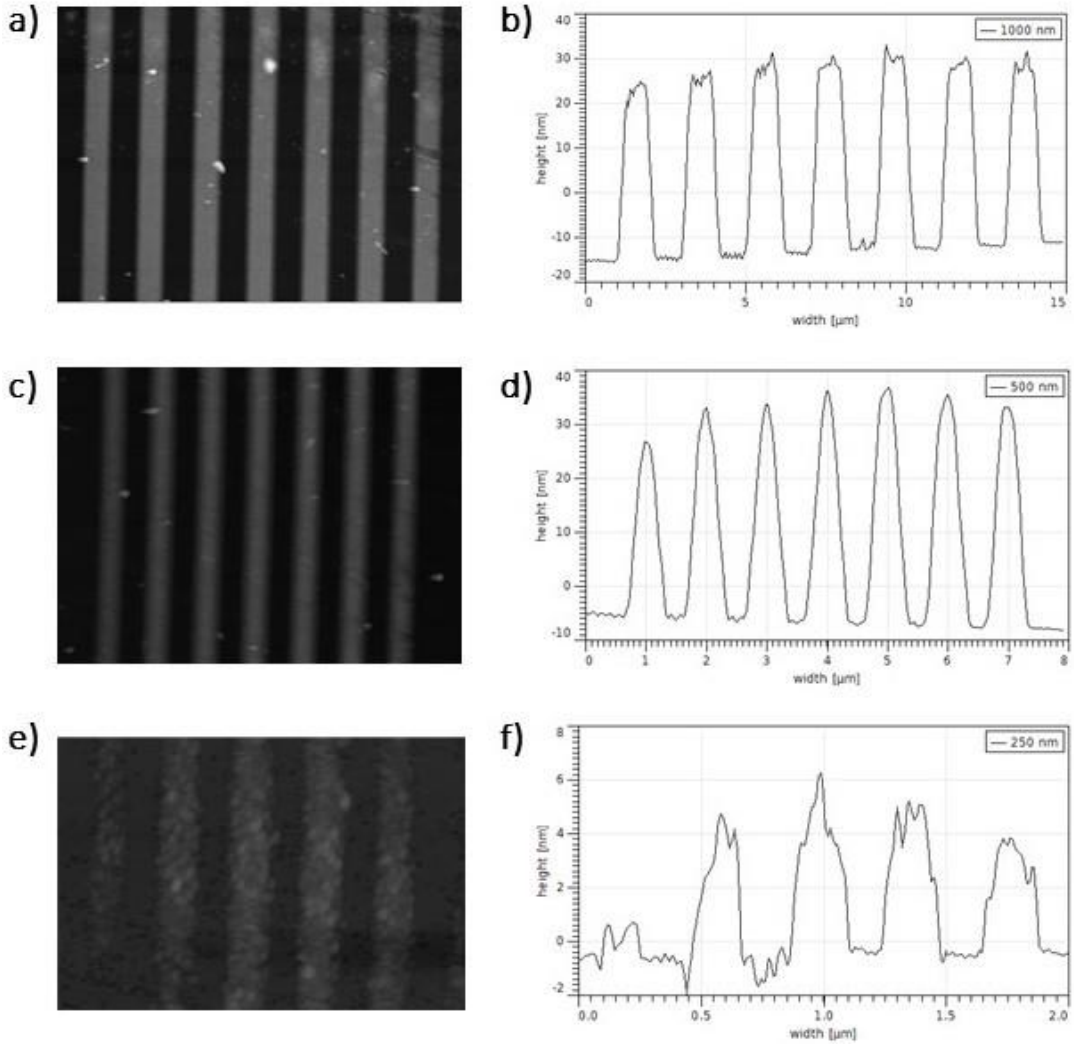

Figure 4.3. AFM analyze of ZnO-4MA-NP with their best photolithographic parameters shown in Table 4.1 after 150 mJ cm^{-2} exposure: a) 1000 nm pattern image; b) 1000 nm pattern height profile; c) 500 nm pattern image; d) 500 nm pattern height profile; e) 250 nm pattern image; f) 250 nm pattern height profile.

4.2 Effect of Bottom Anti-Reflective Coatings (BARC)

4.2.1 Introduction of BARC

As the exposure wavelength of lithography technology continues to decrease, the resolution of the pattern is significantly improved. However, it also brings some negative effects due to the optical reflection effect of the surface of the substrate (such as the silicon wafer). The reflected light interferes with the incident light, forming a standing wave effect inside the photoresist, resulting in uncontrollable pattern dimensions. The wave-like pattern on the sidewall greatly increases the difficulty of controlling the etching accuracy[1]. In addition, studies have found that the smaller the exposure wavelength, the greater the influence of the standing wave effect, the swing effect and the notching effect on the uniformity of the critical dimensions of the pattern, and thus the more serious influence on the sharpness and resolution of the pattern.[2]

In order to overcome the above problems, researchers in the 1990s found that Anti-Reflective Coatings (ARC) can effectively alleviate the standing wave effect and improve the uniformity of key dimensions.[3-6] According to the fabrication process, ARC can be roughly divided into two categories: Top Anti-Reflective Coatings (TARC) and Bottom Anti-Reflective Coatings (BARC). However, compared with TARC, BARC have more obvious effects on reducing the swing effect and the recess effect.[7] Therefore, developing BARC materials to improve the critical size uniformity in the lithography process has become a mainstream method commonly used in the industry.

4.2.2 Zinc-based photoresist with BARC

Before the performance of zinc-based photoresist with BARC materials was evaluated, the developing conditions of ZnO-*o*TA-NP was first confirmed. As the photolithographic process discussed above, the best parameters of ZnO-*o*TA-NP are shown in Table 4.2 and the corresponding SEM images are shown in Figure 4.4.

Table 4.2. Best photolithographic parameters of ZnO-*o*TA-NP.

Sample	Photo Active Compound	Soft Bake Temperature (°C)	Developer	Developing Time (s)
ZnO-*o*TA-NP	PAG	100	DHN	10

Figure 4.4. SEM images of ZnO-*o*TA-NP with the best photolithographic parameters shown in Table 4.2. after 150 mJ cm^{-2} exposure: a) patterns ranging from 500 nm to 750 nm; b) 500 nm patterns; c) 300 nm patterns.

With the best photolithographic parameters above, ZnO-*o*TA-NP in combination with three different BARC materials was then evaluated. An experimental process schematic is shown in Figure 4.5. BARC was spin-coated on the wafer as the first layer and 205 °C baking was needed for triggering a chemical reaction of BARC, such as polymerization. After BARC application, ZnO-*o*TA-NP was then spin-coated as the

second layer and soft baked at 65 °C. DUV exposure and development was conducted at the process introduced in Chapter 2. SEM images before and after the application of BARC are shown in Figure 4.6. The pattern quality is greatly improved with BARC application.

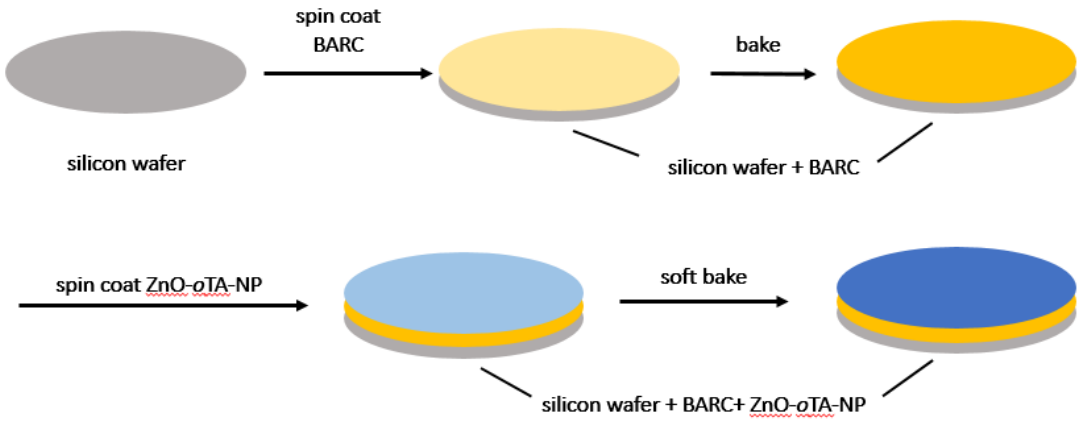

Figure 4.5. Schematic diagram of BARC experiment process.

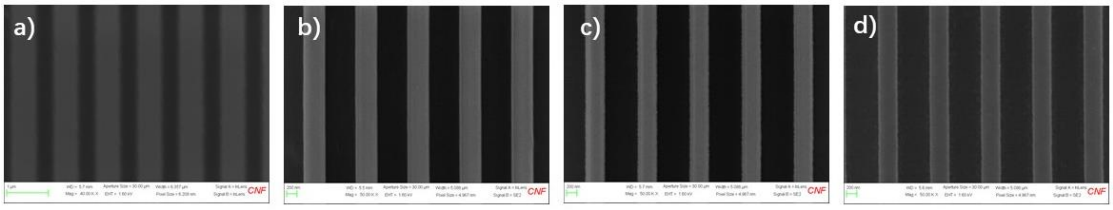

Figure 4.6. Scanning electron microscope images of ZnO-*o*TA-NP, developer: DHN, developing time: 10s, exposure dose: 150 mJ cm^{-2}: (a) without BARC; (b) with BARC-1; (c) with BARC-2; (c) with BARC-3.

4.3 Future Goals

In this work, seven zinc-based nanoparticles used as EUV photoresists have been investigated. Mid-UV, DUV, E-beam and EUV evaluation were conducted to explore their photolithographic performance. For the three zinc-based photoresists with toluic

acid as ligands (ZnO-*o*TA-NP, ZnO-*m*TA-NP and ZnO-*p*TA-NP), high resolution patterns were obtained after DUV and E-beam exposure. If possible, we hope to be able to proceed with further EUV evaluation in the future. For the zinc-based photoresist with methacrylic acid ligands (ZnO-MAA-NP), better resolution patterns can be obtained with the PRG used as an initiator instead of PAG. However, pattern quality is not promising for EUV evaluation. Additional optimization will be needed and previous results of ZnO-MAA-NP optimization have been presented in the previous chapter. Besides toluic acid and methacrylic acid, zinc-based photoresists with methoxybenzoic acid were also synthesized (ZnO-2MA-NP, ZnO-3MA-NP and ZnO-4MA-NP). Synthesis and characterization have been introduced in the first section of this Chapter, but further optimization is also needed for the same reason as ZnO-MAA-NP. For the methoxybenzoic acid system, DLS measurement, developing parameters and SEM images after DUV exposure have also been presented in this chapter. Recently, it was found that BARC has positive effects on the resolution of the zinc-based photoresists. Therefore, in the last section of this chapter, SEM images after applying BARC under the zinc-based photoresist were shown. Further research based on etching assessment is ongoing.

REFERENCES

1. Jung, J.C., Kong, K.K. and Kim, S.K., Light absorbent agent polymer for organic anti-reflective coating and preparation method and organic anti-reflective coating composition comprising the same. *U.S. Patent*, **2006**, *7,033,729*.
2. Hwang, S.H., Lee, K.K. and Jung, J.C., A novel organic bottom anti-reflective coating material for 193 nm excimer laser lithography. *Polymer*, **2000**, *41*(17): 6691-6694.
3. Raut, H.K., Ganesh, V.A., Nair, A.S. and Ramakrishna, S., Anti-reflective coatings: A critical, in-depth review. *Energ. Environ. Sci.*, **2011**, *4*(10): 3779-3804.
4. Houlihan, F.M., Miyazaki, S., Neisser, M.O., Dioses, A.D. and Oberlander, J.E., Bottom antireflective coating compositions. *U.S. Patent*, **2012**, *8,088,548*.
5. Bourke, L. and Blaikie, R.J., Evanescent-coupled antireflection coatings for hyper-numerical aperture immersion lithography. *J. Vac. Sci. Technol. B*, **2014**, *32*(6): 06FE03.
6. Cho, B., Hahm, M.G., Choi, M., Yoon, J., Kim, A.R., Lee, Y.J., Park, S.G., Kwon, J.D., Kim, C.S., Song, M. and Jeong, Y., Charge-transfer-based gas sensing using atomic-layer MoS 2. *Sci. Rep.*, **2015**, *5*: 8052.
7. Vyklicky, L., Huang, W.S., Popova, I., Varanasi, P.R., Cameron, J., Amara, J., Sung, J.W., Valeri, D., Prokopowicz, G., Ware, A. and O'Connell, K., A New Breed of Wet-Developable BARC Materials. *J. Photopolym. Sci. Tec.*, **2009**, *22*(1): 17-24.

SUPPORTING INFORMATION

Contents:

S18 ^{1}H NMR spectra of ZnO-MAA-NP

S19 XPS Carbon 1s orbit survey of ZnO-MAA-NP.

S20 XPS Phosphors 2p orbit of ZnO-MAA-NP.

S21 XPS Phosphors 2p orbit of ZnO-MAA-NP.

S22 XPS Zinc 2p orbit of ZnO-MAA-NP.

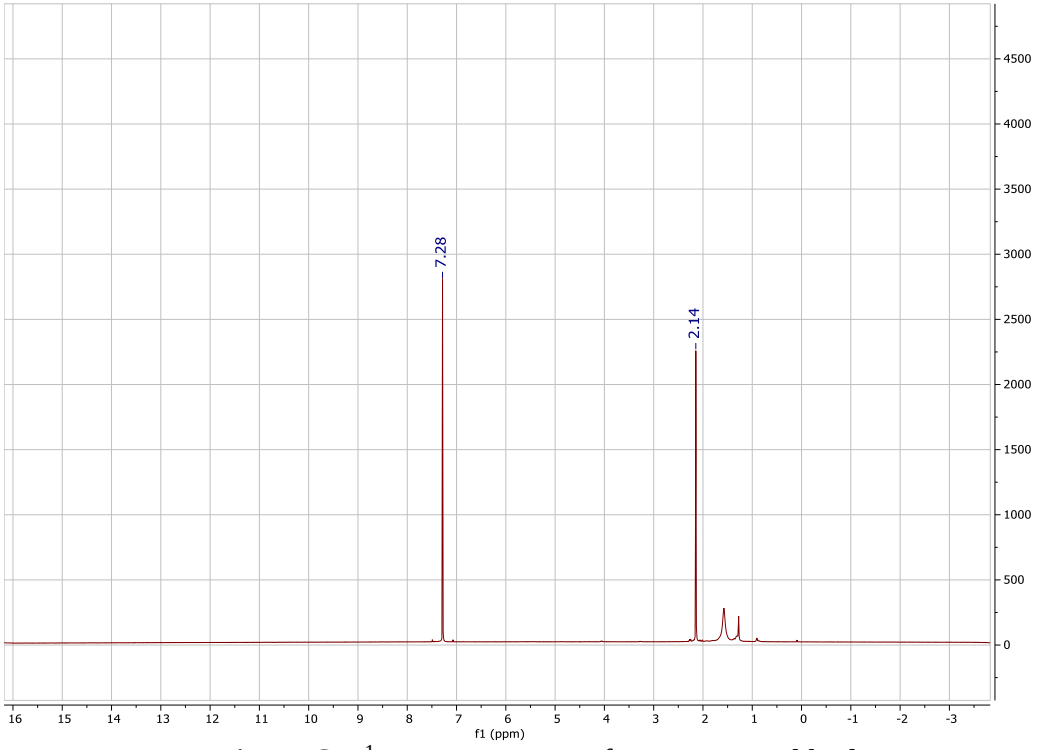

Figure S1. ^{1}H NMR spectra of Zinc acetate dihydrate

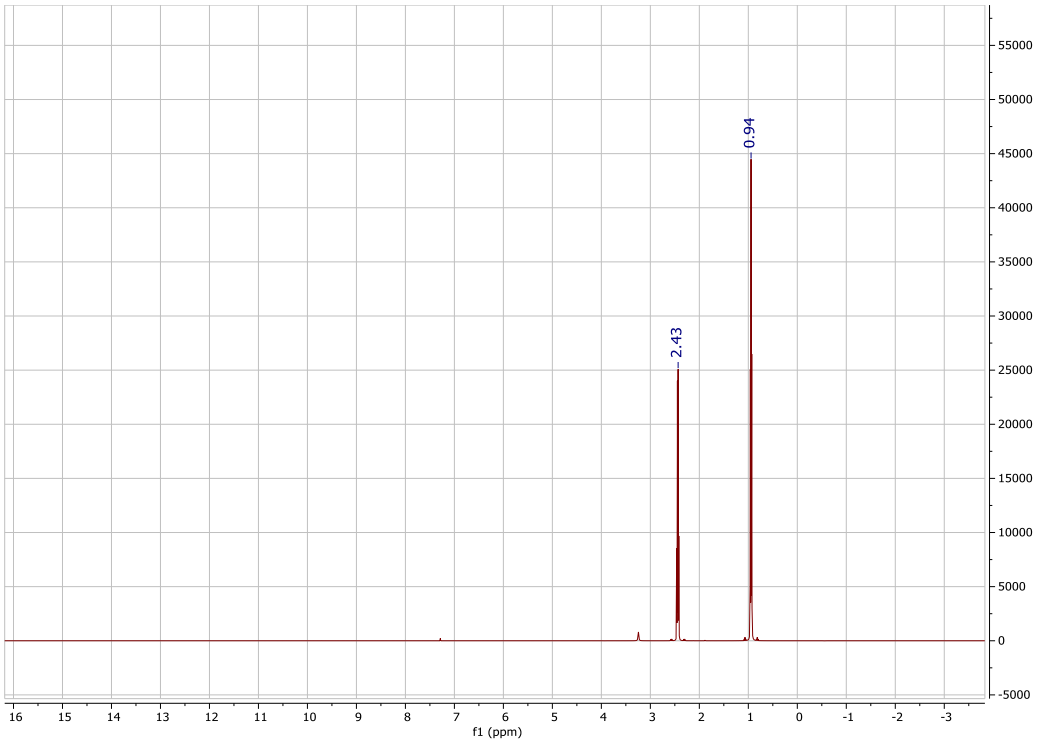

Figure S2. ^{1}H NMR spectra of triethylamine (TEA)

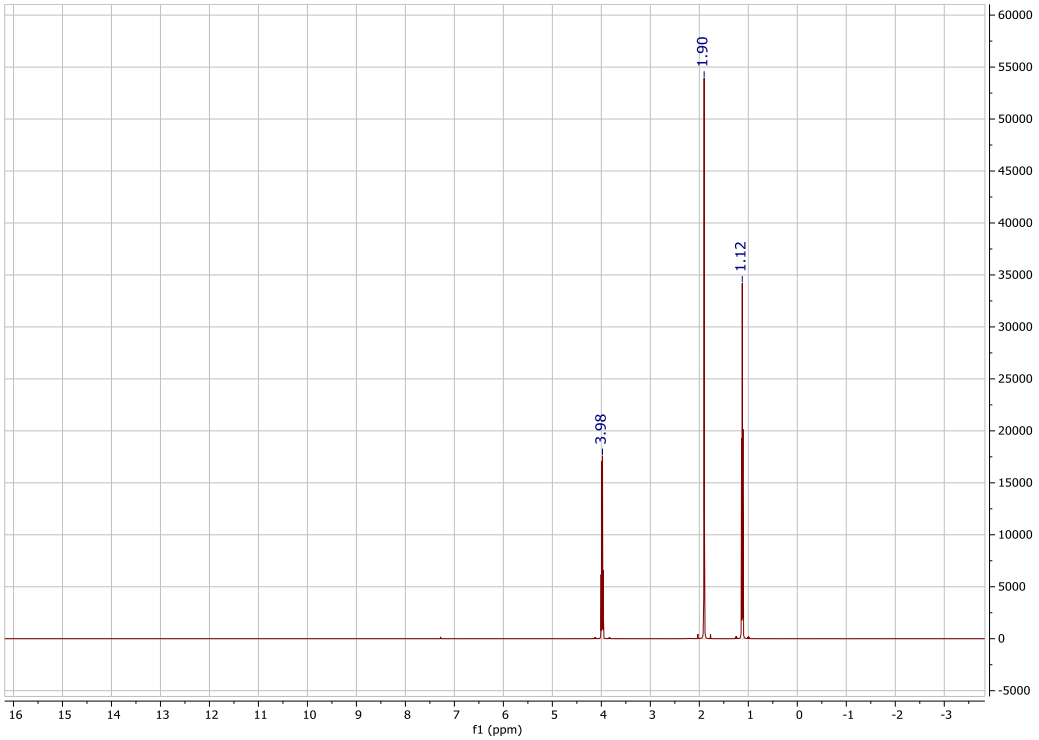

Figure S3. ^{1}H NMR spectra of ethyl acetate (EA)

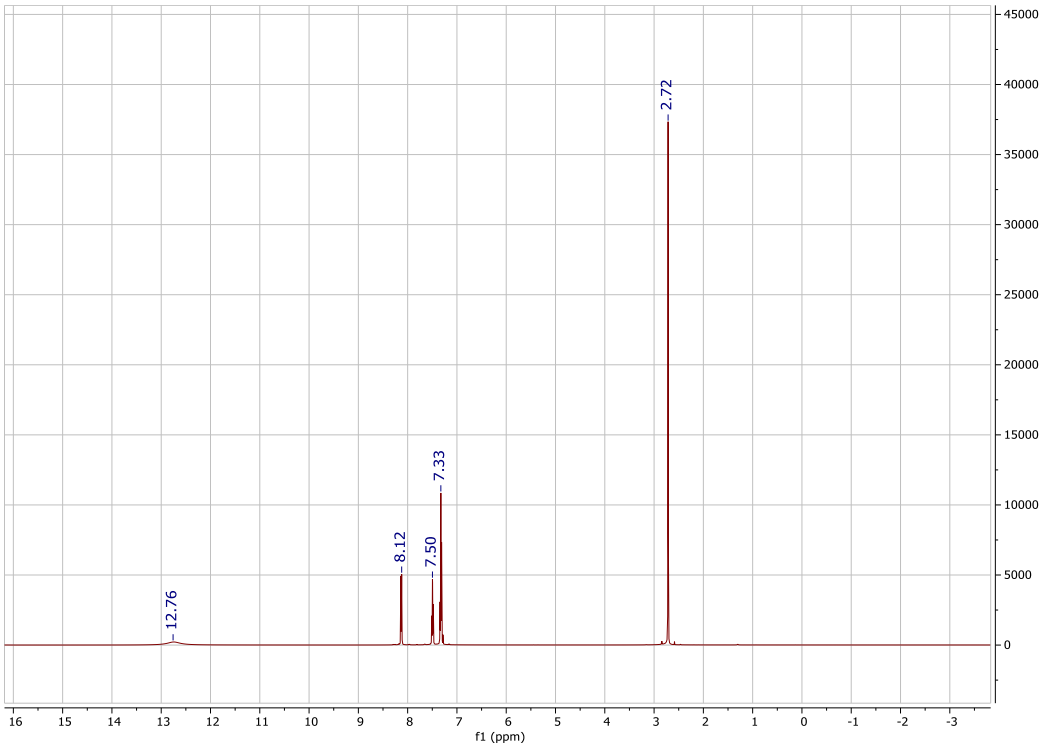

Figure S4. ^{1}H NMR spectra of *o*-Toluic acid (*o*TA)

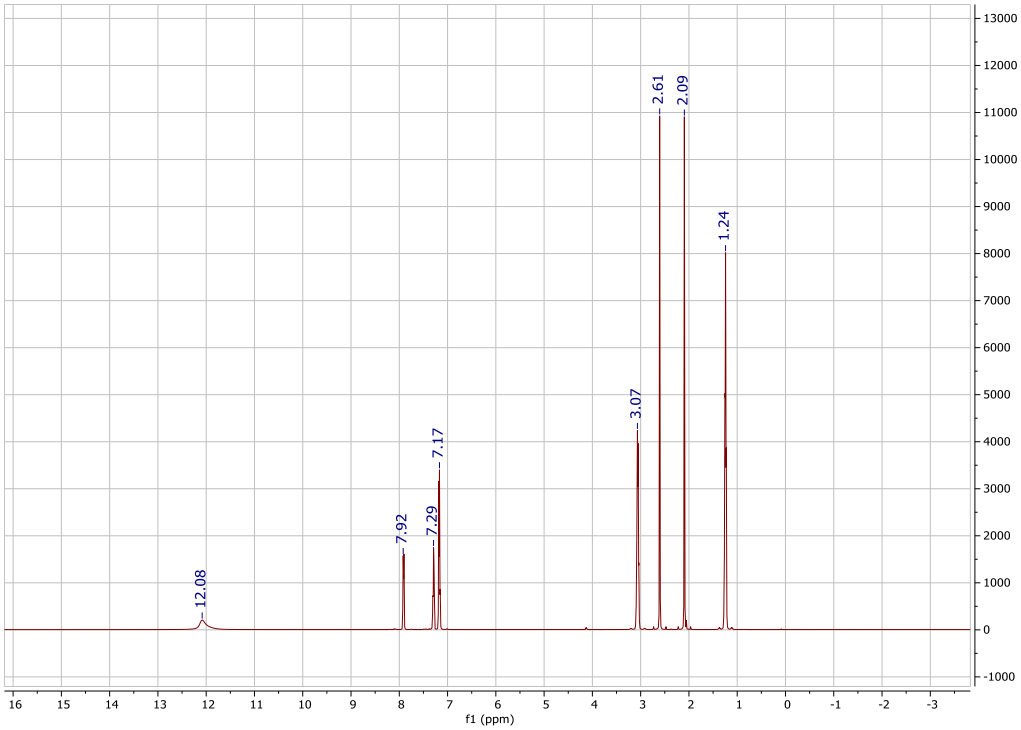

Figure S5. ^{1}H NMR spectra of ZnO-*o*TA-NP

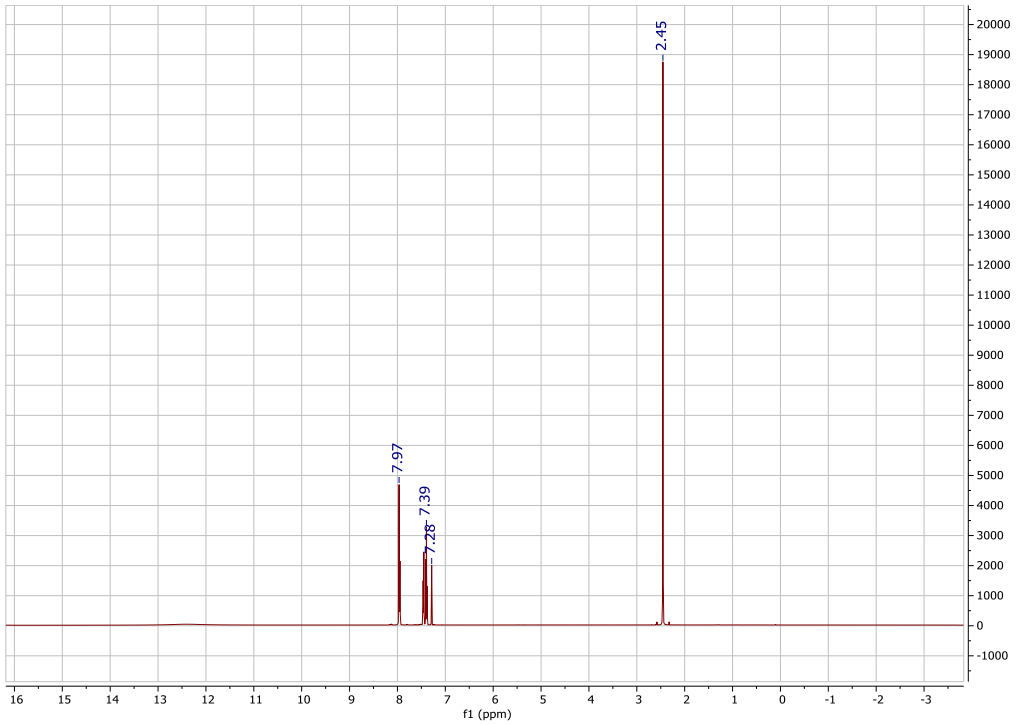

Figure S6. ^{1}H NMR spectra of *m*-Toluic acid (*m*TA)

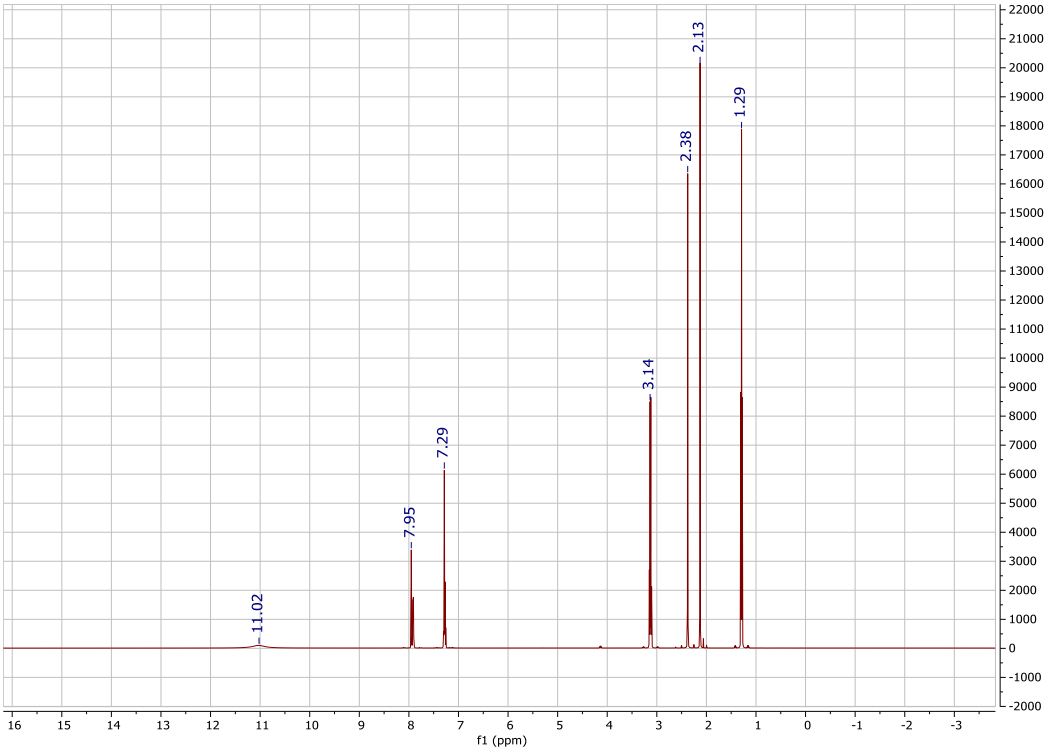

Figure S7. ^{1}H NMR spectra of ZnO-*m*TA-NP

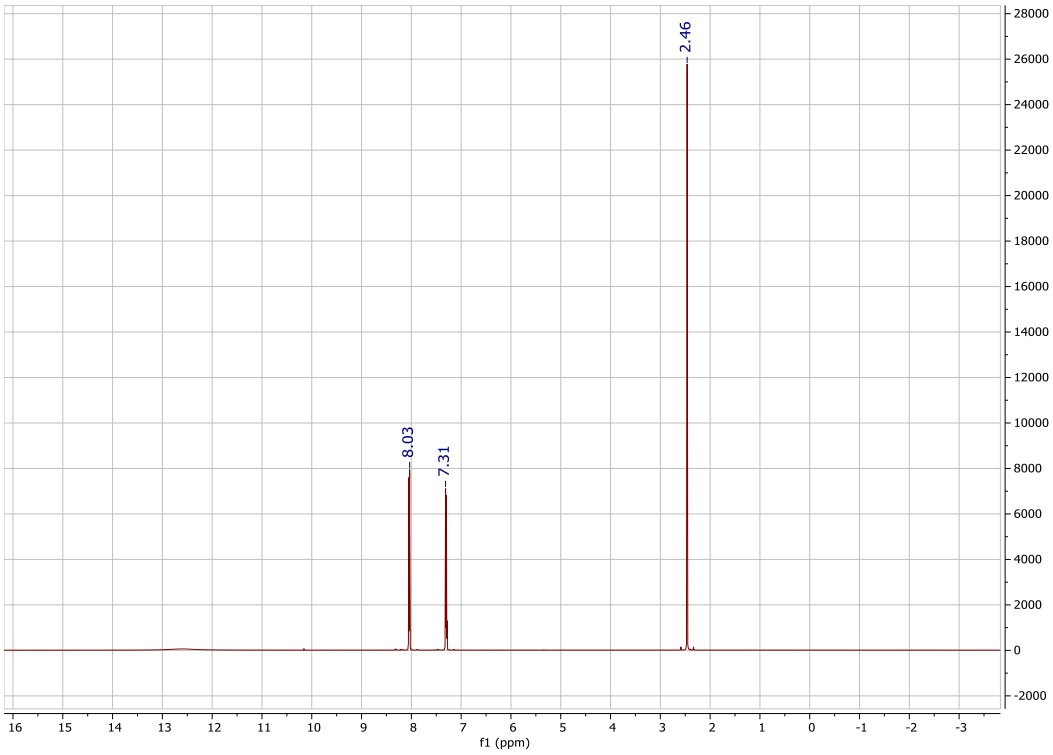

Figure S8. ^{1}H NMR spectra of *p*-Toluic acid (*p*TA)

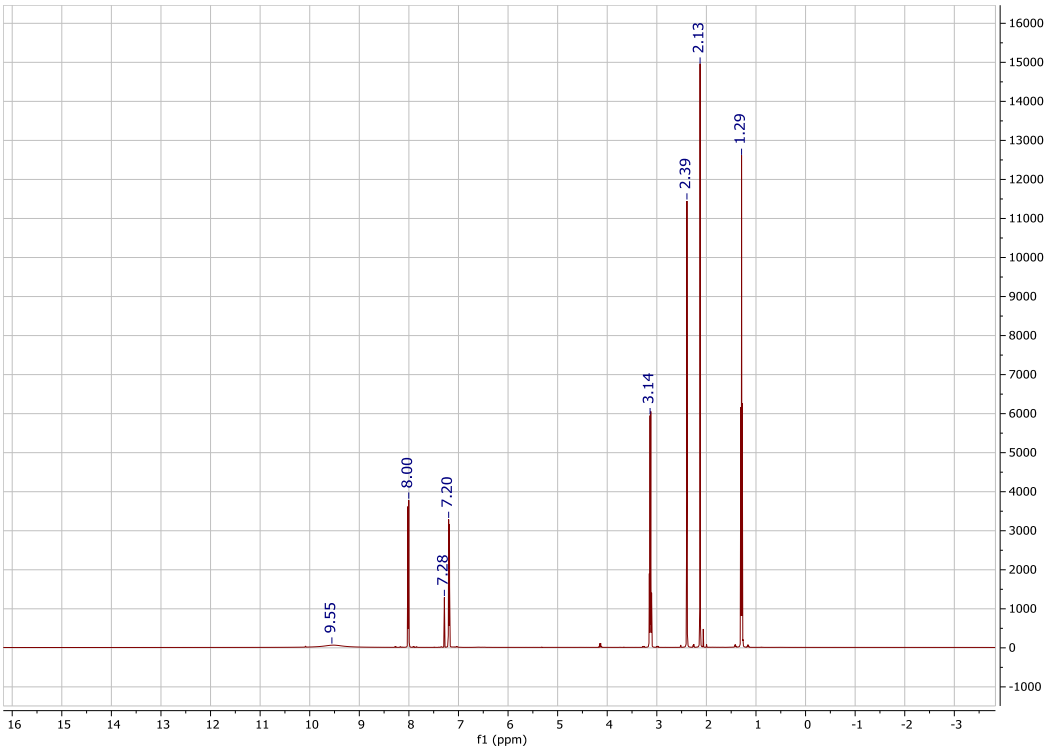

Figure S9. ^{1}H NMR spectra of ZnO-*p*TA-NP

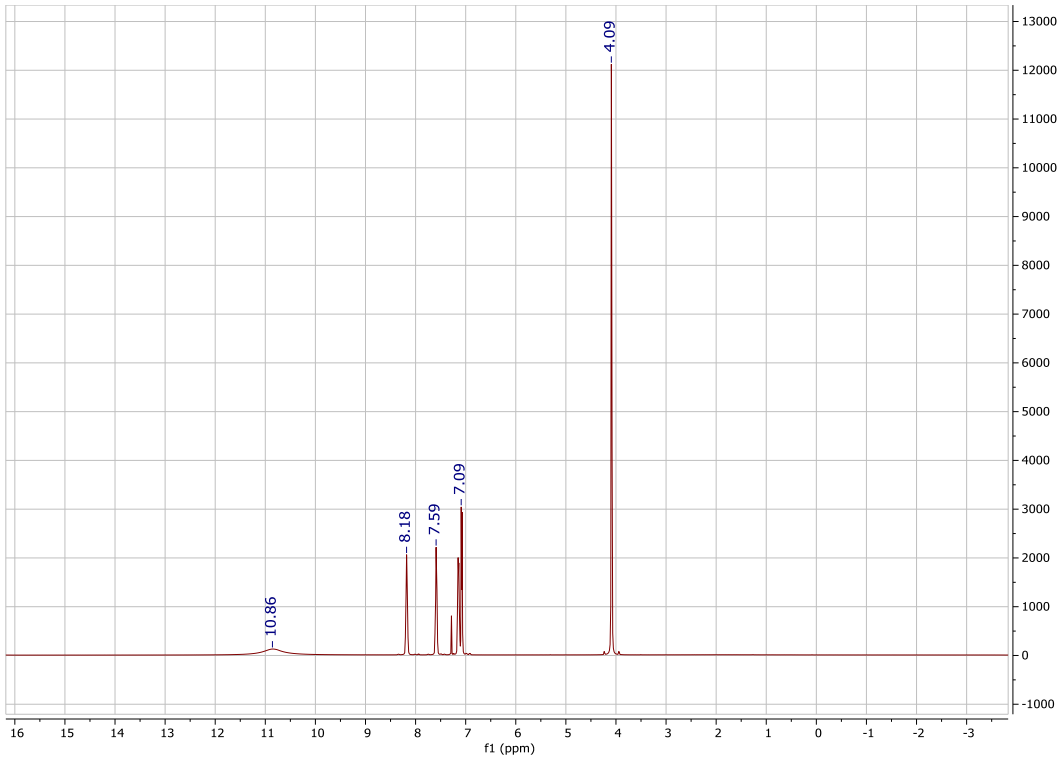

Figure S10. ^{1}H NMR spectra of 2-Methoxybenzoic acid (2MA)

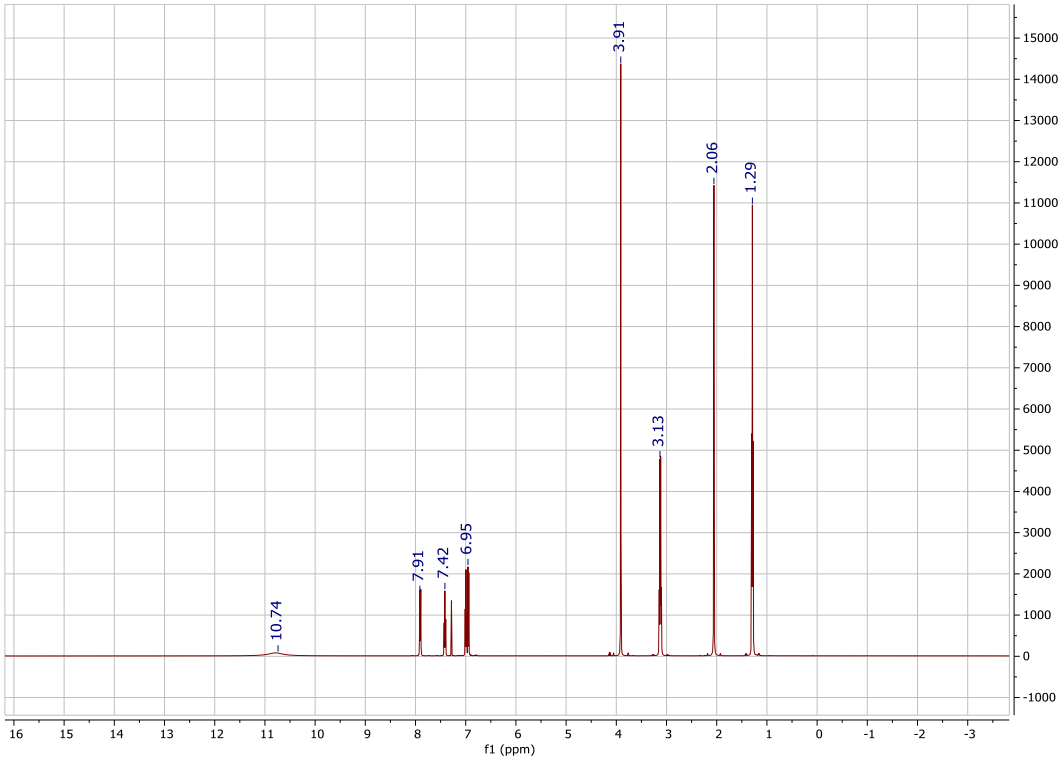

Figure S11. ^{1}H NMR spectra of ZnO-2MA-NP

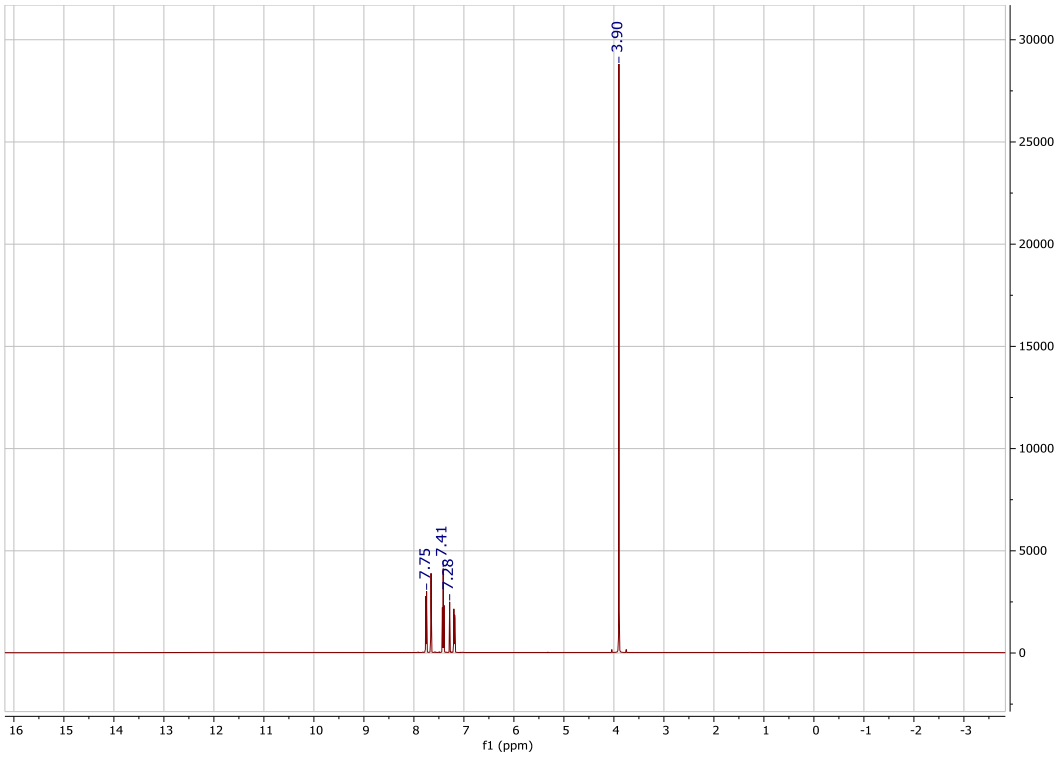

Figure S12. ^{1}H NMR spectra of 3-Methoxybenzoic acid (3MA)

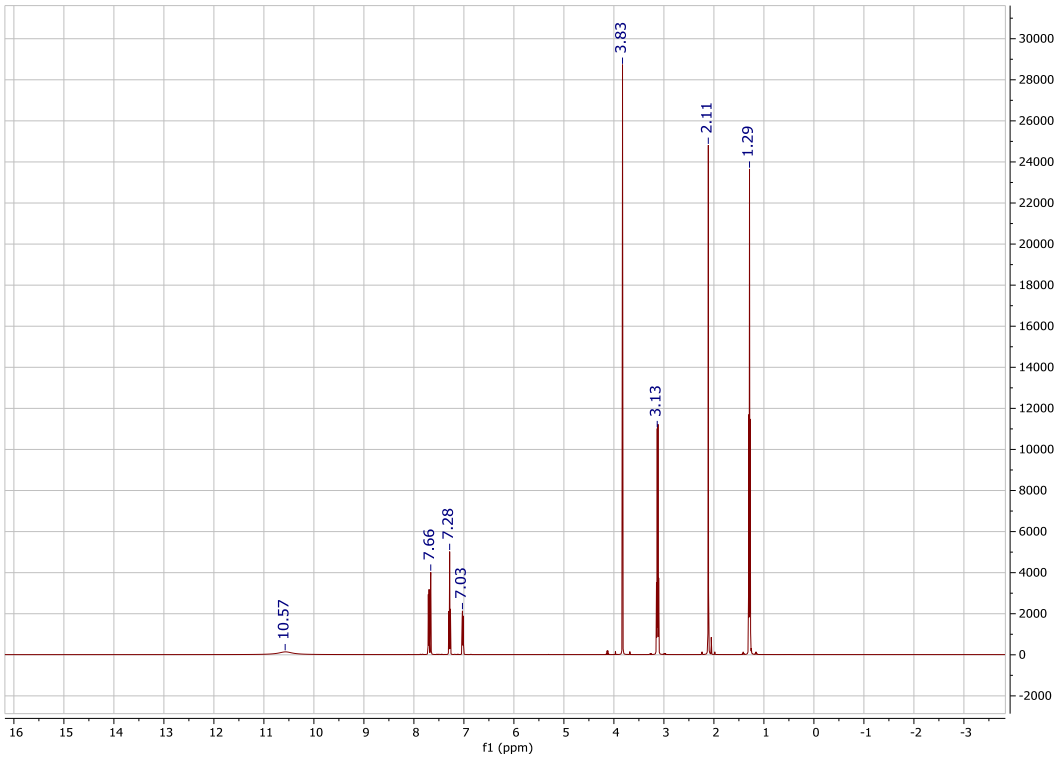

Figure S13. ^{1}H NMR spectra of ZnO-3MA-NP

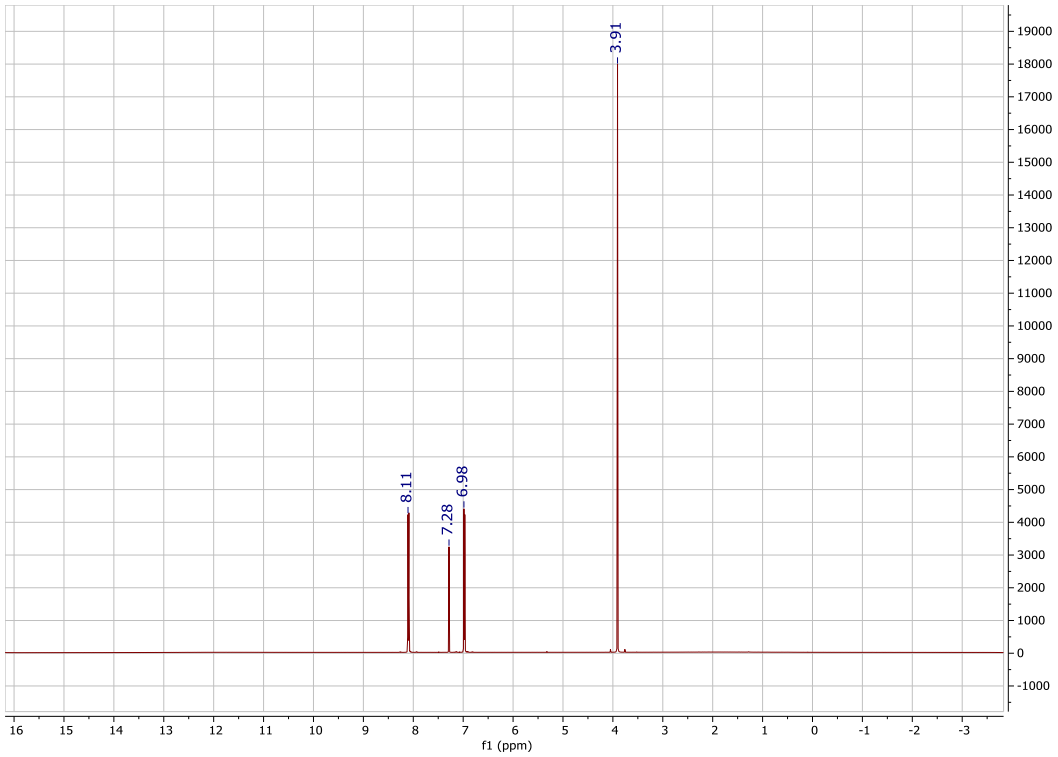

Figure S14. ^{1}H NMR spectra of 4-Methoxybenzoic acid (4MA)

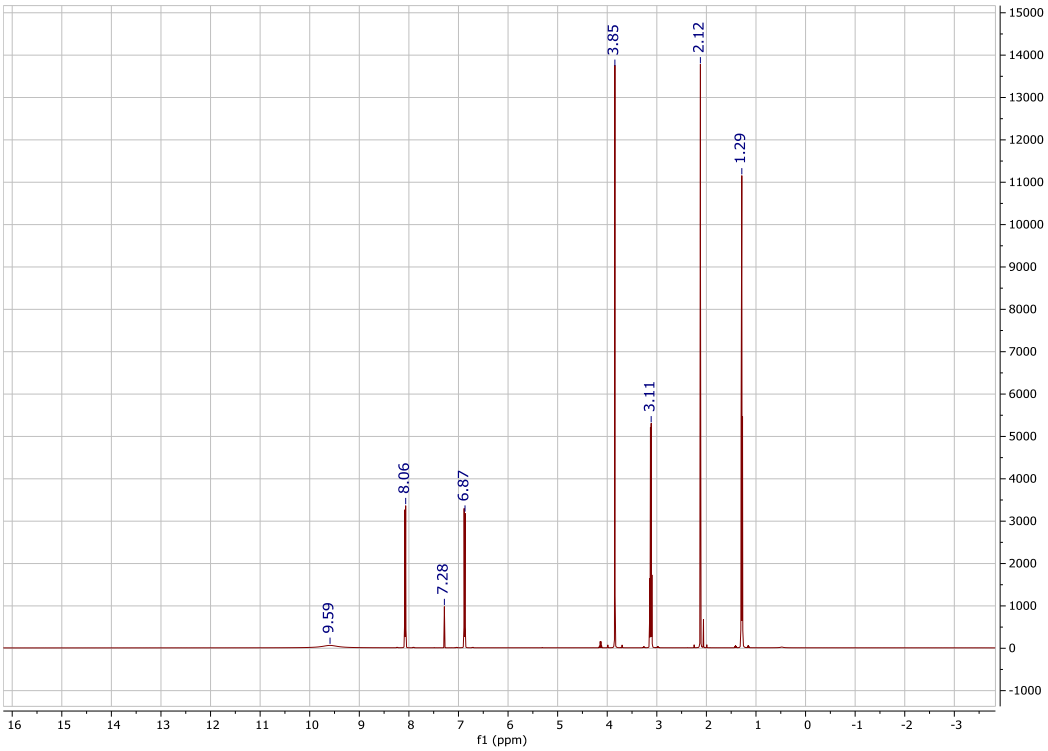

Figure S15. ^{1}H NMR spectra of ZnO-4MA-NP

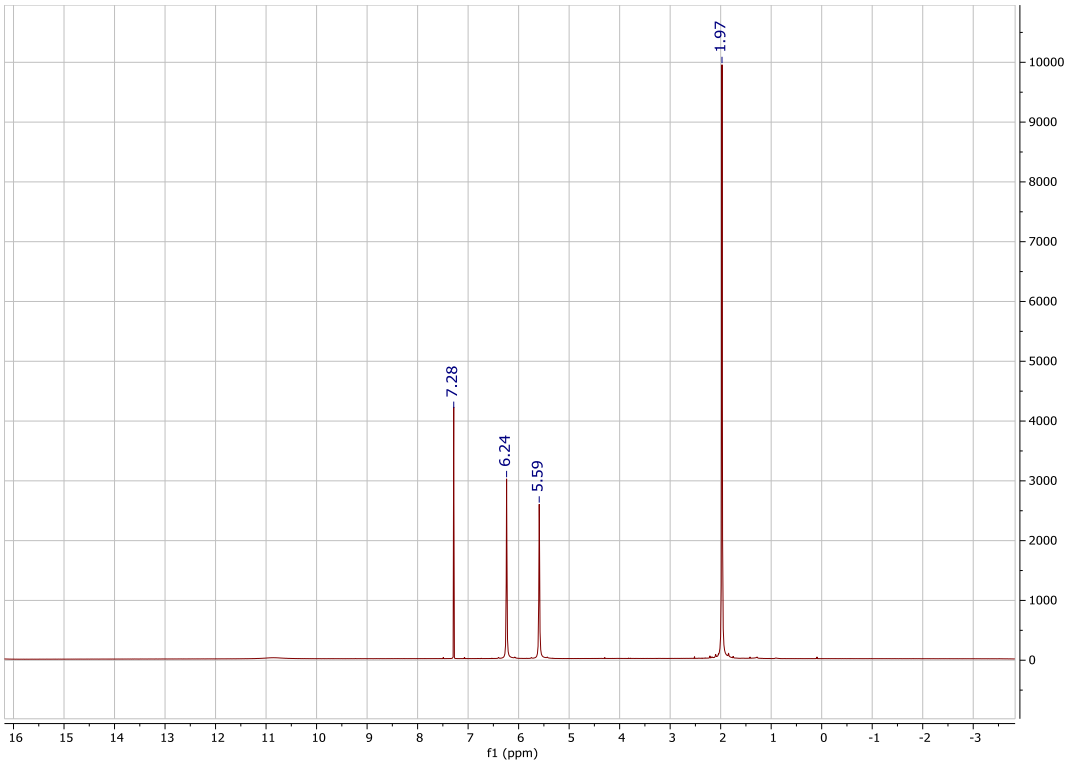

Figure S16. ^{1}H NMR spectra of Zinc Methacrylate

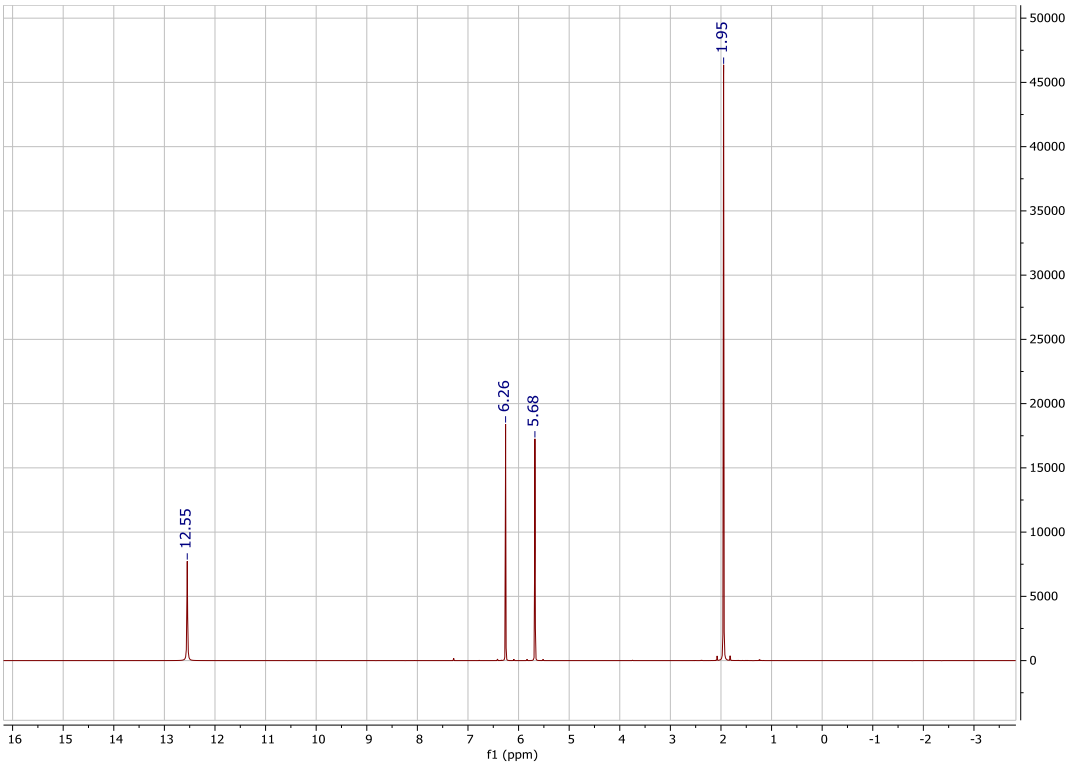

Figure S17. ^{1}H NMR spectra of methacrylic acid (MAA)

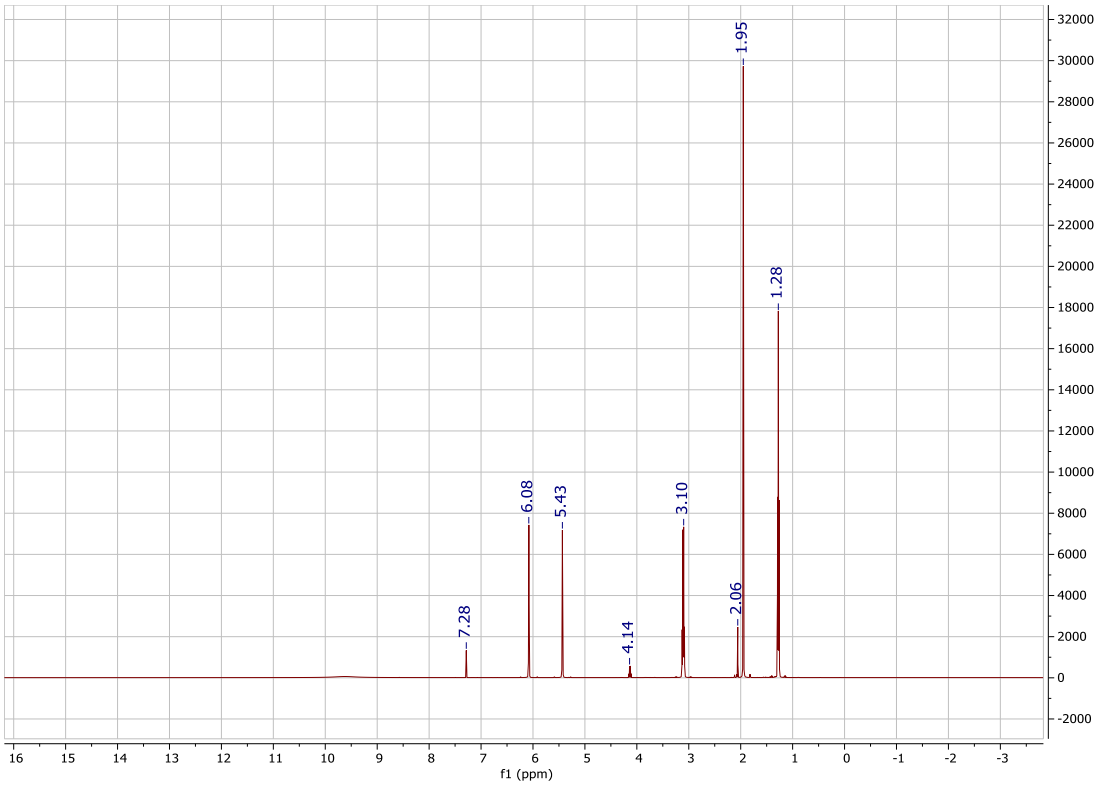

Figure S18. ^{1}H NMR spectra of ZnP-MAA-NP

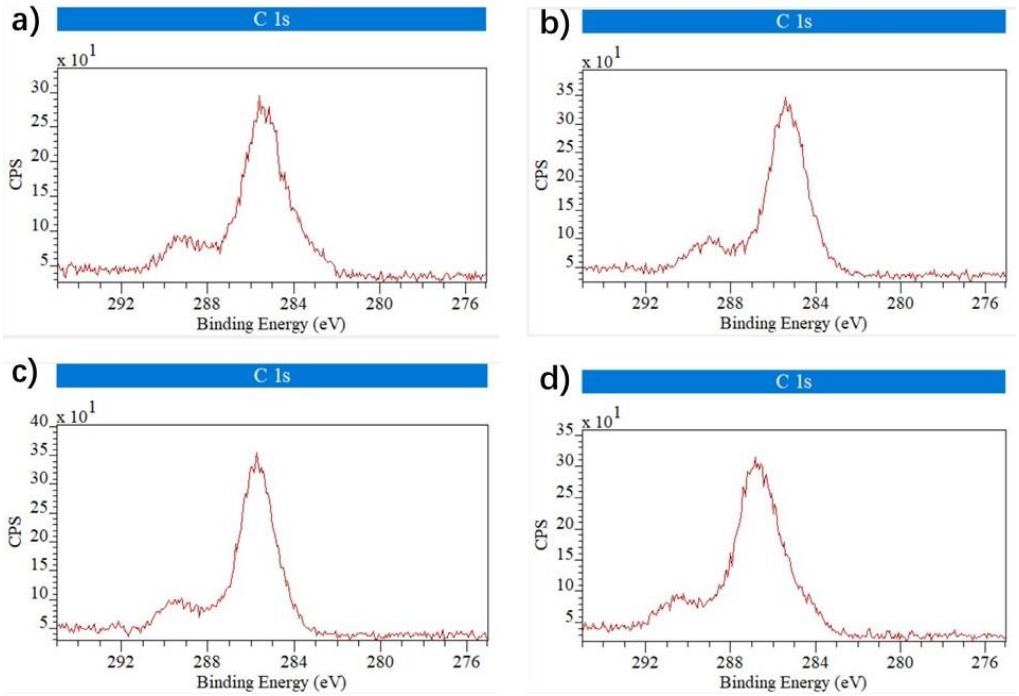

Figure S19. XPS Carbon 1s orbit survey of ZnO-MAA-NP: (a) initiated by PAG before exposure; (b) initiated by PAG after exposure; (c) initiated by PRG before exposure; (d) initiated by PRG after exposure.

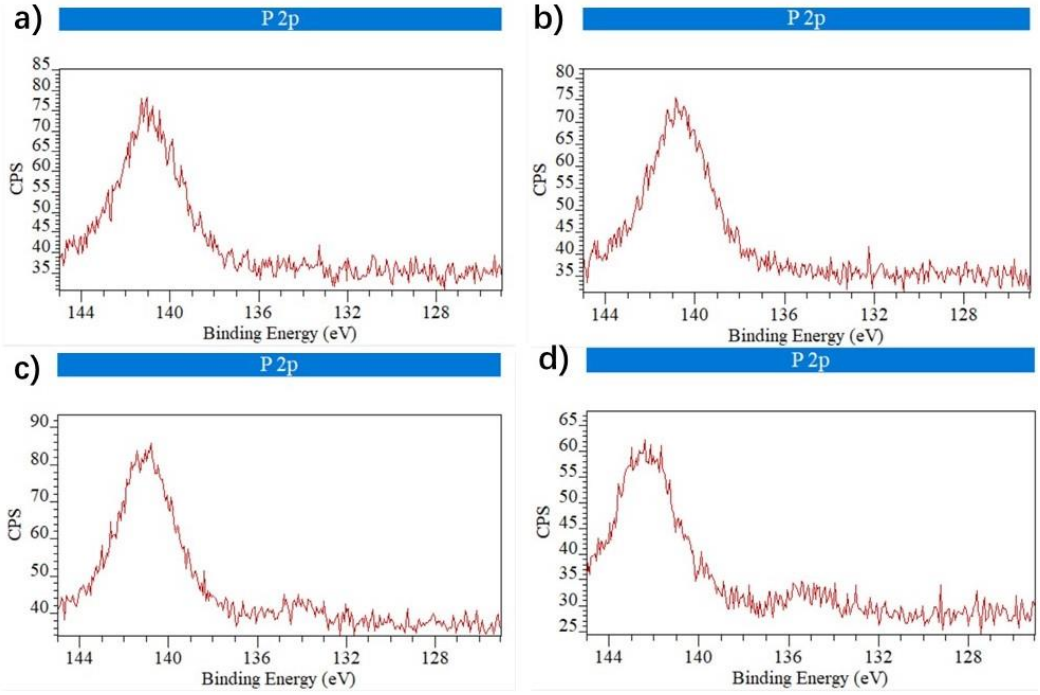

Figure S20. XPS Phosphors 2p orbit survey of ZnO-MAA-NP: (a) initiated by PAG before exposure; (b) initiated by PAG after exposure; (c) initiated by PRG before exposure; (d) initiated by PRG after exposure.

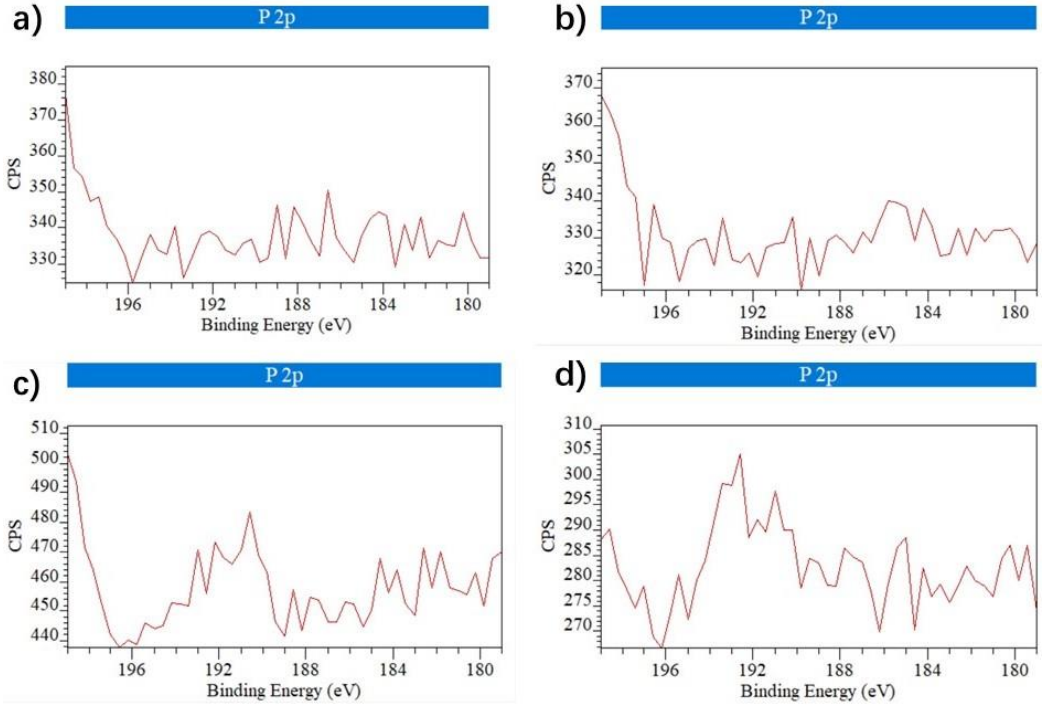

Figure S21. XPS Phosphors 2p orbit survey of ZnO-MAA-NP: (a) initiated by PAG before exposure; (b) initiated by PAG after exposure; (c) initiated by PRG before exposure; (d) initiated by PRG after exposure.

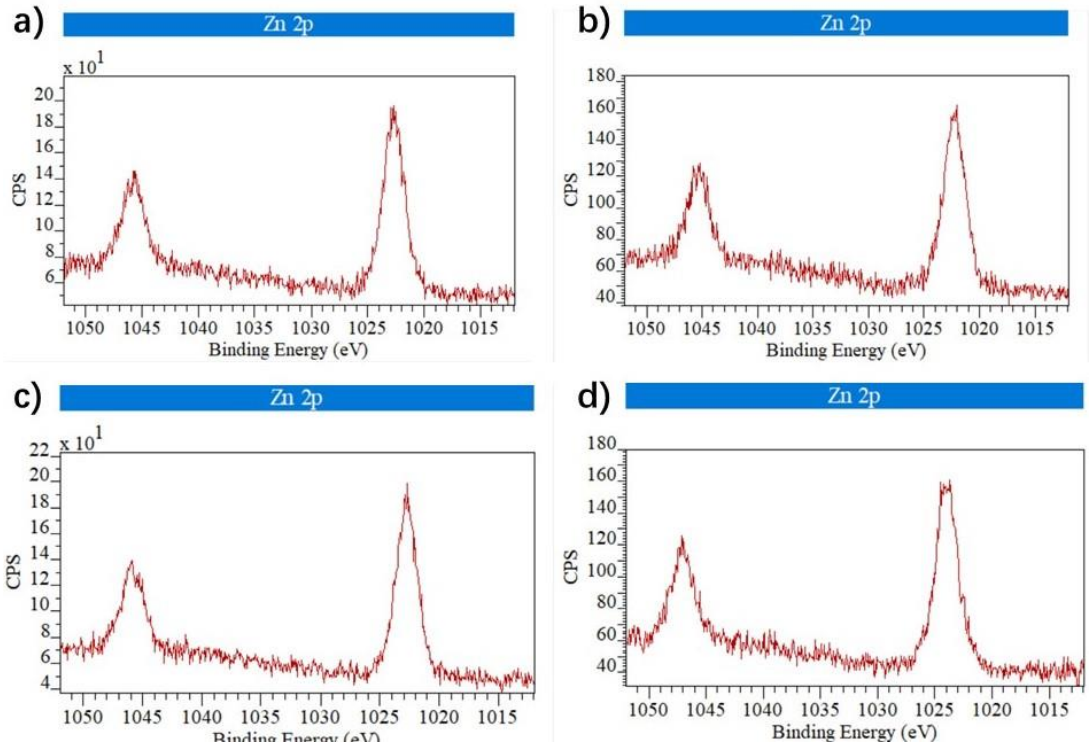

Figure S22. XPS Zinc 2p orbit survey of ZnO-MAA-NP: (a) initiated by PAG before exposure; (b) initiated by PAG after exposure; (c) initiated by PRG before exposure; (d) initiated by PRG after exposure.